

WL-TR-97-4013

**CORE PROGRAMS OF HIGH-PERFORMANCE
COMPOSITE MATERIALS**

A. Crasto, D. Anderson, R. Esterline, C. Hill, R. Kim,
W. Lee, W. Price, B. Rice, and A. Roy

University of Dayton Research Institute
300 College Park Avenue
Dayton, OH 45469-0168



JANUARY 1997

Interim Report for Period 15 September 1995 - 14 September 1996

Approved for public release; distribution unlimited.

MATERIALS DIRECTORATE
WRIGHT LABORATORY
AIR FORCE MATERIEL COMMAND
WRIGHT-PATTERSON AIR FORCE BASE, OH 45433-7734

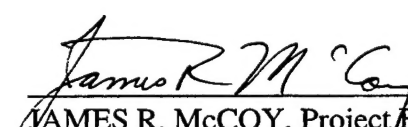
19970814 096

NOTICE

When government drawings, specifications, or other data are used for any purpose other than in connection with a definitely Government-related procurement, the United States Government incurs no responsibility or any obligation whatsoever. The fact that the government may have formulated or in any way supplied the said drawings, specifications, or other data, is not to be regarded by implication, or otherwise in any manner construed, as licensing the holder, or any other person or corporation; or as conveying any rights or permission to manufacture, use, or sell any patented invention that may be related thereto.

This report is releasable to the National Technical Information Service (NTIS). At NTIS, it will be available to the general public, including foreign nations.

This technical report has been reviewed and is approved for publication.



JAMES R. McCOY, Project Engineer
Structural Materials Branch
Nonmetallic Materials Division



ROGER D. GRISWOLD, Chief
Structural Materials Branch
Nonmetallic Materials Division



L. SCOTT THEIBERT, Assistant Chief
Nonmetallic Materials Division
Materials Directorate

If your address has changed, if you wish to be removed from our mailing list, or if the addressee is no longer employed by your organization, please notify WL/MLBC, Bldg 654, 2941 P St, Ste 1, Wright-Patterson AFB OH 45433-7750 to help us maintain a current mailing list.

Copies of this report should not be returned unless return is required by security considerations, contractual obligations, or notice on a specific document.

REPORT DOCUMENTATION PAGE

Form Approved
OMB No. 0704-0188

Public reporting burden for this collection of information is estimated to average 1 hour per response, including the time for reviewing instructions, searching existing data sources, gathering and maintaining the data needed, and completing and reviewing the collection of information. Send comments regarding this burden estimate or any other aspect of this collection of information, including suggestions for reducing this burden, to Washington Headquarters Services, Directorate for Information Operations and Reports, 1215 Jefferson Davis Highway, Suite 1204, Arlington, VA 22202-4302, and to the Office of Management and Budget, Paperwork Reduction Project (0704-0188), Washington, DC 20503.

1. AGENCY USE ONLY (Leave blank)			2. REPORT DATE	3. REPORT TYPE AND DATES COVERED	
			January 1997	Interim - 15 Sep 95 - 14 Sep 96	
4. TITLE AND SUBTITLE			5. FUNDING NUMBERS		
CORE PROGRAMS OF HIGH-PERFORMANCE COMPOSITE MATERIALS			F33615-95-D-5029 PE 62102F PR 4347 TA 34 WU 10		
6. AUTHOR(S)			8. PERFORMING ORGANIZATION REPORT NUMBER		
A. Crasto, D. Anderson, R. Esterline, C. Hill, R. Kim, W. Lee, W. Price, B. Rice, and A. Roy			UDR-TR-97-10		
7. PERFORMING ORGANIZATION NAME(S) AND ADDRESS(ES)			9. SPONSORING/MONITORING AGENCY NAME(S) AND ADDRESS(ES)		
University of Dayton Research Institute 300 College Park Avenue Dayton, OH 45469-0168			10. SPONSORING/MONITORING AGENCY REPORT NUMBER		
Materials Directorate Wright Laboratory Air Force Materiel Command Wright-Patterson AFB OH 45433-7734 POC: James R. McCoy, WL/MLBC, 937/255-9063			WL-TR-97-4013		
11. SUPPLEMENTARY NOTES					
12a. DISTRIBUTION / AVAILABILITY STATEMENT			12b. DISTRIBUTION CODE		
Approved for public release; distribution is unlimited.					
13. ABSTRACT (Maximum 200 words)					
Evaluation of composites continued from the previous contract. New modifications, thermo-oxidative stability, and hydrothermal aging of AFR700 composites were studied. E-beam curing of composites was investigated. Bridge rehabilitation using carbon-epoxy composites was demonstrated. Modeling of damage in carbon-carbon fabric-based composites expanded to include 3-D stresses and model composites testing. Double lap-shear adhesives testing successfully compared predicted and actual test damage. Damage around a hole in a composite in tension was compared to a SVELT model; more detail was predicted by SVELT than FE. The CTE and cracking behavior of spacecraft cyanate ester composites were measured. Processing changes were identified and implemented in the cyanate ester composites. Neural network software has improved composites processing science; it is a more accurate predictor of resin cure than previous analytical models. Hardware and software were acquired to allow the expert control of the carbonization process. New sensors for carbonization investigated included FTIR and off-gas GC/MS. XRD studies of VGCF measured the degree of graphitization and other phases. A thermal conductivity instrument for composites was assembled for testing. The sintering test matrix for single-stage carbonization of pitch was completed. Several new ways of stabilizing pitch were investigated; polymerizable additives are the most promising. A new high-char yield resin was investigated as a carbon-carbon resin.					
14. SUBJECT TERMS			15. NUMBER OF PAGES		
adhesives, AFR700B, carbon-carbon, carbon-epoxy, carbon-phenolic, carbon fiber, carbonization, composite cyanate esters, damage modeling, e-beam curing, expert system, fabric, FTIR, graphite-epoxy, graphitic foams, hydrothermal aging, infrastructure, mechanics modeling, microcellular, morphology, neural networks, microscopy, oxidation, pitch, polyimides, process modeling, qualitative process controls, sensors, sintered carbon, stabilization, SVELT, thermal analysis, thermal cycling, thermo-oxidative stability, thermosets, XRD			157		
16. PRICE CODE					
17. SECURITY CLASSIFICATION OF REPORT		18. SECURITY CLASSIFICATION OF THIS PAGE		19. SECURITY CLASSIFICATION OF ABSTRACT	
Unclassified		Unclassified		Unclassified	
20. LIMITATION OF ABSTRACT					
SAR					

CONTENTS

Section	Page	
1	CHARACTERIZATION OF FIBERS, MATRIX RESINS AND COMPOSITES/TASK 1	1
1.1	COMPOSITE FABRICATION	1
1.2	COMPOSITE MECHANICAL CHARACTERIZATION	1
1.3	THERMAL ANALYSIS	1
1.4	NEW MATRIX RESIN CHARACTERIZATION	1
1.4.1	Screening Study on High-Temperature Polyimides	1
1.4.2	Thermal Oxidative Evaluation of AFR700B/Quartz Composites	1
1.4.3	E-Beam Cure Epoxies	7
1.4.4	Crystallinity of SuperImide Matrix Resins	9
1.4.5	PEPE End-Capped AFR700 Resin	11
1.5	ELECTRON BEAM-CURED COMPOSITE MATERIALS	13
1.5.1	Characterization of Electron Beam-Cured Resins and Composites	13
1.5.1.1	Characterization of Neat Resins	13
1.5.1.2	Processing and Characterization of EBC Composites	16
1.5.2	Electron Beam-Cured Composite Microscopy	20
1.5.3	Characterization of Electron Beam-Exposed Carbon Fibers	20
1.6	COMPOSITES FOR INFRASTRUCTURE REHABILITATION	23
1.6.1	Laboratory Studies	23
1.6.1.1	Materials and Processes	23
1.6.1.2	Performance Evaluation	27
1.6.2	Field Demonstration of Rehabilitation Scheme	29
1.7	CHARACTERIZATION OF POLYMER PROSTHETIC KNEE SOCKETS	31
2	MECHANICS OF POLYMER-MATRIX COMPOSITES	33
2.1	DAMAGE MODELING IN FABRIC-BASED COMPOSITES	33
2.1.1	Equilibrium Equations	36
2.1.2	Compatibility Equations	37
2.1.3	Interface Compatibility Equations	37
2.1.4	Boundary Conditions	38
2.2	COMPOSITE ADHESIVE TESTING	40
2.2.1	Experimental Study of Damage in Bonded Composite Joints	40
2.2.1.1	Bonding Process Selection	40
2.2.1.2	Test Procedure	41

CONTENTS (Continued)

Section	Page
2.2.1.3 Damage Observation	42
2.2.2 Processing of FM300 Adhesive	45
2.3 DAMAGE PROCESS FOR COMPOSITE LAMINATES WITH CENTER HOLES	47
2.4 EXAMINATION OF SPACECRAFT-GRADE CYANATE ESTER COMPOSITES	58
2.4.1 CTE of Composite Laminates for Space Application	58
2.4.1.1 Measurement Technique	58
2.4.1.2 CTE of Unidirectional Composites	60
2.4.1.3 CTE of Off-Axis and Multidirectional Composites	64
2.4.1.4 Influence of Microcracking on Laminate CTE	66
2.4.2 Wright Connection: Edge Effects on Microcracks	67
2.4.3 Processing of XN70A/RS3	67
2.5 DAMAGE INITIATION IN COMPOSITE LAMINATES UNDER MECHANICAL AND THERMAL CYCLIC LOADINGS	68
2.5.1 Analytical Background and Approach	69
2.5.2 Free-Edge Delamination Results	70
3 PROCESSING SCIENCE OF COMPOSITES/TASK 3	75
3.1 INTEGRATION OF SENSORS FOR INTELLIGENT COMPOSITES PROCESSING	75
3.1.1 Neural Network Development Tool	75
3.1.2 Neural Network Model for Reaction Rate	75
3.1.3 Neural Network Models for dc-Resistance and Viscosity	78
3.1.4 On Neural Network Structure	86
3.1.5 On Neural Network Training	86
3.1.6 Neural Network for Sensor/Process Modeling	87
4 CARBON-CARBON AND CARBONACEOUS MATERIALS	88
4.1 CARBONIZATION OF PITCH AND OTHER PRECURSORS	88
4.2 DAMAGE EVOLUTION IN CARBON-CARBON COMPOSITES	88
4.2.1 Processing of Model C-C Laminates	90
4.2.2 Experimental Procedure	90
4.2.3 Laminate Stress-Strain Behavior	90
4.2.4 Damage Observation	93

CONTENTS (Concluded)

Section	Page
4.3 MEASUREMENT OF COMPOSITE THERMAL CONDUCTIVITY	93
4.4 VAPOR-GROWN CARBON FIBERS	96
4.5 UPGRADE OF CARBONIZATION FACILITY	100
4.6 INTELLIGENT PROCESSING OF CARBON-CARBON	101
4.7 INVESTIGATION OF SINTERED CARBON PROCESSING	102
4.7.1 Background	102
4.7.2 Experimental	104
4.7.2.1 Thermoplasticity Measurement	104
4.7.2.2 Variation of Pressing Conditions	105
4.7.2.3 Milling of Resin	105
4.7.2.4 Oxidation Treatment	105
4.7.2.5 Pressing of Panels	109
4.7.2.6 Microstructural Analysis	112
4.7.2.7 Thermoplasticity Testing of Compacted Panels	114
4.7.2.8 Mechanical Testing Results	114
4.7.3 Summary	114
4.8 STABILIZATION OF PITCH	115
4.8.1 Solvent Methods to Infiltrate Pitch	116
4.8.2 Pitch Sample Preparation	117
4.8.3 Stabilization Results for Pitch Samples	118
4.8.3.1 Pitch Samples	118
4.8.3.2 Foams with Additives	119
4.8.3.3 Pitch/T-300 Composites	120
4.8.4 Partial Carbonization of Pitch Samples	121
4.8.5 FTIR Analysis of Pitch	125
4.9 EVALUATION OF A NEW HIGH CHAR YIELD RESIN	130
5 REFERENCES	134
APPENDIX: Notations used in Equation (2-14)	137
PUBLICATIONS, PRESENTATIONS, AND PATENTS	139

FIGURES

Figure		Page
1	Weight Loss per Unit Area of Neat Resins at 371°C After 100 Hours	6
2	Equilibrium Moisture Content of Neat Polyimides at 85°F/85RH	6
3	Glass Transition Temperature of Polyimides After Exposure to Saturated Steam at 150°C	7
4	Thermal Advancement of AS1-Free Radical E-Beam-Cured Epoxy	8
5	Thermal Advancement of RB-47, E-Beam-Cured Epoxy After 6 Hours at 180°C	8
6	Parallel Plate of CAT-B, E-Beam-Curable Epoxy	9
7	Parallel Plate of CAT-B Epoxy During a Hold at 100°C	
8	XRD Scans of SuperImide 800 and AFR600 Powders	10
9	XRD Scans of SuperImide Resin Processed to Various Temperatures	12
10	Moisture Absorption of Three Epoxy Resins Immersed in Water at 23°C	14
11	Dynamic Storage Moduli of Three Neat Epoxy Resins versus Temperature	15
12	Retention of Dynamic Storage Modulus of Three Epoxy Resins as a Function of Temperature	15
13	Change in Dynamic Storage Modulus of Two EBC Epoxies with Isothermal Aging at 121°C	17
14	Epoxy Tensile Strength as a Function of Aging/Test Conditions	17
15	Epoxy Tensile Modulus as a Function of Aging/Test Conditions	18
16	Epoxy Fracture Toughness as a Function of Aging/Test Conditions	18
17	Dynamic Viscosity Data for CAT-B Epoxy Isothermally Aged at Various Temperatures	19

FIGURES (Continued)

Figure		Page
18	Optical Micrographs of Electron Beam-Cured Panel JR-EB1: (a) +45 Ply in Cross Section and -45 Ply Running Horizontal, (b) -45 Ply in Cross Section and +45 Ply Running Horizontal	21
19	Optical Micrograph of Electron Beam-Cured Panel JR-EB2	22
20	Optical Micrograph of Electron Beam-Cured Panel JR-EB3	22
21	Cross Section of Concrete Beam Used in Lab Studies and in the Field (dimensions in cm)	25
22	Sketch of Composite-Reinforced Concrete Beam (dimensions in cm)	26
23	Three Stages in which Composite Plates were Bonded to a Concrete Beam	26
24	Experimental and Calculated Bending Moments vs. Central Deflection for a Concrete Beam Reinforced with Bonded $[0]_4$ CFRP Plates	28
25	Sketch of the Sequence of Failure Modes in the Flexure of a Concrete Beam Reinforced with Bonded Composite Plates	28
26	Comparison of Measured Bending Moments vs. Central Deflection for Three Beams	30
27	XRD Scans of the Two Prosthetic Material Samples	32
28	Parallel Plate Rheometry; Temperature and Viscosity Profiles of FM30-2K Adhesive Using the Manufacturer's Recommended Cure Cycle	41
29	Parallel Plate Rheometry; Temperature and Viscosity Profiles of FM30-2K Adhesive Using the Modified Cure Cycle	41
30	Specimen Configuration and Representative Strain Gage Locations of the Double Lap-Shear Specimen	43
31	Measured Strains at Locations 4, 5, 6, and 7	43
32	Interlaminar Normal Strains at a Damage-Sensitive Location for Several Incremental Loadings	44

FIGURES (Continued)

Figure		Page
33	Micrograph (in Fluorescent Field) Indicating Crack Initiation at the Middle Adherent Interface	44
34	Interlaminar Normal Strains at a Damage-Sensitive Location for Several Incremental Loadings Beyond Crack Initiation in the Bond	45
35	Edge Micrograph Showing Interface Crack at the Middle Adherent Interface taken After a Load of 90 Percent of Failure	46
36	Edge Micrograph Showing Interface Crack Moving from One Adherent Interface to the Other	46
37	Representative Sequential Crack Propagation Event	46
38	Parallel Plate Experiment of FM300 Adhesive	47
39	Specimen Showing Strain Gage Locations	49
40	Comparison of Analytical and Experimental Strains at Hole Vicinity for $[0]_{8T}$ Laminate	50
41	Comparison of Analytical and Experimental Strains at Hole Vicinity for $[90]_{8T}$ Laminate	50
42	Comparison of Analytical and Experimental Strains at Hole Vicinity for $[\pm 45]_{2S}$ Laminate	51
43	Comparison of Analytical and Experimental Strains at Hole Vicinity for $[0_2/90_2]_S$ Laminate	51
44	Comparison of Analytical and Experimental Strains at Hole Vicinity for $[\pm 30/90_2]_S$ Laminate	52
45	Experimental Stress-Strain Relation for $[0]_{8T}$	52
46	Experimental Stress-Strain Relation for $[90]_{8T}$	53
47	Experimental Stress-Strain Relation for $[\pm 45]_{2S}$	53
48	Experimental Stress-Strain Relation for $[0_2/90_2]_S$	54

FIGURES (Continued)

Figure		Page
49	Experimental Stress-Strain Relation for $[\pm 30/90_2]_S$	54
50	Radiograph Showing Damage Around the Hole in a $[0]_{8T}$ Specimen at an Applied Stress of 39.25 ksi	55
51	Radiograph Showing Damage Around the Hole in a $[\pm 45]_{2S}$ Specimen at an Applied Stress of 21.83 ksi	55
52	Radiograph Showing Damage Around the Hole in a $[0/90]_{2S}$ Specimen at an Applied Stress of 24.67 ksi	56
53	Radiograph Showing Damage Around the Hole in a $[\pm 30/90_2]_S$ Specimen at an Applied Stress of 20.4 ksi	56
54	Radiograph Showing Damage Around the Hole in a $[0/90]_{2S}$ Specimen at an Applied Stress of 130.56 ksi	57
55	Radiograph Showing Damage Around the Hole in a $[\pm 30/90_2]_S$ Specimen at an Applied Stress of 56.91 ksi	57
56	Apparent Strain for WK-Series Strain Gages	61
57	Thermal Strain vs. Test Temperature for Aluminum	61
58	Thermal Strain vs. Test Temperature for Invar	62
59	Thermal Strain in the Longitudinal Direction vs. Temperature for XN70/RS3 Unidirectional Specimen	62
60	Thermal Strain in the Longitudinal Direction vs. Temperature for AS4/3501-6 Unidirectional Specimen	63
61	Thermal Strain in the Transverse Direction vs. Temperature for XN70/RS3 Unidirectional Specimen	63
62	Thermal Strain in the Transverse Direction vs. Temperature for AS4/3501-6 Unidirectional Specimen	64
63	Comparison of CTE between Prediction and Experiment for a Variety of the Off-Axis Angles for XN70/RS3 Composites	65

FIGURES (Continued)

Figure		Page
64	Thermal Strain vs. Temperature for the $[0/90]_{2S}$ of AS4/3501-6 Composite	65
65	Thermal Strain vs. Temperature for the $[0/\pm 45/90]_S$ of AS4/3501-6 Composite	66
66	Autoclave Cure of XN70A/RS3 with Hughes Cure Cycle	68
67	Autoclave Cure of XN70A/RS3 with Modified Cure Cycle	68
68	Interlaminar Stress Distribution at the 30/-30 Interface Due to Residual Curing Stress	72
69	Interlaminar Stress Distribution at the Midplane Due to Residual Curing Stress	72
70	Interlaminar Stress Distribution at the 30/-30 Interface Due to Mechanical Loading	73
71	Interlaminar Stress Distribution at the Midplane Due to Mechanical Loading	73
72	Microphotograph Showing Free-Edge Delamination Under Static Loading	74
73	Interlaminar Shear S-N Relation	74
74	The Structure of the Back Propagation Neural Network Reaction Rate Model	76
75	The Training Set from DSC Scans at 0.2, 1, 2, and 5°C/min	76
76	Verification of BNN Model Against DSC Data and Comparison to Loos-Springer Analytical Model	79
77	Verification of BNN Model Against Thermopile Data from a Single Ramp Cycle and Comparison to Loos-Springer Analytical Model	80
78	Verification of BNN Model Against Thermopile Data from a Standard Cure Cycle and Comparison to Loos-Springer Analytical Model	81

FIGURES (Continued)

Figure		Page
79	Glass Transition Temperatures and Predicted Degree of Cure of Hercules 3501-6 Resin Undergoing Isothermal Cure Reaction	82
80	Measured dc-Resistance and Viscosity of 3501-6 Resin at Different Temperature Ramp Rates for Training the BNN Models	83
81	Verification of BNN Models for dc-Resistance and Viscosity	85
82	A Representative Volume Element (RVE) of Woven Fabric Composite	89
83	The Model Carbon-Carbon Composite with Simulated Planar (x-Plane) Yarn Crimping	89
84	Cross-Sectional Micrograph of the Virgin $([90_2/0_2]_S, [0_2/90_2]_S, 0.054)$ Laminate	91
85	Stress-Strain Behavior of a Model Cross-Ply $[90_2/0_2]_S$ Carbon-Carbon Laminate with Incremental Loading	91
86	Stress-Strain Behavior of Three Specimens of a Model Cross-Ply $[90_2/0_2]_S$ Carbon-Carbon Laminate	92
87	Stress-Strain Behavior of Three Specimens of the Model $([90_2/0_2]_S, [0_2/90_2]_S, 0.054)$ Carbon-Carbon Laminate	92
88	<i>In Situ</i> Cross-Sectional Micrograph of the $([90_2/0_2]_S, [0_2/90_2]_S, 0.054)$ Laminate at a Strain Level of 0.162 Percent	94
89	<i>In Situ</i> Cross-Sectional Micrograph of the $([90_2/0_2]_S, [0_2/90_2]_S, 0.050)$ Laminate at a Strain Level of 0.195 Percent	94
90	<i>In Situ</i> Cross-Sectional Micrograph of the $([90_2/0_2]_S, [0_2/90_2]_S, 0.050)$ Laminate at a Strain Level of 0.23 Percent	94
91	(a) Micrograph of the Left Side of the $([90_2/0_2]_S, [0_2/90_2]_S, 0.054)$ Laminate After Failure; and (b) Micrograph of the Right Side of the $([90_2/0_2]_S, [0_2/90_2]_S, 0.054)$ Laminate After Failure	95
92	Micrograph of the $([90_2/0_2]_S, [0_2/90_2]_S, 0.054)$ Laminate After Failure Indicating Extent of Matrix Damage	95

FIGURES (Continued)

Figure		Page
93	Temperature Change of Specimen in Terms of Data Acquisition Board Reading at 1 kHz	96
94	Phase Identification in the ANC-27 (Coal Precursor) Samples	101
95	Thermoplasticity Measurement of Oxidized Pitch Resin	104
96	Representative Powder Size Distribution for Jet-Milled Pitch	106
97	Percent Oxidation Weight Gain for Jet-Milled AR Resin	108
98	Photograph of 2"x6" Hot Press Mold	110
99	Whole Panels in the Compacted and Sintered Conditions	111
100	Fracture Surface SEM Images of Panel E4 which was Oxidized to 6% and Pressed at 5000 psi and 225°C for 240 min	113
101	Pellets after Carbonization: (a) Pellet formed from Powder Treated with Nitric Acid and (b) a Typical Bloated Pellet	120
102	Optical Polarizing Microscopy of Partially-Carbonized A-240 Pitch Showing Different Size Mesophase Regions in the Same Sample	124
103	Normalized FTIR Absorption Scan for Unoxidized and 6% Oxidized Mitsubishi AR Pitch Powder	128
104	Absorption Ratios for Mixes of 0 and 6% Oxidized AR Pitch Powders	128
105	Absorption Ratios of Hydrogen Species for Mixes of 0 and 6% Oxidized AR Pitch Powders	129
106	Absorption Ratios for AR Pitch Powders Oxidized to Various Levels	129
107	Absorption Ratios of Hydrogen Species for AR Pitch Powders Oxidized to Various Levels	130
108	Optical Microscopy of a Cured PCP Composite: (a) Bright Field and (b) Fluorescent Image	131

FIGURES (Concluded)

Figure		Page
109	Optical Microscopy of a Carbonized PCP Composite: (a) Bright Field and (b) Fluorescent Image	133

TABLES

Table	Page
1 Composites Fabricated	2
2 Composite Mechanical Testing for the Period of 15 Sep 95 - 14 Sep 96	4
3 SuperImide Crystalline Peaks and Crystallinity in Neat Resin Samples Processed to Various Temperatures	12
4 Mechanical Properties of IM7/RB-47 Composite Compared with a Typical Thermally-Cured Epoxy Composite	19
5 Relevant Properties of Constituents for Infrastructure Rehabilitation	25
6 Summary of Center Hole Composite Test Matrix	48
7 Changes in AS4/3501-6 Laminate Stiffness and CTE with Microcracking	67
8 Thermomechanical Properties of IM7/5250-4	70
9 Link Weights ($w_{i,j,k}$) of the BNN Reaction Rate Model for 3501-6 Epoxy Resin	77
10 Link Weights ($w_{i,j,k}$) of the BNN dc-Resistance Model for 3501-6 Epoxy Resin	84
11 Link Weights ($w_{i,j,k}$) of the BNN Viscosity Model for 3501-6 Epoxy Resin	84
12 Effects of Oxidation and Heat Treatment on Pyrograf III TM Crystallinity	97
13 Crystallinity of "As-Made" and Heat-Treated Pyrograf-I TM Samples	97
14 First Production Monitoring of Pyrograf III TM Crystallinity	98
15 Reproducibility of Pyrograf III TM Crystallinity	98
16 Second Production Monitoring of Pyrograf III TM Crystallinity	99
17 Third Production Monitoring of Pyrograf III TM Crystallinity	99
18 Hyper-Greco-Latin Square Test Matrix of Pressing Conditions	106

TABLES (Concluded)

Table		Page
19	Effect of Increasing Ramp Rates on Degree of Exotherm	107
20	Mixing of PAN Oxidized Pitch Batches	108
21	Pitch Sintering Pressing Conditions and Processing Success	110
22	Pitch Sintering Physical and Mechanical Data Results	115
23	Pitch Stabilization in Composites Results	122
24	Partial Carbonization Yields (% Remaining) for A-240 and Aerocarb-80 Pitches as a Function of Time Held at 450°C	125
25	Absorption Bands Reported by Drbohlav and Stevenson [25] for Oxidized Pitch and Generally in Silverstein and Bassler [26]	127

FOREWORD

This report was prepared by the University of Dayton Research Institute under Air Force Contract No. F33615-95-D-5029, Delivery Order No. 0001. The work was administered under the direction of the Nonmetallic Materials Division, Materials Directorate, Wright Laboratory, Air Force Materiel Command, with Dr. James R. McCoy (WL/MLBC) as Project Engineer.

This report was submitted in January 1997 and covers work conducted from 15 Sep 1995 through 14 Sep 1996.

SECTION 1

CHARACTERIZATION OF FIBERS, MATRIX RESINS AND COMPOSITES/TASK 1

1.1 COMPOSITE FABRICATION

A list of composites fabricated during this reporting period is given in Table 1.

1.2 COMPOSITE MECHANICAL CHARACTERIZATION

Composite mechanical testing performed during this reporting period is given in Table 2.

1.3 THERMAL ANALYSIS

Two hundred and sixty-seven samples were run during this reporting period. The materials consisted of: AFR700B, AFR-MBTA, AFR700B/S2, AFR-PEPE, SuperImide 800, 3501-6, AS4/3501-6, CATB, RB-47, graphite/epoxy, FM73/polyester, Blackglas, carbon/UHM, nylon 6/6, inhibited carbon-carbon, AR pitch, SC 1008/T300, phenolic/Pyrograph III, epoxy/Pyrograph III, A240 pitch, furfuryl alcohol, furfuryl aldehyde, diallyl bisphenol A, phenylmaleimide, bismaleimide/DABA, bismaleimide/MDA, bismaleimide/DDS, nadimide, benzophenone, pyromellitic diimide, titanium, Invar, and soda lime glass.

1.4 NEW MATRIX RESIN CHARACTERIZATION

1.4.1 Screening Study on High-Temperature Polyimides

A screening study was conducted on several high-temperature polyimides [1] to evaluate their performance with regard to thermal oxidative stability (Figure 1), equilibrium moisture content (Figure 2), and hydrolytic stability (Figure 3). These data show that TRW800D (now SuperImide 800) has superior TOS and hydrolytic stability when compared to AFR700B; however, other studies have shown that the processability and mechanical properties of TRW800D are lacking. The results of AFR-PEPE look promising, and further work on this polyimide will continue.

1.4.2 Thermal Oxidative Evaluation of AFR700B/Quartz Composites

Two AFR700B/quartz composites, which were fabricated at McClellan AFB, were evaluated for thermal oxidative stability. One composite was cured with a Kapton® and Teflon® peel ply on the tool side, and the other was cured on a tool coated with Monocoat E-150.

TABLE 1
COMPOSITES FABRICATED

Material	Panel Size	Orientation	No. of Plies	Remarks
AS4/3501-6	12x12	[0] _{16T}	16	25 ea
AS4/3501-6	12x12	[0] _{8T}	8	6 ea
AS4/3501-6	12x12	[±45] _{2S}	8	5 ea
AS4/3501-6	6x12	[0] _{12T}	12	
AS4/3501-6	6x12	[0] _{24T}	24	
AS4/3501-6	6x6	[0/±45/90] _S	8	
AS4/3501-6	12x12	[0] _{10T}	10	
AS4/3501-6	12x12	[0] _{20T}	20	
AS4/3501-6	12x12	[0] _{30T}	30	
AS4/3501-6	12x12	[0] _{40T}	40	
AS4/3501-6	6x6	[0 ₂ /90 ₂]	8	
AS4/3501-6	6x6	[0 ₂ /90] _S	6	
AS4/3501-6	6x6	[0] _{5T}	5	2 ea
AS4/3501-6	6x6	[0] _{7T}	7	
AS4/3501-6	12x12	[0] _{12T}	12	
AS4/3501-6	6x6	[0/45/90/-45] _S	8	
IM7/5250-4	12x12	[±30/90 ₂] _{3S}	24	
IM7/5250-4	12x12	[0] _{8T}	8	
IM7/5250-4	12x12	[±45] _{2S}	8	2 ea
IM7/5250-4	12x12	[0] _{12T}	12	
IM7/5250-4	12x12	[±30/90 ₂]	8	2 ea
IM7/5250-4	12x12	[0 ₂ /90 ₂]	8	
IM7/5250-4	6x12	[0] _{5T}	5	
IM7/5250-4	6x12	[0] _{10T}	10	
IM7/5250-4	6x12	[0] _{20T}	20	
IM7/5250-4	6x12	[0] _{30T}	30	
IM7/5250-4	6x12	[0] _{40T}	40	
IM7/5250-4	12x12	[0 ₂ /90 ₂] _{3S}	24	

TABLE 1 (Concluded)
COMPOSITES FABRICATED

Material	Panel Size	Orientation	No. of Plies	Remarks
IM7/5250-4	6x6	[0 ₄ /90 ₄] _{3S}	48	
IM7/5250-4	12x12	[0] _{8T}	8	
IM7/5250-4	12x24	[0 ₄ /90 ₄] _{3S}	48	
IM7/5250-4	12x12	[0] _{4T}	4	
IM7/5250-4	12x12	[90 ₂ /±30] _S	8	
XN70/RS-3	3x3	[0] _{6T}	6	
XN70/RS-3	6x9	[±45] _{2S}	8	
XN70/RS-3	6x9	[0 ₂ /90 ₂] _S	8	
XN70/RS-3	6x6	[0] _{4T}	4	
XN70/RS-3	6x9	[0] _{10T}	10	
XN70/RS-3	6x6	[0] _{20T}	20	
XN70/RS-3	6x6	[0] _{8T}	8	
XN70/RS-3	6x6	[0 ₂ /90 ₂] _S	8	
EB	8x8	[45/-45/-45/45] _T	4	
EB	6x6	[0 ₄ /90 ₄] _T	8	
EB	8x8	[±45] _S	4	
EB	6x6	[0/90] _T	2	
EB	6x6	[0 ₂ /90 ₂] _T	4	
AS4C-1919	12x12	[0] _{24T}	24	
AS4C-1919	12x12	[0] _{16T}	16	4 ea
AS4C-1919	12x12	[0] _{8T}	8	4 ea
AS4C-1919		[±45] _{2S}	8	
T300/Phenolic	6x9	[0] _{12T}	12	
T300/Phenolic	6x9	[0] _{8T}	8	
T300/Phenolic	6x9	[0] _{4T}	4	
SC1008/Phenolic	12x12	[90 ₂ /0 ₂ /X ₂] _S	12	
SC1008/Phenolic	12x12	[90 ₂ /0 ₂ /Y ₂] _S	12	
SC1008/Phenolic	12x12	[90 ₂ /0 ₂ /χ] _S	12	
SC1008/Phenolic	12x12	[90/0] _{2S}	8	

TABLE 2
COMPOSITE MECHANICAL TESTING FOR THE PERIOD OF 15 SEP 95 - 14 SEP 96

COMPOSITE	MECHANICAL TESTS				
	<i>Tension</i>	<i>Compression</i>	<i>Flex</i>	<i>Shear</i>	<i>Other</i>
AS4/3501-6	123	8	10	9	CTE-12
IM7/5250-4	166	8		3	
AS4C-1919	47		20	34	CTE-2
AS4C-1919/Hysol 9460				114	Thermal Cycle-23
AS4C-1919/Hysol 9460-9430				6	
Concrete			1		CTE-1
Concrete/Composite	4	2	12	29	
Concrete/Rebar			1		
Concrete/Rebar/Composite			5		
Concrete/Carbon Rod			2		
Wood/Carbon Rod Rebar			3		
Hysol 9460					CTE-2
CAT-B Neat	12		6		CTE-1; Compact Tension - 8
RB-47 Neat	14		6		CTE-1; Compact Tension - 10
3501-6 Neat	13		6		CTE-1; Compact Tension - 11
Carbon	34				
Sintered Carbon			24		
Carbon/Carbon	36				
Vapor-Grown Carbon Fiber	26	10	6	27	
PCP/Carbon	6				
Titanium					CTE-3
Titanium Silicate					CTE-1
Invar					CTE-3

TABLE 2 (Concluded)

COMPOSITE MECHANICAL TESTING FOR THE PERIOD OF 15 SEP 95 - 14 SEP 96

COMPOSITE	MECHANICAL TESTS				
	Tension	Compression	Flex	Shear	Other
IM6/3501-6	18				
Radel 8320/T650-42	3				
P100 HT/954-2A					CTE-14
Graphitic Foam		19			
Carbon/Phenolic	5				
AS4/Phenolic	2				
P6 111/Phenolic	1				
P6 111/Epoxy	2				
EL F6/Epon 862	4				
Steel/Adhesive			51		
Glass/Epoxy	6	2	2		
IM7/RB-47	42		32		CTE-2
XN70/RS3	21		3		CTE-8
T300/938 (Tube)		3	1		
Aluminum (Tube)		2	1		
Aluminum/Adhesive				DCB-1	
Cyanate				6	
Bamboo Skewers	5				
Carbonized Bamboo Skewers	5				
Graphite/Toughened Epoxy	6				

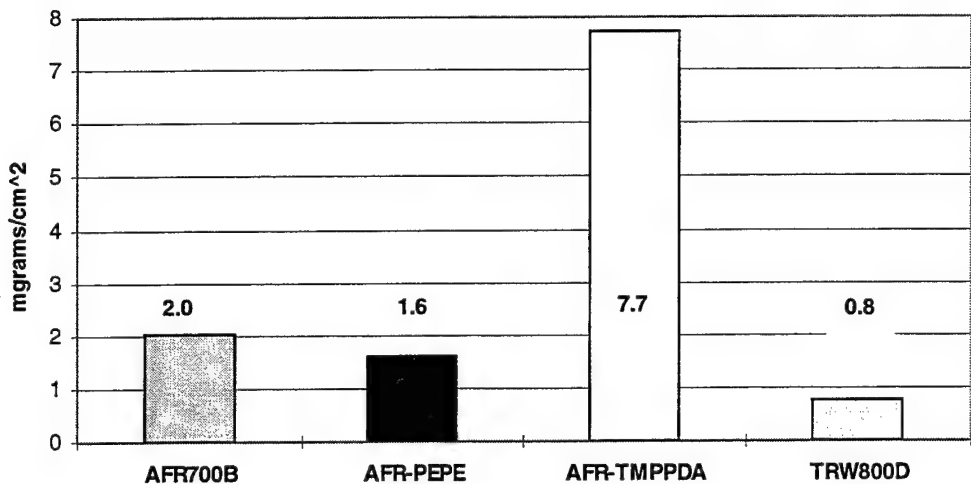


Figure 1. Weight Loss per Unit Area of Neat Resins at 371°C After 100 hours.

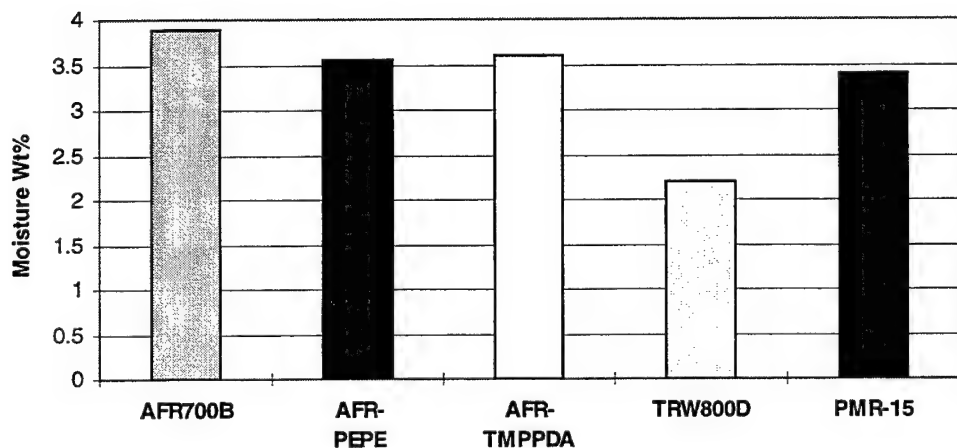


Figure 2. Equilibrium Moisture Content of Neat Polyimides at 85°F/85RH.

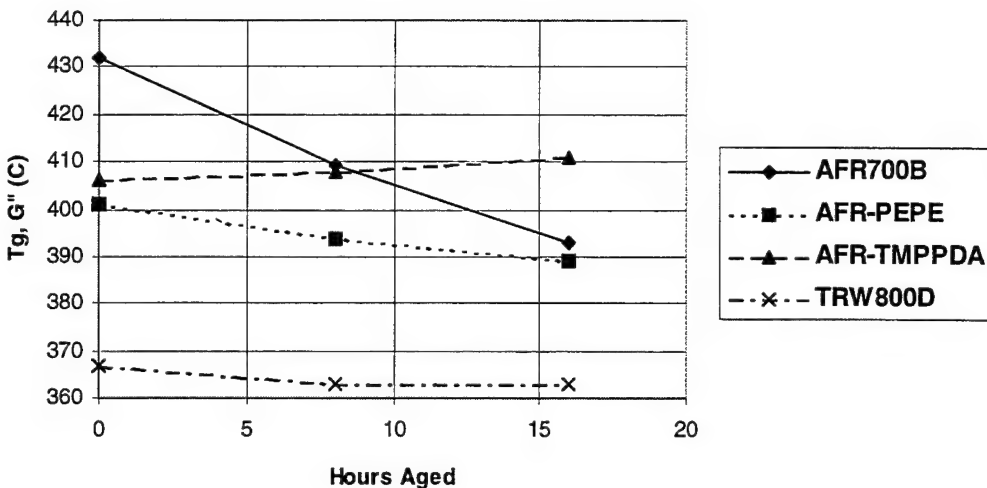


Figure 3. Glass Transition Temperature of Polyimides After Exposure to Saturated Steam at 150°C.

TOS testing was conducted to determine if possible contamination from the metal tooling will affect the thermal oxidative stability of the composites. Ten one-inch-square samples were prepared from each laminate and subjected to 371°C in a convection oven for 75 hours. Samples prepared from the laminate cured on the Kapton®/Teflon®-covered tooling had a weight loss of 0.54 percent, while samples cured on the Monocoat E-150 coated tooling had a weight loss of 0.93 percent. The samples cured on the Monocoat E-150 coated tooling had severe resin oxidation on the tool side, while the other samples showed little change.

1.4.3 E-Beam Cure Epoxies

A free-radical, E-beam-cured carbon/epoxy sample, AS1, was scanned at 2°C/min in the Rheometrics (Figure 4) up to 250°C. The G" peak occurred at 145°C. A subsequent rescan showed an increase in the G" peak to 160°C. These data support the claim that E-beam-cured epoxies will thermally advance. In the same vein another E-beam cure epoxy, RB-47, was held isothermally at 180°C for six hours and retested for Tg advancement. In this case the Tg increased from 148°C to 175°C (Figure 5).

The viscosity profile of a third E-beam-curable epoxy, CAT-B, was determined as shown in Figure 6. The resin begins to cure at approximately 180°C during a temperature ramp

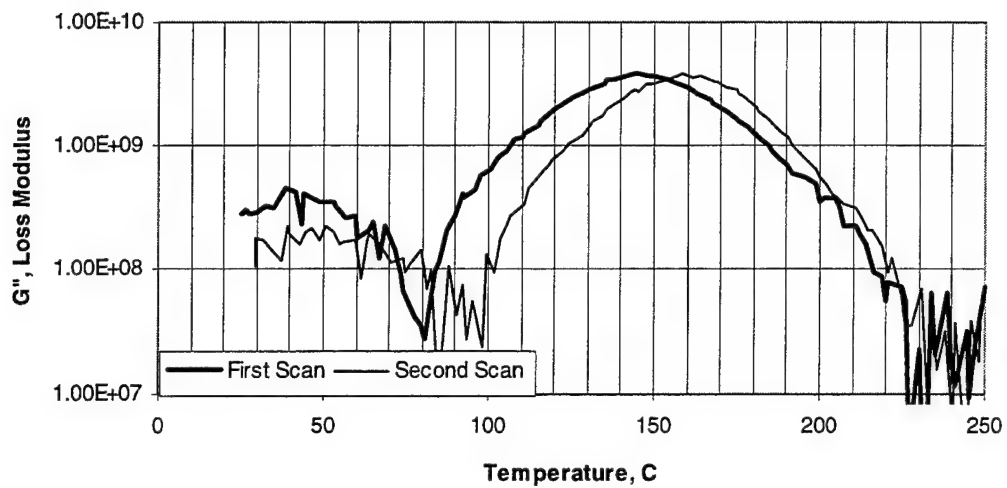


Figure 4. Thermal Advancement of AS1-Free Radical E-Beam-Cured Epoxy.

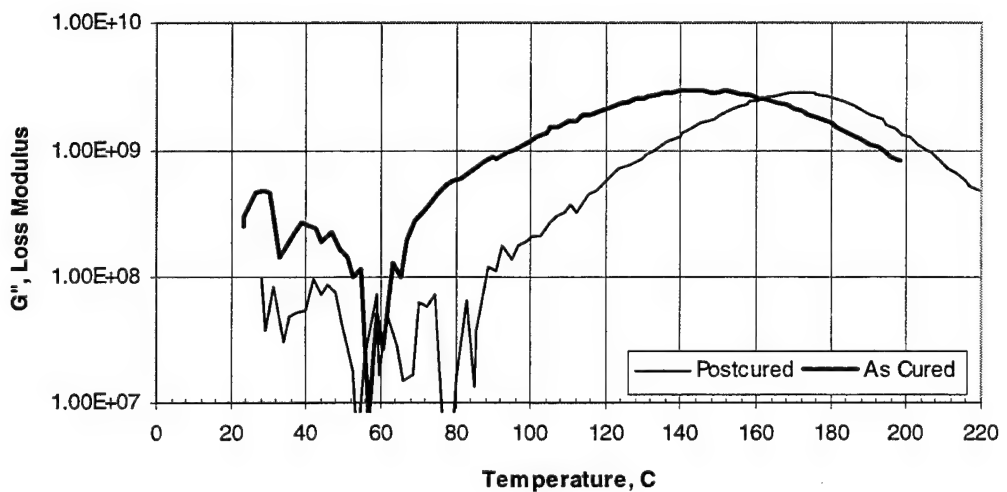


Figure 5. Thermal Advancement of RB-47, E-Beam-Cured Epoxy After 6 hours at 180°C.

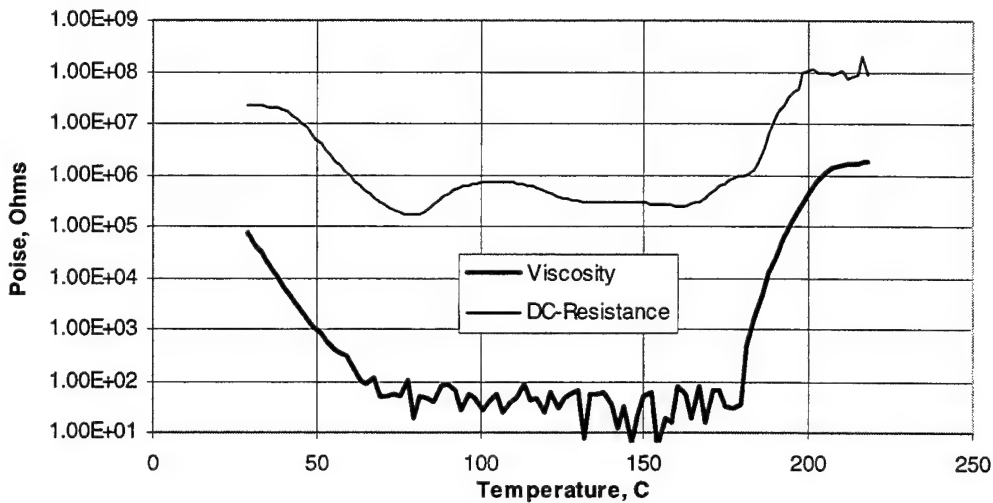


Figure 6. Parallel Plate of CAT-B, E-Beam-Curable Epoxy.

of 2°C/min. A dc-resistance measurement taken during the sweep indicates that such a sensor would be useful for monitoring the cure state. An isothermal hold conducted on the resin at 100°C (Figure 7) shows that the viscosity remains in the range of 3-4 poise, even after eight hours. This resin would be ideal for RTM processing when long flow times are required.

1.4.4 Crystallinity of SuperImide Matrix Resins

Two samples of SuperImide resin powders (#203 and #204) were examined by x-ray diffraction (XRD) and found to have the same crystalline peaks observed in the SuperImide and TRW800 composites. The crystallinity was determined using the AFR600 resin powder as an amorphous standard. Sample #204 was 20 percent crystalline and #203 had slightly higher crystallinity. The higher crystallinity was expected from #203's sharper diffraction peaks. The crystalline peaks in the SuperImide XRD scans can be seen in Figure 8 and compared to the broad amorphous halo of AFR600.

An additional SuperImide powder sample (reportedly noncrystallizable) was analyzed by x-ray diffraction for crystallinity along with several samples (made from this original powder) processed to various temperatures. A total of six samples of the SuperImide neat polymer were analyzed by x-ray diffraction. These samples consisted of (1) the as-received powder; (2) powder which had been heated to 450°C and then cooled to ambient in the DSC (10°C/min heating and cooling rates); powders pressed into films at (3) 288°C (550°F), (4) 316°C (600°F), and (5) 343°C (650°F); and (6) a postcured film (standard composite processing

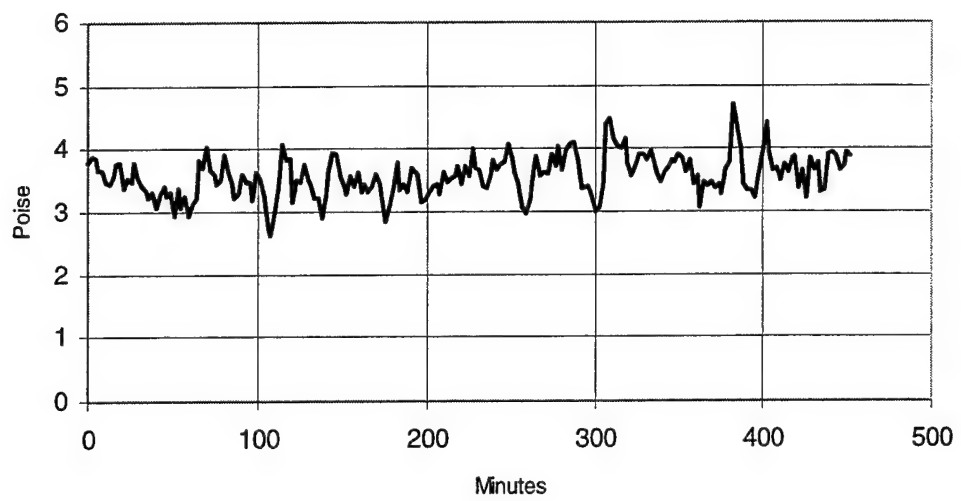


Figure 7. Parallel Plate of CAT-B Epoxy During a Hold at 100°C.

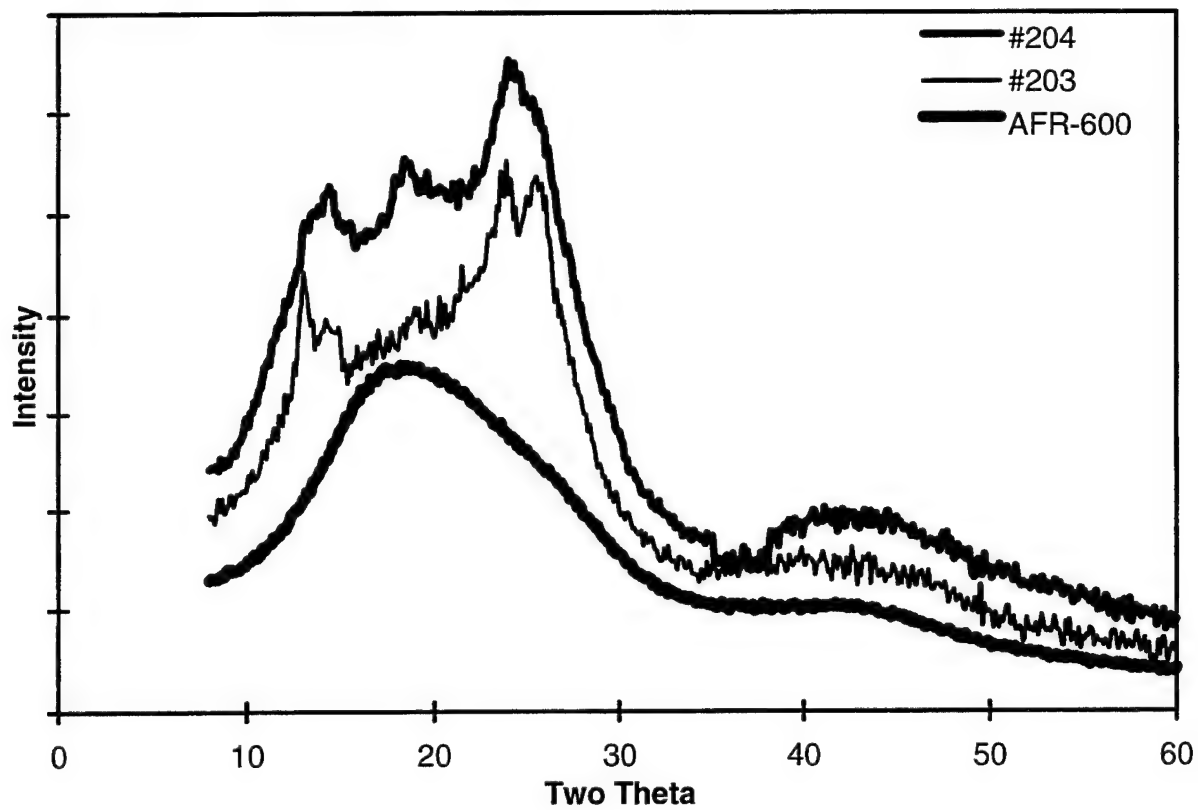


Figure 8. XRD Scans of SuperImide 800 and AFR600 Powders.

conditions). The DSC of the powder was obtained to see if any recrystallization peaks could be observed and to get sample #2.

The original, unprocessed powder (1) showed two small peaks around $25^\circ 2\theta$ amounting to only two percent of the total intensity. This represents an identifiable crystalline phase but at a level too low to quantify. The film plaques (3-5) pressed at 550°F , 600°F , and 650°F showed increasing degrees of crystallinity: the diffraction peaks in sample #3 (near $25^\circ 2\theta$) increased to about five percent crystallinity, the diffraction of #4 sample showed peaks at lower angles of $12\text{--}15^\circ 2\theta$ as well as the growth of the 25° peaks for a degree of crystallinity of 20 percent, while samples #5 and #6 had similar degrees of crystallinity to #4 but with better defined diffraction peaks indicating larger and more perfectly developed crystals. The XRD scans of these samples can be seen in Figure 9.

The powder, which was recovered from the DSC pan, had not melted together (still flowed freely). There was a heat of reaction or melting endotherm during heat-up, but this occurred over a large temperature range which is not typical of a melting peak. On cool down there was a small baseline shift but no recrystallization peak.

The DSC sample (#2) showed peaks at both the higher and lower angle regions but with a degree of crystallinity near five percent. The low degree of crystallinity in this sample may be a result of slow crystallization kinetics which explains why zero crystallization has been reported by the producers in the past. This low level of crystallization would also explain not observing any peak on cool down in the DSC. The samples processed above 300°C all show significant crystallinity but have also spent much longer times at elevated temperatures which would allow the crystallization to take place. These results are summarized in Table 3.

1.4.5 PEPE End-Capped AFR700 Resin

Processing problems with the PEPE end-capped AFR700 resin (AFR-PEPE-2) were similar to the problems encountered with the semicrystalline SuperImide resins. For this reason XRD was performed on that resin. The AFR-PEPE-2 was indeed found to have a significant crystalline content. Since the AFR backbone has never been observed to crystallize, it is the end-caps in this material that can and do crystallize.

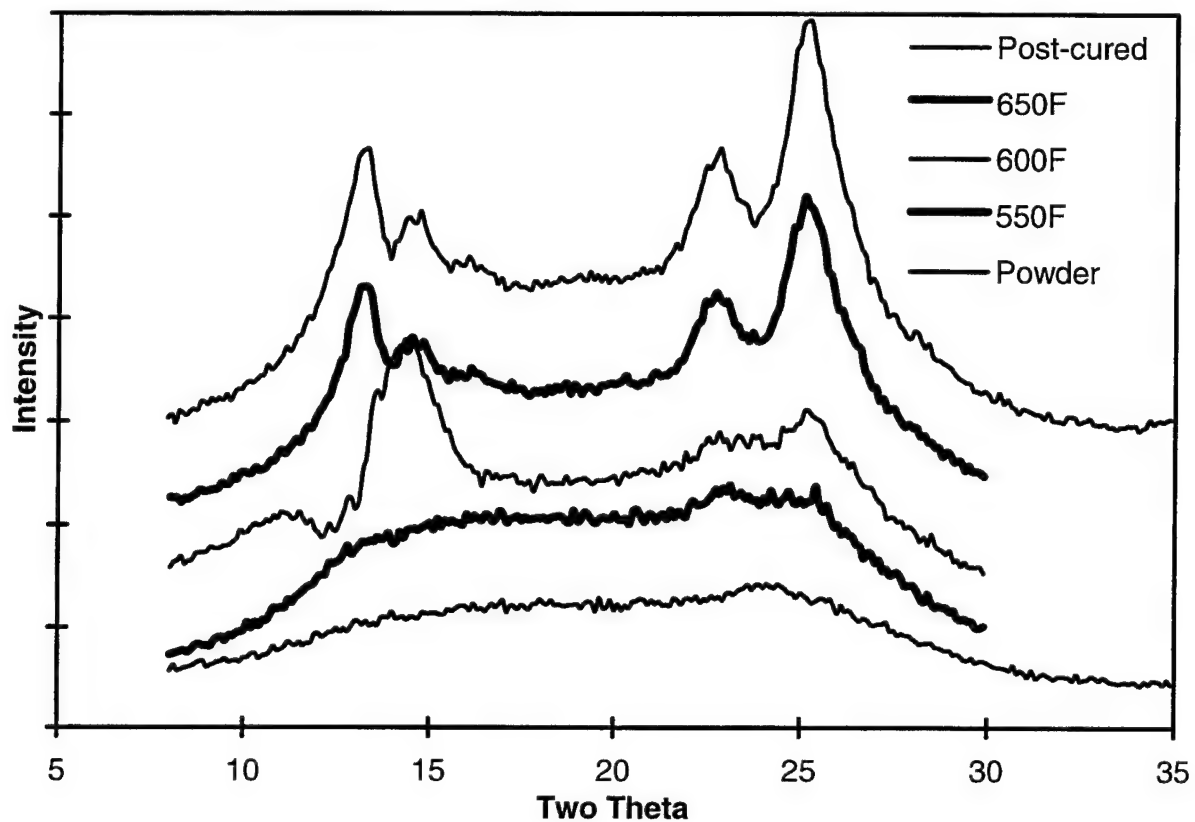


Figure 9. XRD Scans of SuperImide Resin Processed to Various Temperatures.

TABLE 3
SUPERIMIDE CRYSTALLINE PEAKS AND CRYSTALLINITY IN NEAT RESIN
SAMPLES PROCESSED TO VARIOUS TEMPERATURES

Sample	Processing	Peaks ($^{\circ}2\theta$)		Degree of Crystallinity (%)
		12-15	25	
1	as Rec'd	no	yes	2
2	DSC (450°C)	yes	yes	5
3	288°C (550°F)	no	yes	5
4	316°C (600°F)	yes	yes	20
5	343°C (650°F)	yes	yes	20+
6	Postcured	yes	yes	20+

1.5 ELECTRON BEAM-CURED COMPOSITE MATERIALS

1.5.1 Characterization of Electron Beam-Cured Resins and Composites

In the electron beam cure of composites, high-energy electrons are used to initiate polymerization and crosslinking of the matrix resin. In addition to being more affordable than conventional thermal cure for many applications, this technique offers a number of unique advantages, including cure under ambient conditions (with consequent lower thermal residual stresses), high throughput, simultaneous cure of different matrix materials in the same component, and the one-piece fabrication of large structures such as cryogenic tanks. Although employed in the coatings industry for several years, this technique has only recently gained interest for aerospace applications. Several feasibility studies have demonstrated the inherent economic and technical advantages offered by electron beam cure for aerospace composite structures; however, the success of this technology is dependent on development of the appropriate material systems and processes. A study was conducted to assess the processing, properties, and performance of state-of-the-art electron beam-cured resins and their carbon fiber composites in comparison to those of a baseline thermally-cured counterpart. The resins selected were RB-47, a methacrylated epoxy resin that cures via a free-radical mechanism, and CAT-B, a mixture of epoxies derived from diglycidyl ether of bisphenol-A and cationically cured with a photoinitiator. The baseline for comparison was 3501-6, the thermally-cured epoxy workhorse of the aerospace industry. Composites of these resins, reinforced with AS4 and IM7 carbon fibers, were also evaluated.

1.5.1.1 Characterization of Neat Resins

Moisture absorption characteristics of the neat resins immersed in water at 23°C are shown in Figure 10. While the rate of absorption for RB-47 and 3501-6 is similar, CAT-B absorbs moisture at a slower rate. Thermal expansions of the neat resins over the temperature range of -100°C to 100°C are similar for the electron beam-cured (EBC) resins, with CTEs of 50.7 and 51.0 ppm/°C for CAT-B and RB-47, respectively, while 3501-6 has a CTE of 40.9 ppm/°C over the same temperature range. The thermal stability of the EBC resins from TGA scans in air and nitrogen is superior to 3501-6. While the rate of mass loss from 3501-6 increases sharply at around 320°C (in nitrogen), the EBC resins are stable up to about 380°C. From DSC scans of the EBC resins, there appears to be residual uncured material which cures thermally during the scan. From the ratio of the corresponding exotherm to that generated from the thermal cure of uncured liquid resin, the degree of cure of the EBC CAT-B panel was estimated at 89 percent. This is surprising, considering that an electron beam dose of 300 kGy

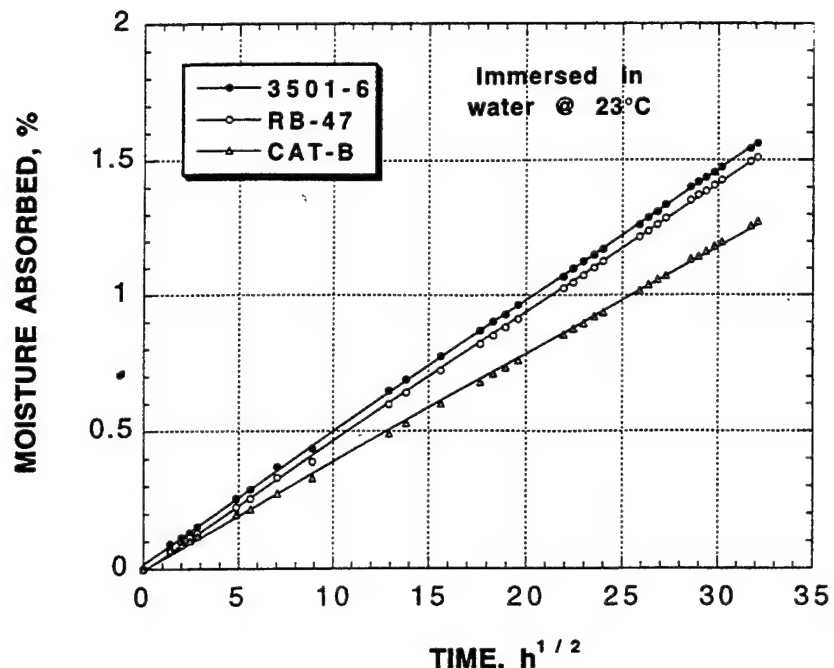


Figure 10. Moisture Absorption of Three Epoxy Resins Immersed in Water at 23°C.

was employed for this cure, in excess of the standard dose of 150 kGy. In comparison, the 3501-6 panel, fabricated in-house, had a degree of cure of 97 percent. No uncured resin was available for determination of degree of cure of the RB-47 panel. However from a comparison of DSC scans of cured and postcured RB-47, it appears that the cured panel evaluated was also not fully cured.

Dynamic mechanical analysis studies were conducted in a Rheometrics RDS II tester in the torsion mode. Representative dynamic storage moduli of the three resins as functions of temperature are shown in Figure 11. From this figure it appears that the RB-47 has a relatively low glass transition temperature (T_g) of 115°C. The T_g s of the CAT-B and 3501-6 are 160°C and 202°C, respectively. A better representation of this data is the plot of retention of storage modulus (on a linear scale) as a function of temperature, as shown in Figure 12, which allows a direct comparison to room-temperature stiffness. The temperatures corresponding to 50 percent retention of the room temperature stiffnesses occur at approximately 108, 133, and 185°C, respectively. Alternatively, at 125°C, RB-47, CAT-B, and 3501-6 retain 40, 68, and 80 percent of their room temperature stiffness. These data demonstrate the superiority of thermally-cured 3501-6 for elevated temperature applications.

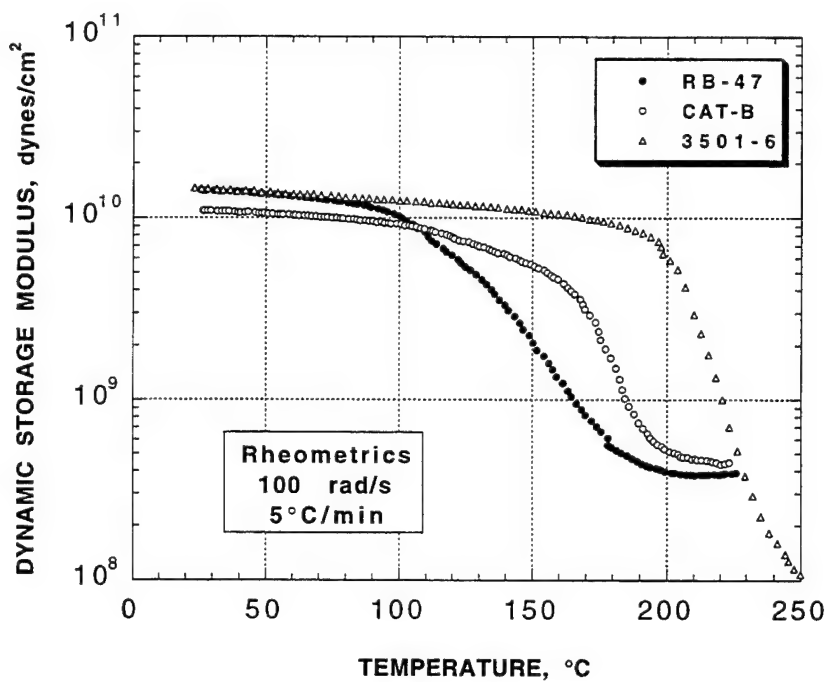


Figure 11. Dynamic Storage Moduli of Three Neat Epoxy Resins versus Temperature.

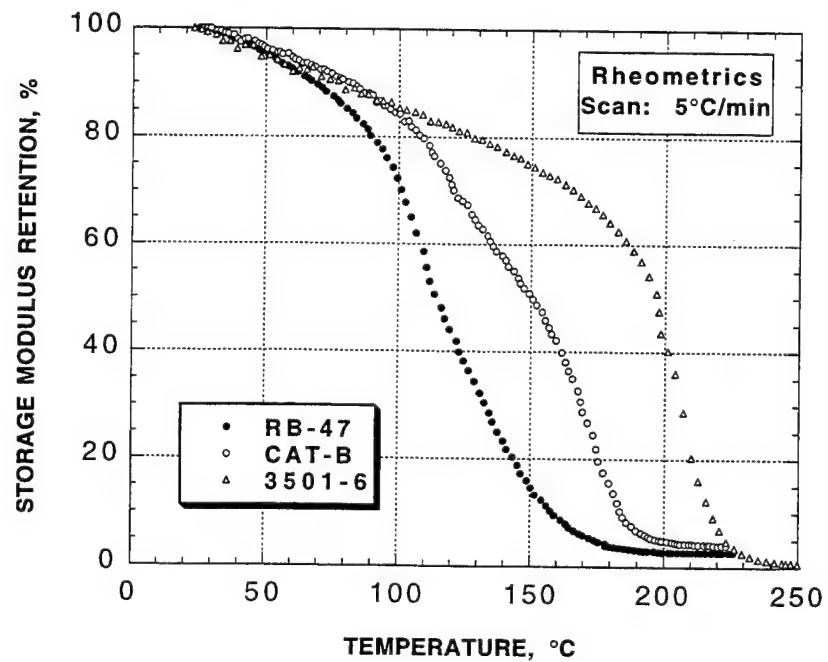


Figure 12. Retention of Dynamic Storage Modulus of Three Epoxy Resins as a Function of Temperature.

A possible application of this technology is in space structures because of the potential for greatly reduced residual stresses (and hence better dimensional stability) due to the ambient curing conditions. However, the lack of full cure in an electron beam raises a concern about the potential for dimensional distortion when cure advances (thermally) in the application environment. Space structures may cycle between -157°C and 121°C. Consequently, neat resin specimens were isothermally aged at 121°C to simulate the upper temperature of a space environment. The corresponding change in dynamic storage modulus with time is shown in Figure 13. After 64 hours of aging, the Tg increases by 14°C and 5°C for RB-47 and CAT-B, respectively.

Mechanical properties of the neat resins were determined under ambient conditions (RTD), at 121°C (ETD), at room temperature after boiling in water for 24 hours (RTW), and at room temperature after aging at 121°C for 72 hours. The tensile strength, tensile modulus, and fracture toughness for these resins are compared in Figures 14-16. As expected from the dynamic mechanical study, both of the EBC resins suffer a significant knockdown in tensile properties at 121°C, the RB-47 more so than the CAT-B. The fracture toughness, on the other hand, appears to increase with aging, possibly due to further (thermal) completion of cure.

1.5.1.2 Processing and Characterization of EBC Composites

Unitape prepreg was processed in-house on a drum winder using unsized AU4 (12K) fiber and neat CAT-B resin. The resin is sensitive to light, and its cure can also be thermally advanced. The minimum melt temperature for satisfactory fiber tow impregnation was found to be 120°C. Due to cure advancement at elevated temperature, the resin pot life is limited. This is illustrated in Figure 17, where the viscosity of the resin at three different temperatures is plotted as a function of time. It is apparent that at a processing temperature of 125°C, the limited pot life of the resin requires that prepregging be completed in three hours. This prepreg was cut and composite panels laid up. The processing challenge with these materials lies in achieving a void-free part through appropriate consolidation prior to cure, since the resin is immobile during cure. Panels were consolidated in a vacuum bag at elevated temperature for electron beam cure elsewhere.

Mechanical properties of a [0]₈ IM7/RB-47 panel (from Northrop) were evaluated. The results are summarized in Table 4. Poor fiber-matrix interfacial adhesion combined with poor matrix properties at elevated temperature yielded poor matrix-dominated composite properties, especially under hot/wet conditions.

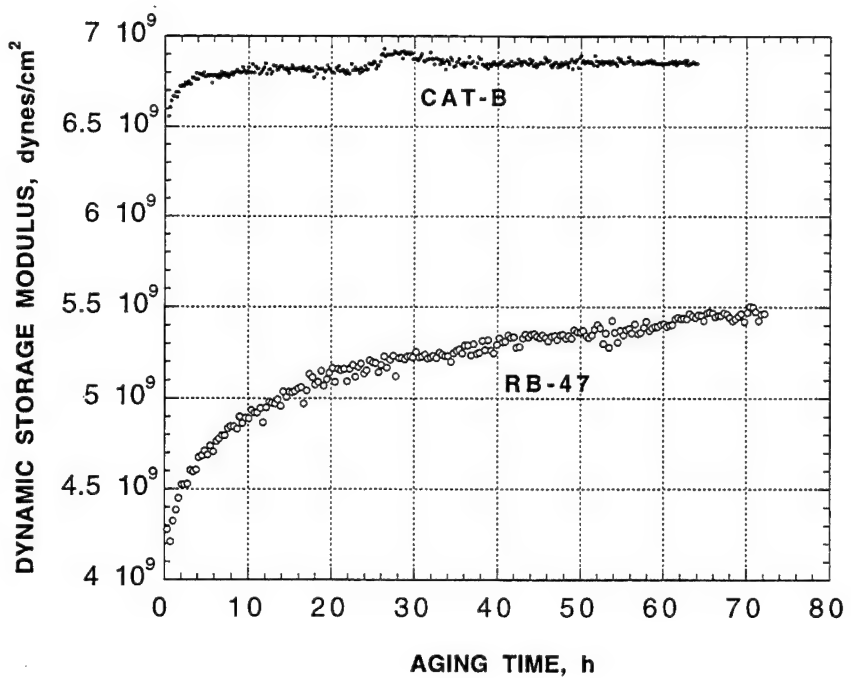


Figure 13. Change in Dynamic Storage Modulus of Two EBC Epoxies with Isothermal Aging at 121°C.

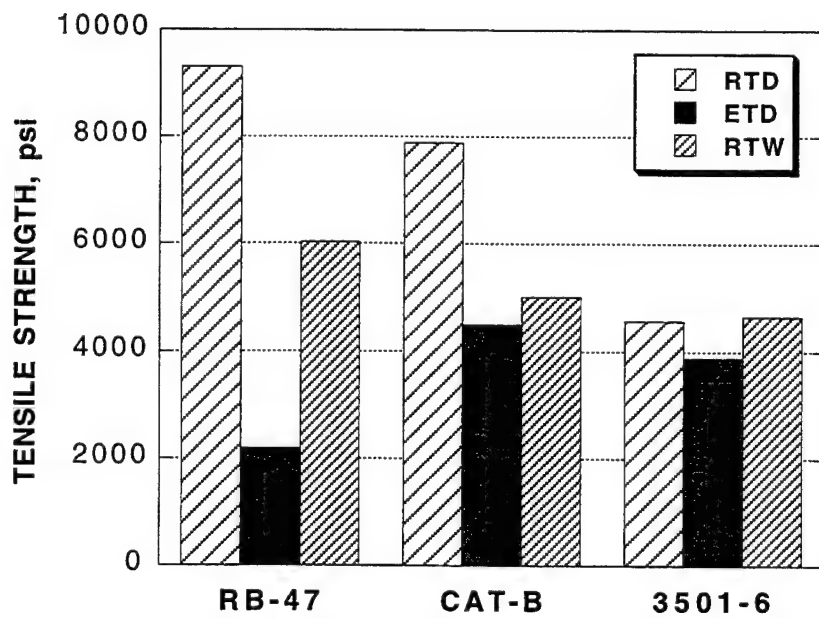


Figure 14. Epoxy Tensile Strength as a Function of Aging/Test Conditions.

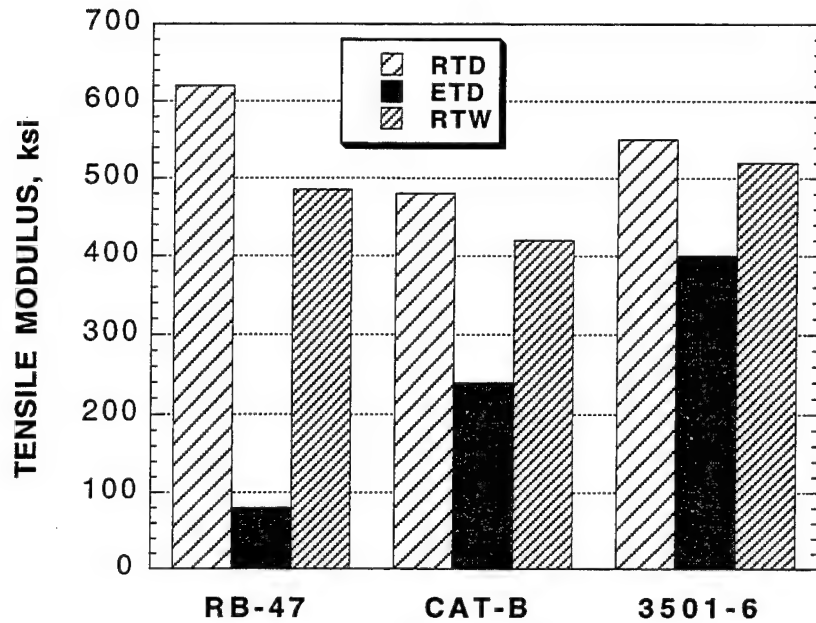


Figure 15. Epoxy Tensile Modulus as a Function of Aging/Test Conditions.

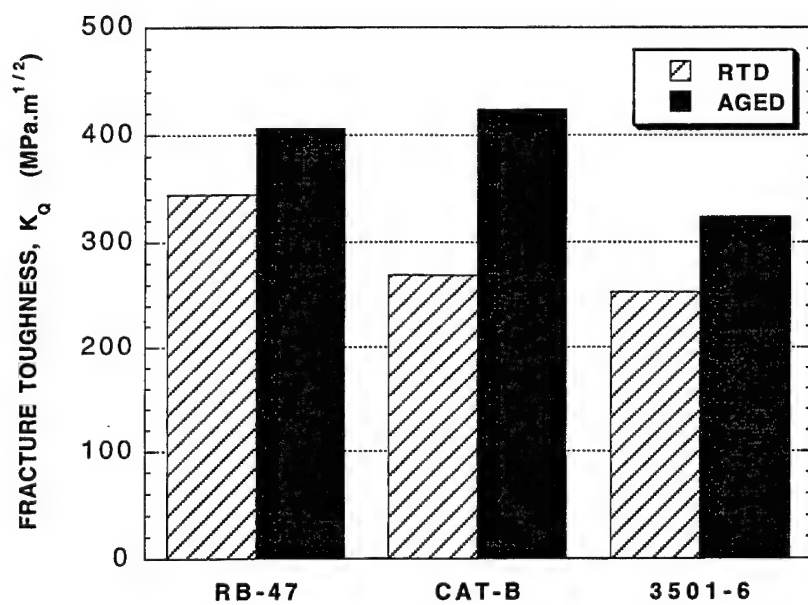


Figure 16. Epoxy Fracture Toughness as a Function of Aging/Test Conditions.

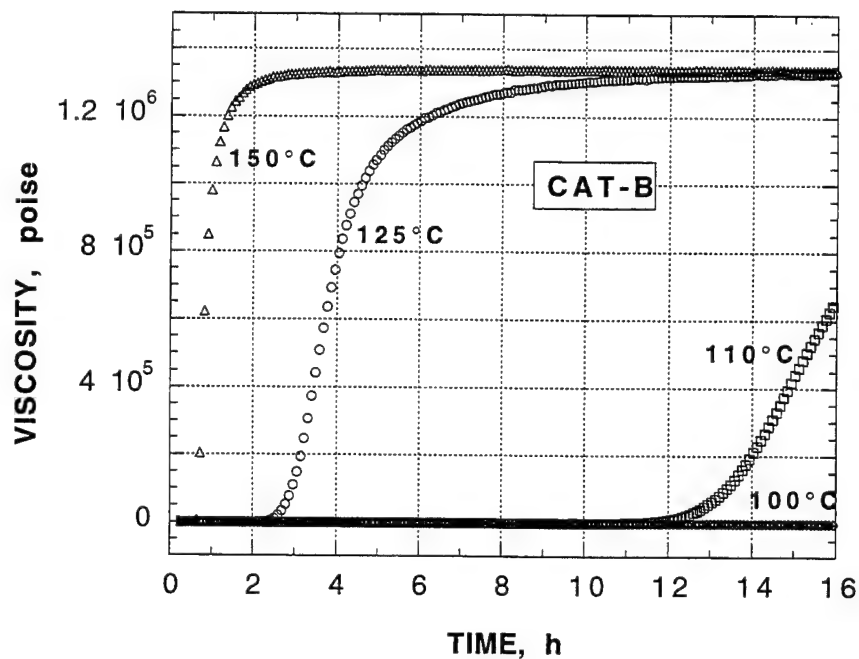


Figure 17. Dynamic Viscosity Data for CAT-B Epoxy Isothermally Aged at Various Temperatures.

TABLE 4
MECHANICAL PROPERTIES OF IM7/RB-47 COMPOSITE
COMPARED WITH A TYPICAL THERMALLY-CURED EPOXY COMPOSITE

PROPERTY	IM7/RB-47					IM7/8552*
	RTD	ETD (121°C)	RTW (23°C)	ETW (93°C)	ETW (121°C)	
Fiber Volume, %	56					62
Glass Transition Temp**, °C	116					
0° Tensile Modulus, Msi	24				24.3	24.5
0° Tensile Strength, ksi	225 [35]				190 [5]	385
90° Tensile Modulus, Msi	1.45	0.75			0.4	
90° Tensile Strength, psi	4725 [440]	2275 [510]	1680 [715]		440 [155]	
90° Flexural Strength, psi	6545 [775]		3500 [335]			
ILSS, ksi	11 [0.4]			3.6 [0.2]		18.6

* Hercules data

** From Storage Modulus

The two EBC resins evaluated do not stack up well against 3501-6, especially under hot and wet conditions. Resin formulations with higher glass transition temperatures are required. In addition, work is needed to optimize the fiber-matrix interface in these composites before the potential of these materials can be realized and their benefits utilized in commercial applications.

1.5.2 Electron Beam-Cured Composite Microscopy

Three E-beam-cured composite panels were examined by optical microscopy. As expected from the C-scans, all three samples had numerous voids scattered about the plies. Micrographs are shown in Figures 18-20. Sample JR-EB1 or panel #1, $[45/-45]_{2S}$ was mounted so that each of the 45 plies was viewed normal to the viewing plane. The lay-up for JR-EB3 (panel #3) was not listed on the C-scans like the first two but was observed to be $[0/90]_{4S}$ – the sample mounted to observe the 0° plies.

In Figure 18 panel #1 has long voids running parallel to the $+45^\circ$ fiber bundles – the void diameter is half the ply thickness. Elongated voids like the one shown in Figure 18b were found across the microscopy plug. It is not known whether this observation is universal or varies with location within the panel.

The uniaxial panel #2 (JR-EB2) in Figure 19 has many large voids (unknown if they are elongated parallel to the fibers). Some of the void diameters are several times larger than those observed in panels #1 and #3. The fiber bundle cross sections are also very irregular with matrix-rich areas in between. This panel did not look like a typical uniaxial composite which usually has identifiable plies.

In Figure 20 panel #3 has voids which look to be the same as those observed in panel #1 parallel to the 0° plies, but only the cross sections were visible in the plug as sectioned.

1.5.3 Characterization of Electron Beam-Exposed Carbon Fibers

Three fiber samples (AS-4, M60J, and P-100) were exposed to 10 megarads of electrons by SRL and returned to our laboratory for analysis. This short study was undertaken to determine if E-beam cure of composites might cause damage to the fibers and weaken the resulting composite. The XRD results showed no detectable differences between fiber samples exposed to electrons and the nonirradiated fibers. This includes crystallite size, orientation, and degree of graphitization.

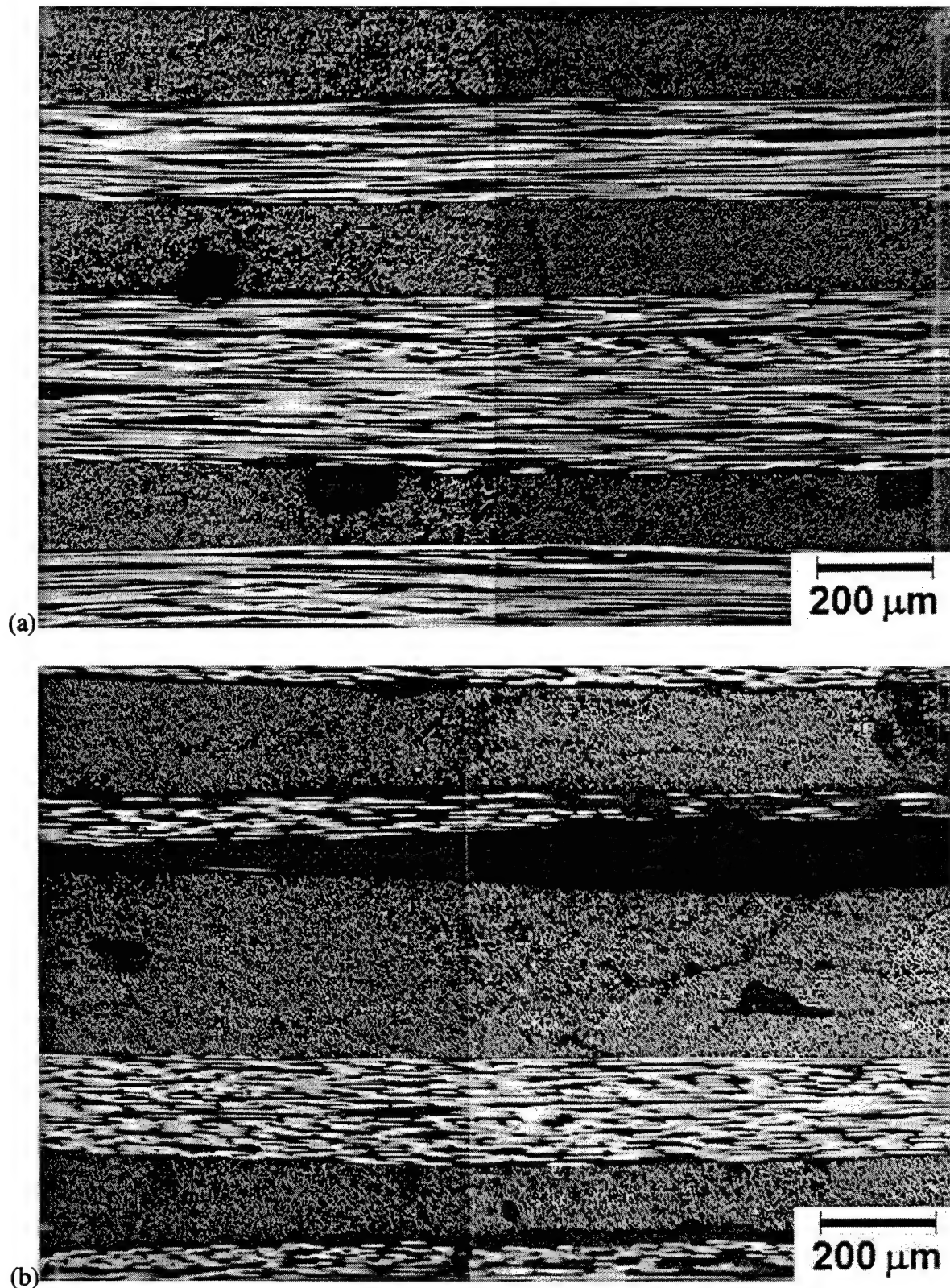


Figure 18. Optical Micrographs of Electron Beam-Cured Panel JR-EB1: (a) +45 Ply in Cross Section and -45 Ply Running Horizontal, (b) -45 Ply in Cross Section and +45 Ply Running Horizontal.

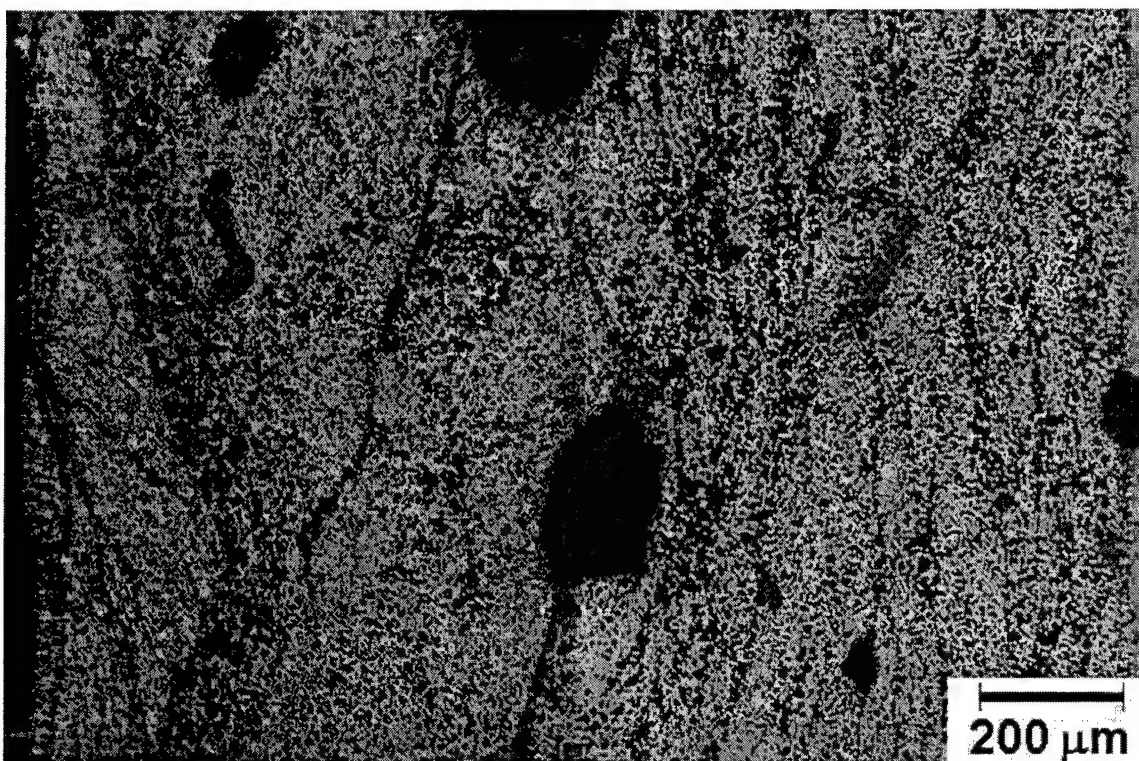


Figure 19. Optical Micrograph of Electron Beam-Cured Panel JR-EB2.

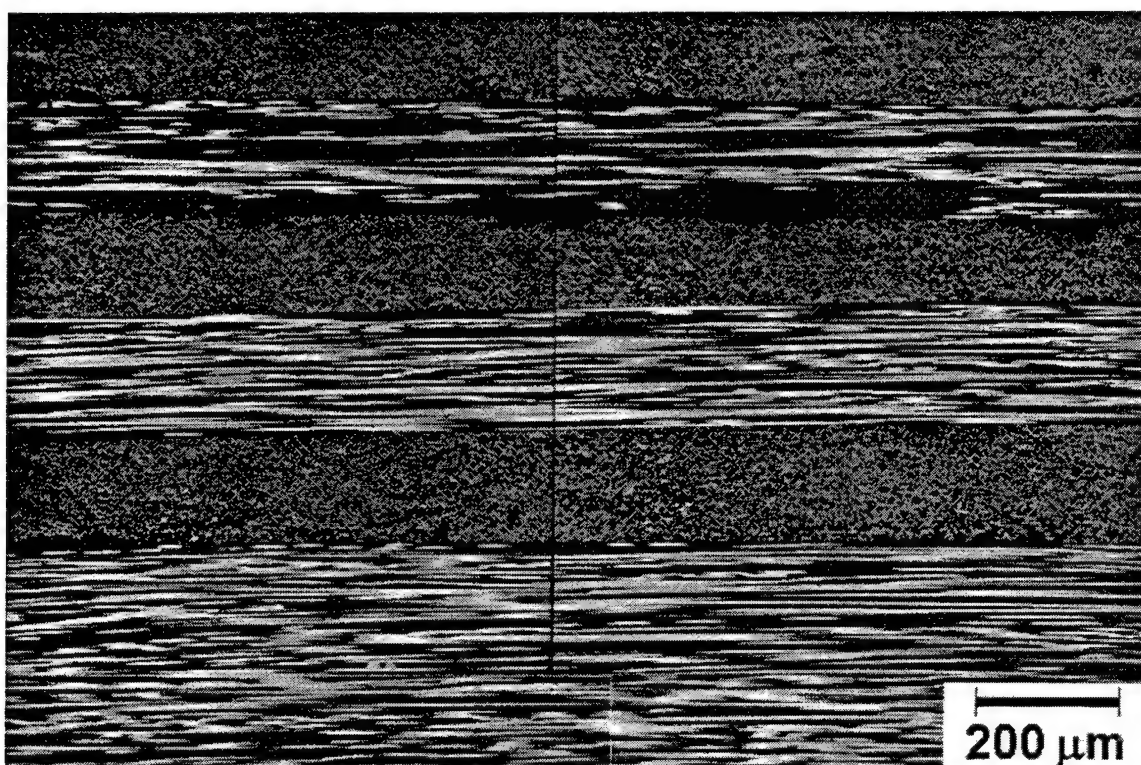


Figure 20. Optical Micrograph of Electron Beam-Cured Panel JR-EB3.

An SEM of these fiber samples shows some minor differences in that the irradiated samples appear to have some additional debris on their surfaces. This debris was visibly scattered randomly about the fibers and did not constitute a major portion of the surface. It appears to have spalled from the fibers during irradiation; the nonirradiated fiber surfaces were generally clear. The fiber cross sections were not affected by the irradiation.

In conclusion the fibers are not adversely affected by the energy levels of electrons used for composite curing. Some minor surface defects may occur, but the bulk of the fibers is unaffected.

1.6 COMPOSITES FOR INFRASTRUCTURE REHABILITATION

1.6.1 Laboratory Studies

An accepted method of repair of weak or damaged concrete structural members is flexural strengthening or stiffening with bonded steel plates. The advantages of this method over others such as external post-tensioning or additional supports are lower cost, ease of application and maintenance, elimination of special anchorages, and the ability to strengthen the structure while it remains in use. An important drawback of this structural system, however, is the potential for corrosion at the adhesive/steel interface with consequent reduction in the adhesive bond strength. Fiber-reinforced composites offer distinct advantages over steel as an externally-bonded plate reinforcement for concrete structural members. (CFRP) in particular have higher specific stiffnesses and strengths, demonstrate excellent durability in a saline environment, are resistant to corrosion by acids, alkalis, and salts over a wide range of temperatures, and can be tailored to the desired mechanical properties. Although the CFRP itself is much costlier than steel, the lighter weight and better corrosion resistance can result in significant reductions in fabrication and long-term costs. Research was recently initiated in this area with studies on eight-foot beams to develop appropriate materials and processes for field rehabilitation of concrete bridge beams [2]. This study was then extended to larger beams and actual field trials.

1.6.1.1 Materials and Processes

Based on earlier laboratory work, the materials selected for the field trials were a commercial graphite/epoxy composite material (AS4C/1919 from Hercules, Inc.) and a two-part ambient-cure epoxy paste adhesive (Hysol EA 9460 from Dexter Hysol, Inc.). Composite plates of various dimensions with $[0]_4$ and $[0]_5$ lay-ups were fabricated in a vacuum bag at 121°C. These composites were cured between porous Teflon-coated release plies to

impart a rough surface texture to the plate which aids in obtaining a good interfacial bond. Composite/composite lap shear tests, however, showed that this surface preparation was inadequate. Mechanical abrasion with a 240-grit sandpaper, followed by a water wash and an acetone rinse, was therefore employed to increase the lap shear strength to 2400 psi. Three concrete beams tested in this study were of the same dimensions and cast at the same time as those used to construct the bridge deck used in the field demonstration. The relevant composite, concrete, adhesive, and reinforcing steel properties are given in Table 5. The cross-sectional dimensions of the concrete beams as well as the details of the steel reinforcement are shown in Figure 21.

Composite joints are considered both practical and necessary in field rehabilitation of concrete structures, and bonded joints were therefore introduced into the test beams at a number of locations. The joint of choice for this application (based on earlier studies [2]) was a doubler, and the same adhesive was employed for the joint as that used to bond the composite to concrete. Each joint had a composite overlap of 15.2 cm, and four such joints were utilized in each beam as shown in Figure 22. The rationale for the selection of the number and location of joints was to limit the length of a composite plate to 1.83 m (for convenience of transportation to the work site) and to avoid having a joint directly below a loading pin in the flexural test. Three beams were tested in this study. The first beam was tested without any composite reinforcement to obtain baseline concrete data. The surfaces of the other two beams were prepared prior to composite bonding by removing loosely-bound cement with a wire brush and vacuuming residual dust and debris. The second beam was flipped to allow the tensile surface (i.e., the face nearer the reinforcing steel) to face upward to facilitate composite plate bonding. Composite plates were bonded overhead to the suspended third beam to simulate application conditions in the field.

The composite plates were bonded in three stages as depicted in Figure 23. In each stage the two-part adhesive was mixed in accordance with the manufacturer instructions, applied to the beam surface, and overlaid with the composite plates. To limit the exotherm generated during adhesive mixing, the required adhesive for each stage was mixed in two separate batches. A vacuum bag was applied to this assembly for at least 24 hours to generate a pressure during adhesive cure of 50-67 kPa. An additional period of at least two days was allowed between the final stage and testing to ensure that the adhesive had cured to its full strength.

TABLE 5
RELEVANT PROPERTIES OF CONSTITUENTS FOR
INFRASTRUCTURE REHABILITATION

PROPERTY	COMPOSITE PLATE*	STEEL REBAR	CONCRETE	ADHESIVE
Yield stress, ksi	-	60	-	-
Tensile modulus, Msi	20	29	-	0.4
Tensile strength, ksi	280	-	-	4.4
Elongation at break, %	1.4	-	-	3.5
Compression strength, ksi	-	-	4.5	

* Fiber volume = 60%

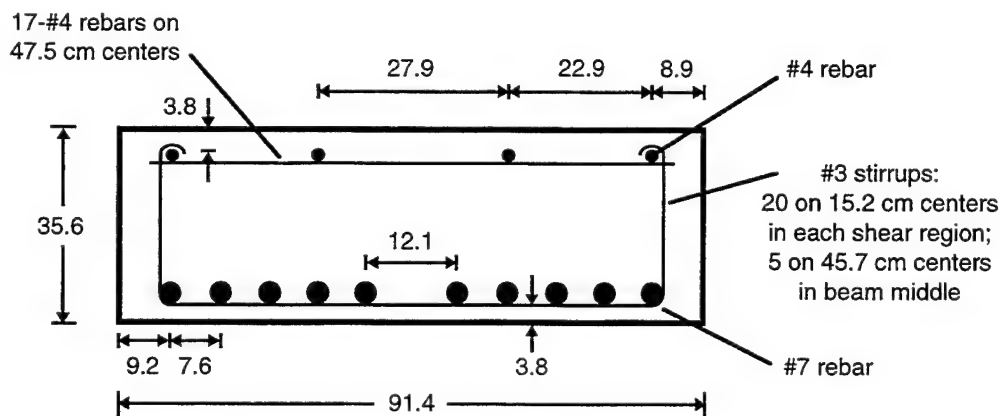


Figure 21. Cross Section of Concrete Beam Used in Lab Studies and in the Field (dimensions in cm).

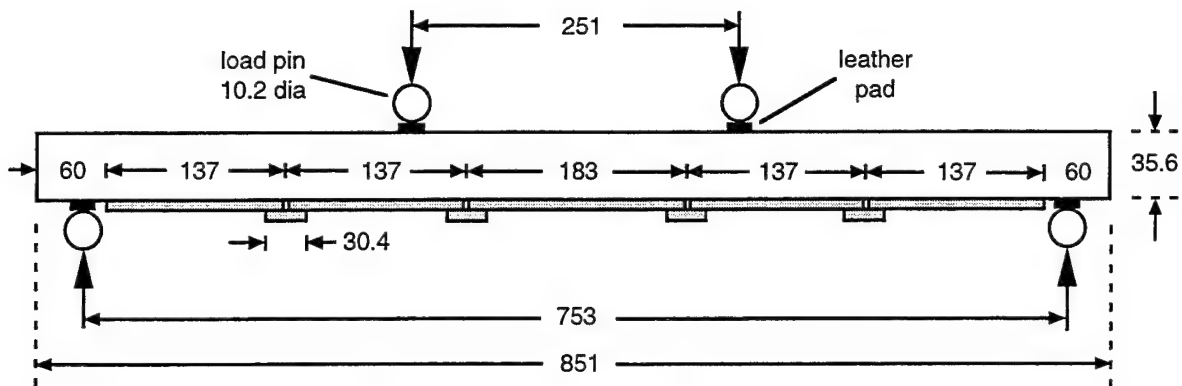


Figure 22. Sketch of Composite-Reinforced Concrete Beam (dimensions in cm).

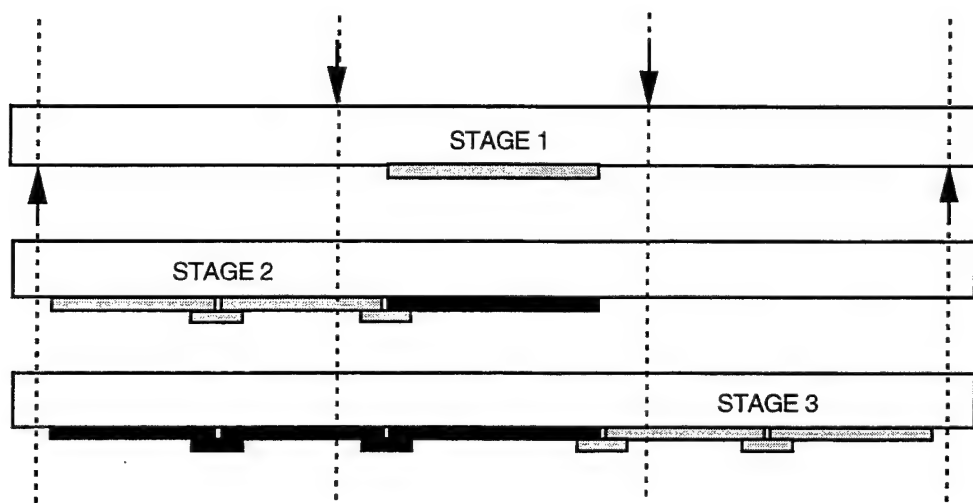


Figure 23. Three Stages in which Composite Plates were Bonded to a Concrete Beam. The arrows show loading and support points for flexural tests.

1.6.1.2 Performance Evaluation

The three beams were tested in four-point flexure (one-third point loading), in accordance with ASTM C78-84, at a crosshead displacement of 7.5 mm/min. Leather pads, 9.5 mm thick, were placed between the loading pins and beam to prevent local crushing. The central deflection of the beam was measured as a function of applied load. In the analysis the cross-sectional areas of the steel rebar and composite plate were replaced with equivalent areas of concrete (based on the ratio of moduli) at the corresponding locations. The usual methods for analysis of an elastic homogeneous beam were then applied to locate the neutral axis of this equivalent concrete beam and calculate the moment of inertia. The analysis assumes that the composite-to-concrete bond remains intact up to final failure which was confirmed from experimental observations.

Failure of the control beam under flexural loading proceeded as expected, initiating with tensile cracks on the beam's lower face at a bending moment of about 100 kN-m. Above this load the bending moment increased linearly with beam deflection up to approximately 400 kN-m which marks the onset of yielding of the steel rebar. Beyond this point the beam continued to deflect with no significant increase in bending moment, with the concrete eventually failing in compression at a maximum bending moment of 435 kN-m. The calculated bending moment agrees fairly well with the experimental data, with the loads for concrete compressive failure and steel yielding predicted to be in close proximity to each other.

The [0]₄ composite plate bonded to the lower face of the second beam covered 86.4 cm of the beam's 91.4-cm width. The measured and calculated central deflections under flexural loading are shown in Figure 24 as a function of bending moment. The calculated curve follows the experimental data fairly well but predicts compressive failure of the concrete at approximately 500 kN-m, which is significantly lower than the maximum bending moment measured. Failure once again initiated through tensile cracks in the concrete. This was followed by longitudinal splitting of the composite plate in the region of maximum bending moment as the load increased. Ultimate failure was precipitated by fracture of the concrete in compression, preceded by spalling at the top face. This was followed instantaneously by failure of the composite/composite lap at an inner doubler joint with accompanying failure in the concrete layer near the composite, causing it to peel away with the fractured concrete still adhering to it. This sequence of failure events is illustrated in Figure 25. This failure scenario confirms the existence of a strong bond between the concrete and composite in this specimen. On the other hand, failure at a lap instead of composite tensile fracture (after the concrete has failed in compression) suggests the need to improve the composite/composite bond. Ultimate failure

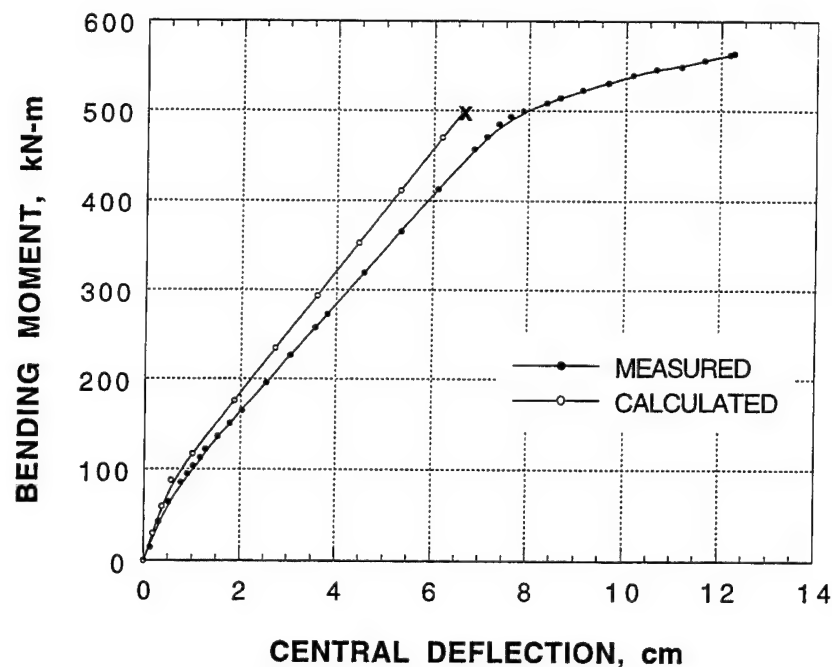


Figure 24: Experimental and Calculated Bending Moments vs. Central Deflection for a Concrete Beam Reinforced with Bonded $[0]_4$ CFRP Plates.

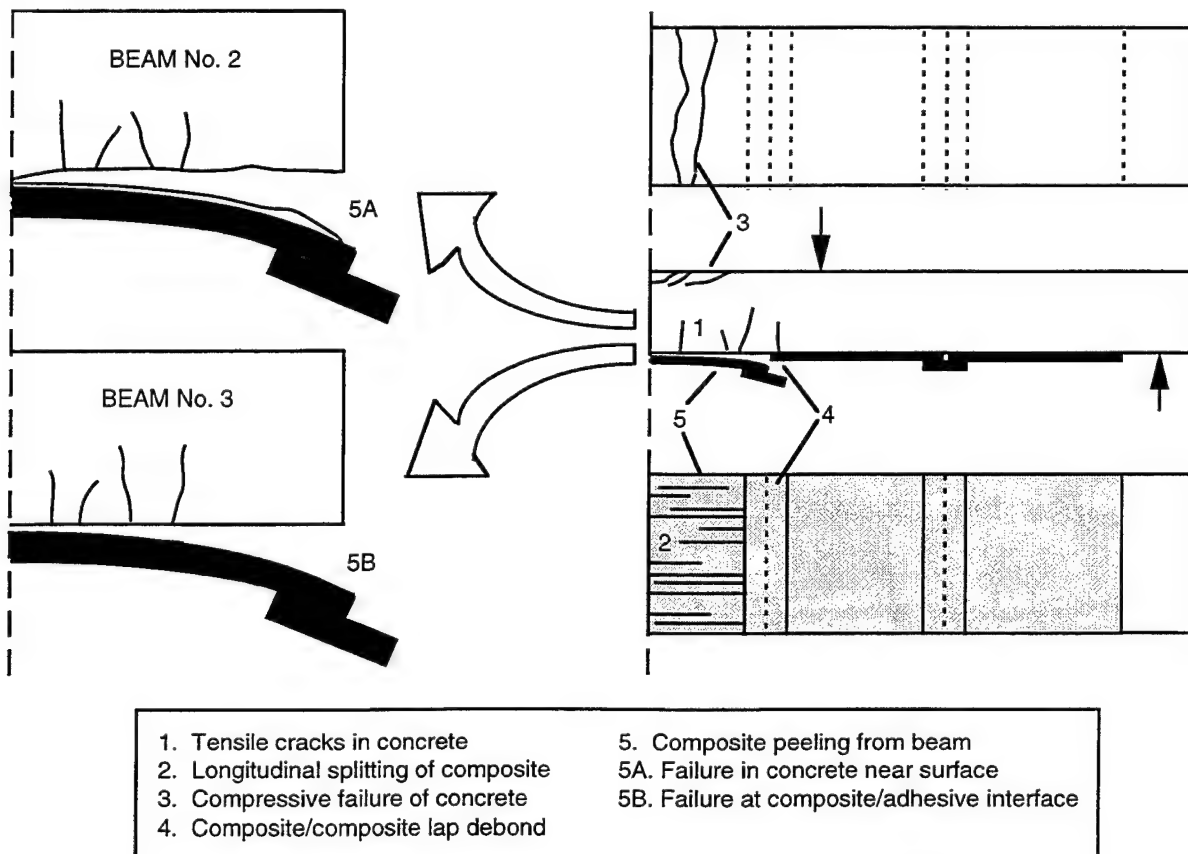


Figure 25. Sketch of the Sequence of Failure Modes in the Flexure of a Concrete Beam Reinforced with Bonded Composite Plates.

occurred at a maximum bending moment of 565 kN-m, representing a 30 percent increase in moment capacity over the control beam.

To simulate the procedure of bonding composites to the lower faces of concrete beams in bridges, composite plates were bonded overhead to the third test beam. When the beam sides are inaccessible for sealing a vacuum bag, as is the case in a bridge deck, the bag must be sealed against the same (lower) face to which the composite plates are bonded. To provide space for the vacuum bag sealant on the sides of the composite plate, the plate width for this beam was reduced from 86.4 cm to 69 cm; the composite cross-sectional area was maintained the same as in the second beam by going from a [0]₄ to a [0]₅ lay-up. The sequence of failure events paralleled that observed in beam No. 2 with two notable exceptions. It is uncertain if ultimate failure was precipitated by compression fracture of the concrete or by failure of the composite/composite lap. It should be remembered that the 20 percent reduction in the composite width for this beam resulted in a 20 percent smaller composite/composite lap area compared to beam No. 2. Perhaps not coincidentally, the maximum bending moment at ultimate failure (for the same composite cross-sectional area), 530 kN-m, is also lower than that obtained with beam No. 2. Examination of the peeled composite plate following final failure also showed predominantly clean interfacial failure between the composite and adhesive layer (Figure 25) unlike the case with beam No. 2.

From a comparison of the experimental data for all three beams tested (Figure 26), it is apparent that the region of composite to reinforced concrete utilized in this study did not enhance beam stiffness. In analyzing the results from these tests, it was concluded that due to the difficulty in working overhead with beam No. 3, the application of adhesive and the adhesive bond obtained were not as efficient as with beam No. 2, resulting in the observed interfacial failure between composite and adhesive. Up until ultimate failure (which occurred at a bending moment 22 to 30 percent higher than the control beam), however, no composite peeling was observed either at the ends of the plate or the composite joints. These results validate the improvements seen in the earlier study [2] on scaled-down concrete beams and provide the materials, process, and design for an approach to the rehabilitation of concrete beams.

1.6.2 Field Demonstration of Rehabilitation Scheme

One drawback to the use of composites in infrastructure is the lack of reliable accelerated aging tests and life prediction methodologies for the net structure in the intended service environment. In their absence field demonstrations that strictly monitor long-term

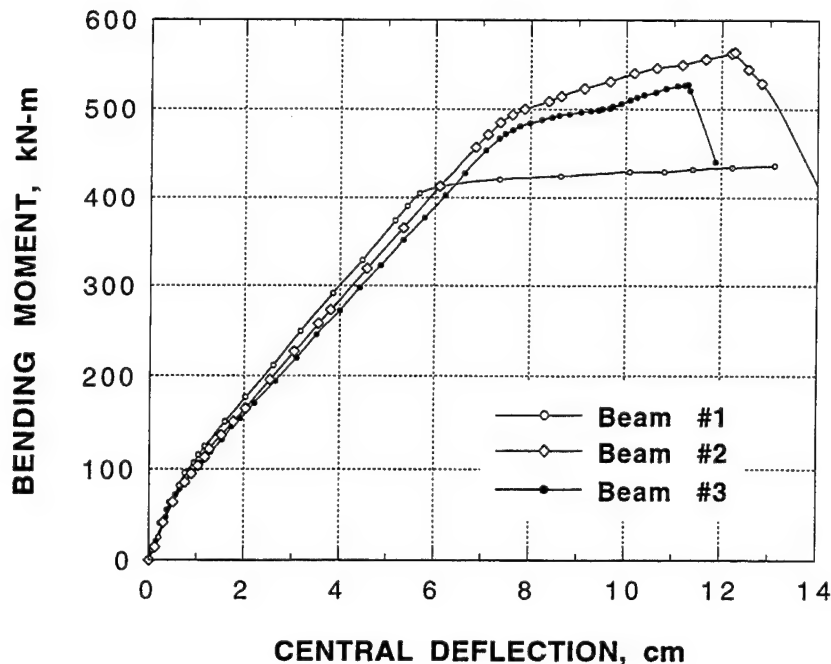


Figure 26. Comparison of Measured Bending Moments vs. Central Deflection for Three Beams. Beam 1: control, no composite; Beam 2: bonded $[0]_4$ plate; Beam 3: bonded $[0]_5$ plate.

durability of the composite material must be conducted. With the results and lessons learned from laboratory studies on 2.44-m beams [2] and the 8.51-m beams in this study, this technology was applied in the field to demonstrate the feasibility of strengthening concrete beams in a bridge deck with externally-bonded composite plates. The bridge, on Fear Not Mills Road in Butler County, Ohio was built in 1994 and has a single span with a conventionally-reinforced precast concrete box-beam superstructure and an asphalt wearing surface. The 10 box beams which comprise the deck have dimensions identical to those shown in Figure 21. The span of the bridge is 8.05 m center to center of bearing, and the width is 9.14 m face to face of the rail. Composite plates (with doubler joints) of the same design employed in beam No. 3 were bonded to each of the two exterior box beams of the bridge deck. The only difference from beam No. 3 was an increase in length of the composite/composite lap from 15.2 cm to 22.9 cm for this field application. The exterior box beams were selected because they will receive the most severe exposure to the natural environment as well as to gasoline, oil, deicing chemicals, etc.

Composites were once again bonded in three stages to each beam as depicted in Figure 23. The lower faces of the box beams were prepared by sandblasting to remove any outer weak cement layer, followed by a high-pressure water wash. All aggregate projecting below the

plane of the lower face was mechanically ground down. Pressure during adhesive cure was once again applied with a vacuum bag. Application of the various components that comprise the vacuum bag - the porous peel-ply, breather element, and the plastic bag itself - was facilitated by gluing them together, using a hot-melt adhesive gun, and raising this assembly for attachment to the sealant tape on the concrete. Vacuum was applied through conventional laboratory vacuum pumps, located either on the dry stream bed below the bridge or on the side of the road above, and connected to ports in the vacuum bag through flexible, lightweight vacuum tubing. One vacuum pump was employed for the first stage of the bonding procedure, while two pumps, one at each end of the composite plate assembly, were used for the next two stages. Based on the ambient temperature during bonding, the vacuum was maintained for a minimum of five hours.

The physical condition of the composite plates and the adhesive bond will be periodically assessed. In one year one of the exterior box beams (with the bonded composite plates) will be removed from the bridge and transported to the lab where it will be tested in flexure for comparison to the baseline beams (with and without bonded composites). In five to six years the other exterior beam will be similarly removed and tested. In addition to the composite plates bonded to the two outer box beams, two smaller [0]₅ composite plates (each measuring 122 cm x 69 cm) were bonded to an inner box beam. The first plate was bonded as described above, with pressure applied through a vacuum bag. Pressure during bonding of the second plate was applied mechanically through a thick section of plywood propped up firmly against the entire area of the composite plate. These composite patches will be retained on the structure to assess the influence of environmental exposure on the structural integrity of the adhesive bond over the long term.

1.7 CHARACTERIZATION OF POLYMER PROSTHETIC KNEE SOCKETS

Two samples of polymers used in prosthetic knee sockets were obtained from MLS for analysis by x-ray diffraction analysis (XRD). The results from these materials indicate that the major component of both has essentially identical degrees of crystallinity. The sample designated "B" from the failed socket, however, does show an additional component not observed in the control sample, #3. See Figure 27.

A crystalline peak of this additional component is seen as a shoulder near 24° on the large main-component peak between 25 and 26°. The amorphous halo is also visible, extending above and at a slightly lower angle than the main-component amorphous halo. The composition of the second component would have to be known to quantify its presence, but assuming a similar

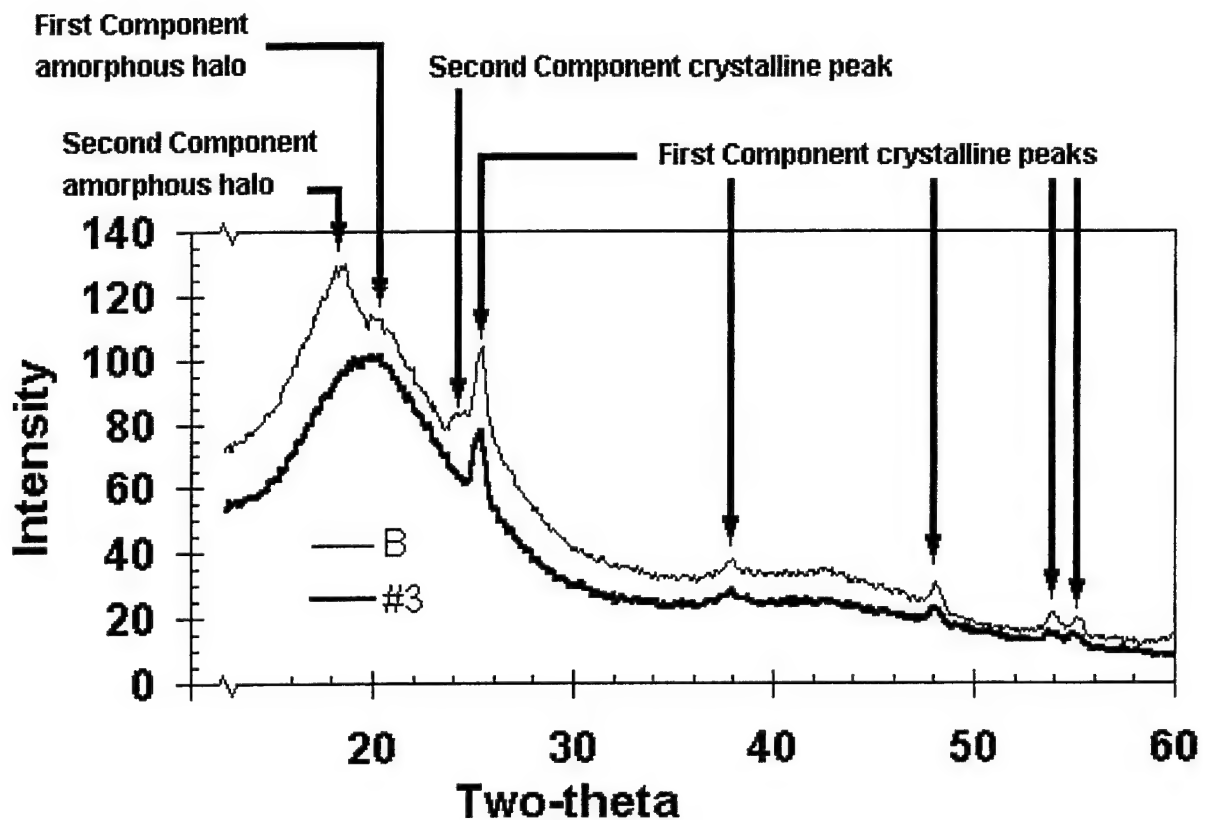


Figure 27. XRD Scans of the Two Prosthetic Material Samples.

composition to the main component, it was estimated that the second component constitutes about 10 percent of the total.

Since the absorption characteristics of the two samples are very similar, it is expected that the second component of "B" is organic rather than metallic or ceramic. Analytical tests other than XRD would be required to get more information about the composition of the contaminant in "B."

SECTION 2

MECHANICS OF POLYMER-MATRIX COMPOSITES

2.1 DAMAGE MODELING IN FABRIC-BASED COMPOSITES

The failure in textile composites in general occurs in the vicinity of two perpendicular yarns crimping over and under to each other [3]. In the vicinity of the yarn crimping, the stress is known to be three dimensional. To optimize the material properties and improve the performance of textile composites, we need to understand the physics and identify the stress components influencing the failure mechanism. Experimental observation of damage initiation in textile composites reveals that the damage initiates in the form of interface cracks in the vicinity of yarn crimping, which is strongly influenced by the interlaminar stresses at the interface region. Most of the research work in this area, however, is based on two-dimensional stress analysis which does not reliably predict interlaminar stresses. Since finite-element analysis only predicts accurate stresses at the Gaussian integration points, even three-dimensional finite element analysis does not yield accurate interlaminar stresses at the interface. In order to obtain reliable interlaminar stresses at the interface, a three-dimensional analytical model is developed based on the Reissner variational principle [4]. Accurate prediction of interlaminar stresses at the yarn interface is obtained by satisfying the interface traction continuity conditions. The representative volume element (RVE) of the model is divided into several subregions; each subregion is occupied by a characteristic fabric yarn. The in-plane stresses within a yarn are assumed to vary linearly in the thickness direction. The expressions for the interlaminar stresses are obtained by satisfying the equilibrium equations. After performing the thickness integration, the model yields a set of partial differential and algebraic equations which are solved using cubic splines. The analytical derivation of the governing equations of the model is described below.

Reissner has shown that the governing equations of elasticity can be obtained from the following variational equation

$$\delta J = 0 \quad (2-1)$$

where

$$J = \int_V F dV - \int_{S'} \tilde{\tau}_i u_i dS \quad (2-2)$$

and

$$F = \frac{1}{2} \sigma_{ij} (u_{i,j} + u_{j,i}) - W \quad (2-3)$$

in terms of cartesian coordinates [x_i ($i=1,2,3$)]. In these equations W is the strain energy density expressed in terms of the stresses σ_{ij} ; V is the volume; S the entire surface; $\tilde{\tau}_i$ the prescribed tractions; u_i the displacement components; and S' is the portion of the boundary on which one or more traction components are prescribed. It is understood that both stresses and displacements are subjected to variation in the application of Equation (2-1), and summation over the range of repeated subscripts (but not superscripts) is implied throughout the work.

As described above, each yarn is modeled as homogeneous and transversely isotropic. The cross-sectional boundary of the yarn is confined by h_1 (lower boundary) and h_2 (upper boundary). Because of yarn waviness and the elliptical cross-sectional boundary of the yarns, h_1 and h_2 are functions of both x and y . Contracted notation is employed in the representation of the stress and strain components, i. e.,

$$\sigma_1 = \sigma_x, \sigma_2 = \sigma_y, \sigma_3 = \sigma_z, \sigma_4 = \sigma_{yz}, \sigma_5 = \sigma_{xz}, \sigma_6 = \sigma_{xy} \quad (2-4)$$

and analogous relation for the engineering strain components ε_i ($i=1-6$).

The equilibrium equations are satisfied by assuming the following form for the stress components.

$$\sigma_i = s_{iK} f_K^{(i)} \quad (i = 1-6, K = 1-4) \quad (2-5)$$

where s_{iK} are functions of x and y only, and

$$f_1^{(1)} = f_1^{(2)} = f_1^{(3)} = f_1^{(4)} = f_1^{(5)} = f_1^{(6)} = \frac{h_2 - z}{h_2 - h_1} \quad (2-6)$$

$$f_2^{(1)} = f_2^{(2)} = f_2^{(3)} = f_2^{(4)} = f_2^{(5)} = f_2^{(6)} = \frac{z - h_1}{h_2 - h_1} \quad (2-7)$$

$$f_3^{(3)} = f_3^{(4)} = f_3^{(5)} = \frac{z^2 - z(h_1 + h_2) + h_1 h_2}{(h_2 - h_1)^2} \quad (2-8)$$

$$f_4^{(3)} = \frac{z^3 - z(h_1^2 + h_1 h_2 + h_2^2) + h_1 h_2 (h_1 + h_2)}{(h_2 - h_1)^3} \quad (2-9)$$

with

$$\sigma_{iK} = f_K^{(i)} = 0 \quad (i = 1,2,6 \text{ and } K = 3,4; i = 4,5 \text{ and } K = 4) \quad (2-10)$$

The strain energy density of an elastic anisotropic body, including the influence of free expansion, is given by

$$W = \frac{1}{2} S_{ij} \sigma_i \sigma_j + \sigma_i e_i \quad (2-11)$$

The assumed form of the stresses is substituted in Equation (1), and the integration with respect to z is performed. The integration with respect to z also gives rise to weighted average displacements and the displacements on the surfaces $z = h_1, h_2$. The definitions of the weighted displacements are

$$[\bar{q}(x, y), q^*(x, y), \hat{q}(x, y)] = \int_{h_1}^{h_2} [H_1, H_2, H_3] q(x, y, z) dz \quad (2-12)$$

where

$$H_1 = \frac{h_2 - z}{(h_2 - h_1)^2}, \quad H_2 = \frac{z - h_1}{(h_2 - h_1)^2}, \quad H_3 = \frac{z^2 - zz(h_1 + h_2) + h_1 h_2}{(h_2 - h_1)^3}$$

Because of the dependence of h_1 and h_2 on x and y , Leibnitz's theorem in the following form must be applied on terms involving derivatives in x and y .

$$\int_{h_1(x, y)}^{h_2(x, y)} \frac{\partial}{\partial \xi} F(x, y, z) dz = \frac{d}{d\xi} \int_{h_1(x, y)}^{h_2(x, y)} F(x, y, z) dz - \frac{\partial h_2}{\partial \xi} F(x, y, h_2) + \frac{\partial h_1}{\partial \xi} F(x, y, h_1) \quad (2-13)$$

where ξ represents either x or y .

In addition, q may represent either u , v , or w . After substituting Equations (3)-(12) into (2), using Equation (13) where appropriate, and taking the first variation we obtain

$$\begin{aligned} \delta J = & \iint_{xy} \sum_{k=1}^N [(\mu_{ij} + \chi_{ij})^{(k)} \delta s_{ij}^{(k)} - (F_1 \delta \bar{u} + F_2 \delta^* + F_3 \delta \bar{v} + F_4 \delta^* + F_5 \delta \bar{w} + F_6 \delta^*)^{(k)}] dx dy \\ & + \iint_{xy} \sum_{k=1}^{N-1} \left[\left(s_{52}^{(k)} - \frac{\partial h_k}{\partial x} s_{12}^{(k)} - \frac{\partial h_k}{\partial y} s_{62}^{(k)} \right) \delta u_2^{(k)} + \left(\frac{\partial h_k}{\partial x} s_{11}^{(k+1)} - \frac{\partial h_k}{\partial y} s_{61}^{(k+1)} - s_{51}^{(k+1)} \right) \delta u_1^{(k+1)} \right. \\ & + \left(s_{42}^{(k)} - \frac{\partial h_k}{\partial x} s_{62}^{(k)} - \frac{\partial h_k}{\partial y} s_{22}^{(k)} \right) \delta v_2^{(k)} + \left(\frac{\partial h_k}{\partial x} s_{61}^{(k+1)} - \frac{\partial h_k}{\partial y} s_{21}^{(k+1)} - s_{41}^{(k+1)} \right) \delta v_1^{(k+1)} \\ & \left. + \left(s_{32}^{(k)} - \frac{\partial h_k}{\partial x} s_{52}^{(k)} - \frac{\partial h_k}{\partial y} s_{42}^{(k)} \right) \delta w_2^{(k)} + \left(\frac{\partial h_k}{\partial x} s_{51}^{(k+1)} - \frac{\partial h_k}{\partial y} s_{41}^{(k+1)} - s_{31}^{(k+1)} \right) \delta w_1^{(k+1)} \right] dx dy \end{aligned}$$

$$\begin{aligned}
& + \iint_{xy} \left[\left(s_{52}^{(N)} - \frac{\partial h_N}{\partial x} s_{12}^{(N)} - \frac{\partial h_N}{\partial y} s_{62}^{(N)} \right) \delta u_2^{(N)} + \left(\frac{\partial h_0}{\partial x} s_{11}^{(1)} + \frac{\partial h_0}{\partial y} s_{61}^{(1)} - s_{51}^{(1)} \right) \delta u_1^{(1)} \right. \\
& + \left(s_{42}^{(N)} - \frac{\partial h_N}{\partial x} s_{62}^{(N)} - \frac{\partial h_N}{\partial y} s_{22}^{(N)} \right) \delta v_2^{(N)} + \left(\frac{\partial h_0}{\partial x} s_{61}^{(1)} - \frac{\partial h_0}{\partial y} s_{21}^{(1)} - s_{41}^{(1)} \right) \delta v_1^{(1)} \\
& + \left. \left(s_{32}^{(N)} - \frac{\partial h_N}{\partial x} s_{52}^{(N)} - \frac{\partial h_N}{\partial y} s_{42}^{(N)} \right) \delta w_2^{(N)} + \left(\frac{\partial h_0}{\partial x} s_{51}^{(1)} - \frac{\partial h_0}{\partial y} s_{41}^{(1)} - s_{31}^{(1)} \right) \delta w_1^{(1)} \right] dx dy \\
& + \int_x \sum_{k=1}^N \left\{ \left[(s_{61} - \tilde{s}_{61})^{(k)} \delta u^{(k)} + (s_{62} - \tilde{s}_{62})^{(k)} \delta u^{*(k)} + (s_{21} - \tilde{s}_{21})^{(k)} \delta v^{(k)} + (s_{22} - \tilde{s}_{22})^{(k)} \delta v^{*(k)} \right. \right. \\
& \left. \left. + (s_{41} - \tilde{s}_{41})^{(k)} \delta w^{(k)} + (s_{42} - \tilde{s}_{42})^{(k)} \delta w^{*(k)} + (s_{43} - \tilde{s}_{43})^{(k)} \delta \hat{w}^{(k)} \right] (z_k - z_{k-1}) \right\}_{y_1}^{y_2} dx \\
& + \int_y \sum_{k=1}^N \left\{ \left[(s_{11} - \tilde{s}_{11})^{(k)} \delta u^{(k)} + (s_{12} - \tilde{s}_{12})^{(k)} \delta u^{*(k)} + (s_{61} - \tilde{s}_{61})^{(k)} \delta v^{(k)} + (s_{62} - \tilde{s}_{62})^{(k)} \delta v^{*(k)} \right. \right. \\
& \left. \left. + (s_{51} - \tilde{s}_{51})^{(k)} \delta w^{(k)} + (s_{52} - \tilde{s}_{52})^{(k)} \delta w^{*(k)} + (s_{53} - \tilde{s}_{53})^{(k)} \delta \hat{w}^{(k)} \right] (z_k - z_{k-1}) \right\}_{x_1}^{x_2} dy \\
& - \iint_{xy} \left[(\tilde{\tau}_{x2} \delta u_2^{(N)} + \tilde{\tau}_{y2} \delta v_2^{(N)} + \tilde{\tau}_{z2} \delta w_2^{(N)}) \sec \alpha_N \sec \beta_N \right. \\
& \left. - (\tilde{\tau}_{x1} \delta u_1^{(1)} + \tilde{\tau}_{y1} \delta v_1^{(1)} + \tilde{\tau}_{z1} \delta w_1^{(1)}) \sec \alpha_1 \sec \beta \right] dx dy = 0
\end{aligned} \tag{2-14}$$

where μ_{ij} and χ_{ij} are defined in the Appendix.

All terms in Equation (2-14) are not independent. However, there are 23^*N unknown variables (here N is the number of subregions) to be determined. After imposing the interface traction continuity conditions, we obtain the following governing equations representing the equilibrium, compatibility, and boundary conditions for the RVE.

2.1.1 Equilibrium Equations

$$F_i^{(k)} = 0, i = 1, 2, \dots, 7 \quad \text{for } k = 1, 2, \dots, N \tag{2-15}$$

2.1.2 Compatibility Equations

$$\chi_{33}^{(k)} = \chi_{34}^{(k)} = \chi_{43}^{(k)} = \chi_{53}^{(k)} = 0 \quad \text{for } k = 1, 2, \dots, N \quad (2-16)$$

where

$$\chi_{ij}^{(k)} = \eta_{ij}^{(k)} - E_{ij}^{(k)} - \hat{S}_{iklj}^{(k)} s_{kl}^{(k)} \quad (2-17)$$

2.1.3 Interface Compatibility Equations

Consider a perfectly bonded interface between k-th and l-th yarns. Here k-th yarn is considered on top of the l-th yarn (i.e., k-th yarn is at a higher z-value than that of the l-th yarn).

$$\chi_{i1}^{(k)} + \chi_{i2}^{(l)} = 0 \quad \text{for } i = 1, 2, \dots, 6 \quad (2-18)$$

$$\chi_{12}^{(l)} + \frac{\partial h_l}{\partial x} \chi_{52}^l + \left(\frac{\partial h_l}{\partial x} \right)^2 \chi_{32}^l = 0 \quad (2-19)$$

$$\chi_{22}^{(l)} + \frac{\partial h_l}{\partial y} \chi_{42}^l + \left(\frac{\partial h_l}{\partial y} \right)^2 \chi_{32}^l = 0 \quad (2-20)$$

$$\chi_{31}^{(1)} - \tilde{w}_1^{(1)} = 0 \quad (2-21)$$

$$s_{52}^{(l)} - \frac{\partial h_l}{\partial x} s_{12}^{(l)} - \frac{\partial h_l}{\partial y} s_{62}^{(l)} - s_{51}^{(k)} + \frac{\partial h_l}{\partial x} s_{11}^{(k)} + \frac{\partial h_l}{\partial y} s_{61}^{(k)} = 0 \quad (2-22)$$

$$s_{42}^{(l)} - \frac{\partial h_l}{\partial x} s_{62}^{(l)} - \frac{\partial h_l}{\partial y} s_{22}^{(l)} - s_{41}^{(k)} + \frac{\partial h_l}{\partial x} s_{61}^{(k)} + \frac{\partial h_l}{\partial y} s_{21}^{(k)} = 0 \quad (2-23)$$

$$s_{32}^{(l)} - \frac{\partial h_l}{\partial x} s_{52}^{(l)} - \frac{\partial h_l}{\partial y} s_{42}^{(l)} - s_{31}^{(k)} + \frac{\partial h_l}{\partial x} s_{51}^{(k)} + \frac{\partial h_l}{\partial y} s_{41}^{(k)} = 0 \quad (2-24)$$

2.1.4 Boundary Conditions

Top surface

$$\chi_{12}^{(N)} + \frac{\partial h_N}{\partial x} \chi_{52}^{(N)} + \left(\frac{\partial h_N}{\partial x} \right)^2 \chi_{32}^{(N)} = 0 \quad (2-25)$$

$$\chi_{22}^{(N)} + \frac{\partial h_N}{\partial y} \chi_{42}^{(N)} + \left(\frac{\partial h_N}{\partial y} \right)^2 \chi_{32}^{(N)} = 0 \quad (2-26)$$

$$\chi_{62}^{(N)} + \frac{\partial h_N}{\partial x} \chi_{42}^{(N)} + \frac{\partial h_N}{\partial y} \chi_{52}^{(N)} + 2 \frac{\partial h_N}{\partial x} \frac{\partial h_N}{\partial y} \chi_{32}^{(N)} = 0 \quad (2-27)$$

$$\cos \alpha_0 \cos \beta_0 s_{32}^{(1)} - \sin \alpha_0 \cos \beta_0 s_{52}^{(1)} - \cos \alpha_0 \sin \beta_0 s_{42}^{(1)} = \tilde{\tau}_{z1}^{(1)} \quad (2-28)$$

$$\chi_{52}^{(N)} + \frac{\partial h_N}{\partial x} \chi_{32}^{(N)} + \tilde{u}_2^{(N)} = 0 \quad (2-29)$$

or

$$\cos \alpha_N \cos \beta_N s_{52}^{(N)} - \sin \alpha_N \cos \beta_N s_{12}^{(N)} - \cos \alpha_N \sin \beta_N s_{62}^{(N)} = \tilde{\tau}_{x2}^{(N)} \quad (2-30)$$

$$\chi_{42}^{(N)} + \frac{\partial h_N}{\partial y} \chi_{32}^{(N)} + \tilde{v}_2^{(N)} = 0 \quad (2-31)$$

or

$$\cos \alpha_0 \cos \beta_0 s_{51}^{(1)} - \sin \alpha_0 \cos \beta_0 s_{11}^{(1)} - \cos \alpha_0 \sin \beta_0 s_{61}^{(1)} = \tilde{\tau}_{x1}^{(1)} \quad (2-32)$$

$$\chi_{32}^{(N)} + \tilde{w}_2^{(N)} = 0 \quad (2-33)$$

or

$$\cos \alpha_N \cos \beta_N s_{32}^{(N)} - \sin \alpha_N \cos \beta_N s_{52}^{(N)} - \cos \alpha_N \sin \beta_N s_{42}^{(N)} = \tilde{\tau}_{z2}^{(N)} \quad (2-34)$$

Bottom surface

$$\chi_{11}^{(1)} + \frac{\partial h_0}{\partial x} \chi_{51}^{(1)} + \left(\frac{\partial h_0}{\partial x} \right)^2 \chi_{31}^{(1)} = 0 \quad (2-35)$$

$$\chi_{21}^{(1)} + \frac{\partial h_0}{\partial y} \chi_{41}^{(1)} + \left(\frac{\partial h_0}{\partial y} \right)^2 \chi_{31}^{(1)} = 0 \quad (2-36)$$

$$\chi_{61}^{(1)} + \frac{\partial h_0}{\partial x} \chi_{41}^{(1)} + \frac{\partial h_0}{\partial y} \chi_{51}^{(1)} + 2 \frac{\partial h_0}{\partial x} \frac{\partial h_0}{\partial y} \chi_{31}^{(1)} = 0 \quad (2-37)$$

$$\chi_{51}^{(1)} + \frac{\partial h_0}{\partial x} \chi_{31}^{(1)} + \tilde{u}_1^{(1)} = 0 \quad (2-38)$$

or

$$\cos \alpha_0 \cos \beta_0 s_{51}^{(1)} - \sin \alpha_0 \cos \beta_0 s_{11}^{(1)} - \cos \alpha_0 \sin \beta_0 s_{61}^{(1)} = \tilde{\tau}_{x1}^{(1)} \quad (2-39)$$

$$\chi_{41}^{(1)} + \frac{\partial h_0}{\partial y} \chi_{31}^{(1)} + \tilde{v}_1^{(1)} = 0 \quad (2-40)$$

or

$$\cos \alpha_0 \cos \beta_0 s_{41}^{(1)} - \sin \alpha_0 \cos \beta_0 s_{61}^{(1)} - \cos \alpha_0 \sin \beta_0 s_{21}^{(1)} = \tilde{\tau}_{y1}^{(1)} \quad (2-41)$$

$$\chi_{31}^{(1)} + \tilde{w}_1^{(1)} = 0 \quad (2-42)$$

or

$$\cos \alpha_0 \cos \beta_0 s_{32}^{(1)} - \sin \alpha_0 \cos \beta_0 s_{52}^{(1)} - \cos \alpha_0 \sin \beta_0 s_{42}^{(1)} = \tilde{\tau}_{z1}^{(1)} \quad (2-43)$$

There are 23 unknown variables for each subregion (yarn) in the model. For an N number of subregions, Equations (15-43) yields a set of 23*N equations to determine the variables required to obtain the complete three-dimensional stress and strain fields. A numerical solution technique to solve the above system of equations, using cubic splines, is being formulated.

2.2 COMPOSITE ADHESIVE TESTING

2.2.1 Experimental Study of Damage in Bonded Composite Joints

The use of adhesively-bonded composite structures is expected to increase for two primary reasons. The first is the drive to reduce the assembly cost in composite structures by applying the concept of large, highly-integrated bonded and cocured structures. The second is the need to perform repairs on composite structures; these repairs often necessitate the use of bonded scarf joints. A primary concern regarding the use of adhesively-bonded joints in primary load-bearing structures is the environmental durability of the bond. This study attempts to identify failure modes seen in adhesively-bonded composite structures and environmental effects on bonded composite structures.

All the test data reported in this report, however, are for tests performed in room temperature and dry conditions (i.e., without aging the specimens in an environmental chamber). The specimen geometry selected was double-lap type to reduce the large amount of global bending observed in single-lap configurations. The adhesives included in the study were Cytex FM300-2U and FM300-2M, and the carbon/epoxy AS4/3501-6 composite was used as the adherent. In order to be consistent with the curing temperature of heat blanket field repair, the curing temperature of the adhesive was chosen to be 125°C (257°F).

2.2.1.1 Bonding Process Selection

A study for process selection was carried out to control and minimize the void content in the bond line. Unidirectional 16-ply (0.080 inch thick) AS4/3501-6 carbon/epoxy composite was used as the adherent. The adherents were prepared for bonding by hand sanding the bonding surface and then cleaning with acetone. Then, in order to minimize the ingress of moisture from the adherent (AS4/3501-6 composite) during curing of the adhesive bond, the adherent was vacuum dried overnight prior to bonding. The manufacturer's recommended cure cycle was first used to cure the bond which yielded a considerable amount (over the acceptable limit) of void content in the adhesive. In order to modify the cure cycle to minimize void content, parallel-plate rheometry of the adhesive was performed. Figure 28 shows the adhesive viscosity and temperature profiles using the manufacturer's recommended cure cycle. For the manufacturer's recommended cycle, as revealed in Figure 28, there was a sharp viscosity increase of the adhesive within a very short time (less than 10 min.). Such a short time duration of viscosity increase was not sufficient to suppress the void formation even by applying 100 psi of external pressure. In order to slow down the rate of viscosity increase, a modified two-step cure

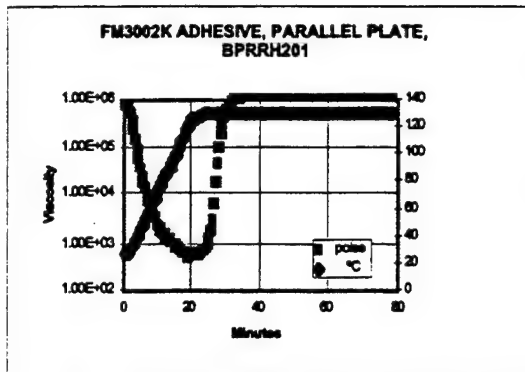


Figure 28. Parallel Plate Rheometry; Temperature and Viscosity Profiles of FM30-2K Adhesive Using the Manufacturer's Recommended Cure Cycle.

cycle was adopted. The viscosity and temperature profiles of the adhesive using the modified cure cycle are shown in Figure 29. The modified cure cycle contains a temperature hold at 100°C for 25 min. to slow down the viscosity rise of the adhesive; the rest of the curing was done at the 125°C hold. An external pressure of 100 psi was applied at the beginning of the 100°C temperature hold. The void content in the bond line using the modified cure cycle was less than two percent, quantified by optical microscopic inspection of polished edges of the bonded specimens. The modified cure cycle was thus selected and used to prepare all the double-lap shear specimens.

2.2.1.2 Test Procedure

Static tests were performed to monitor the initiation and growth of damage in unconditioned specimens. Very small strain gages (typically 0.032 and 0.015 inch in size), edge polishing coupled with optical microscopy, fluorescent microscopy, and acoustic

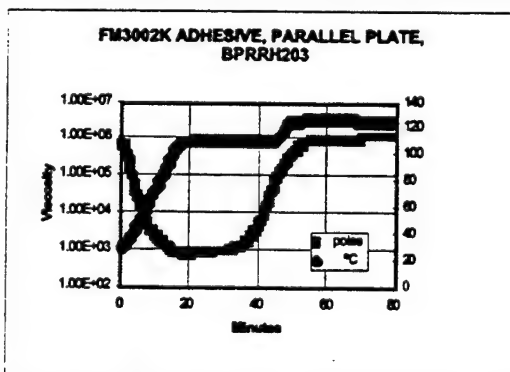


Figure 29. Parallel Plate Rheometry; Temperature and Viscosity Profiles of FM30-2K Adhesive Using the Modified Cure Cycle.

emission sensors were used to monitor damage progression. The specimen configuration of the double lap-shear specimens, and the representative locations where strain gages were installed to measure strains, are shown in Figure 30. The adherents were made of 16-ply [0] unidirectional AS4/3501-6 graphite/epoxy composites of 0.09-inch (2.286-mm) thickness. The average bond line thickness was 0.005 inch (0.127 mm). In order to validate the test procedure, the measured strains were correlated with analytical predictions before any damage initiation. The analytical prediction indicated a sign reversal of the interlaminar normal strain (e_3) between locations 4 and 5, and axial strain at location 7 being larger than that in location 6. The measured strains at these four locations due to tensile loading are shown in Figure 31. The measured strains at these four locations are qualitatively in agreement with the analytical prediction. Qualitative agreement of the measured strains with that of the analytical prediction ensured validity of the test procedure. In addition a quantitative correlation of the experimental data with the analytical prediction is being performed.

2.2.1.3 Damage Observation

One of the objectives of this study is to understand the damage development mechanism and develop methodology to predict failure. The specimens were loaded incrementally in tension; at the end of each load increment, the specimens were unloaded and the edge of the specimen containing the bond line was inspected with an optical microscope for damage. During loading the specimens were instrumented with an acoustic emission sensor for monitoring damage initiation. In addition strain gages at locations of strains sensitive to damage were also installed to monitor damage. Among many damage detection techniques, the fluorescent dye penetration technique appeared to be the most effective. Figure 32 shows the strain measured by Gage 5 (location of strain extremely sensitive to damage) in a specimen. As revealed from the strain plot in Figure 32, the second loading indicated initiation of damage. The specimen was then unloaded and its edge microscopically inspected for damage. The edge micrograph indicating crack initiation is shown in Figure 33. The crack initiated at the middle adherent interface crack, and at the bond end where Gage 5 was installed (location of high interlaminar normal and shear strains). Crack initiation took place at a stress level of 67 percent of that at final failure.

Besides crack initiation, tests were conducted to understand the crack propagation phenomenon. The specimens were loaded incrementally in tension beyond crack initiation following the same procedure as was followed in the case of the crack initiation study. The interlaminar normal strain measured by Gage 4, installed (at a damage sensitive location) on a specimen used for the damage propagation study, is shown in Figure 34. At the peak load of

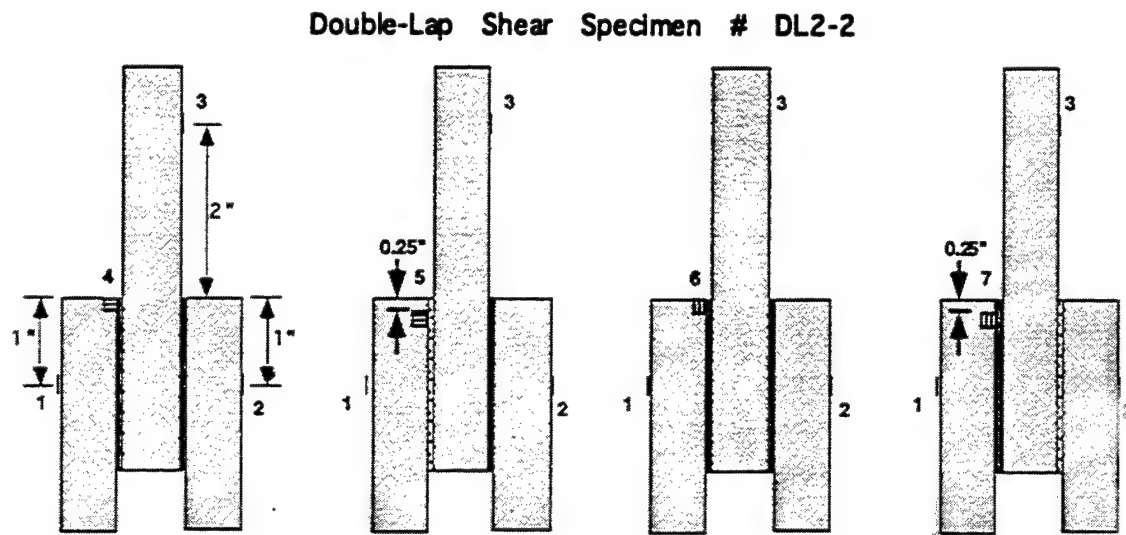


Figure 30. Specimen Configuration and Representative Strain Gage Locations of the Double Lap-Shear Specimen.

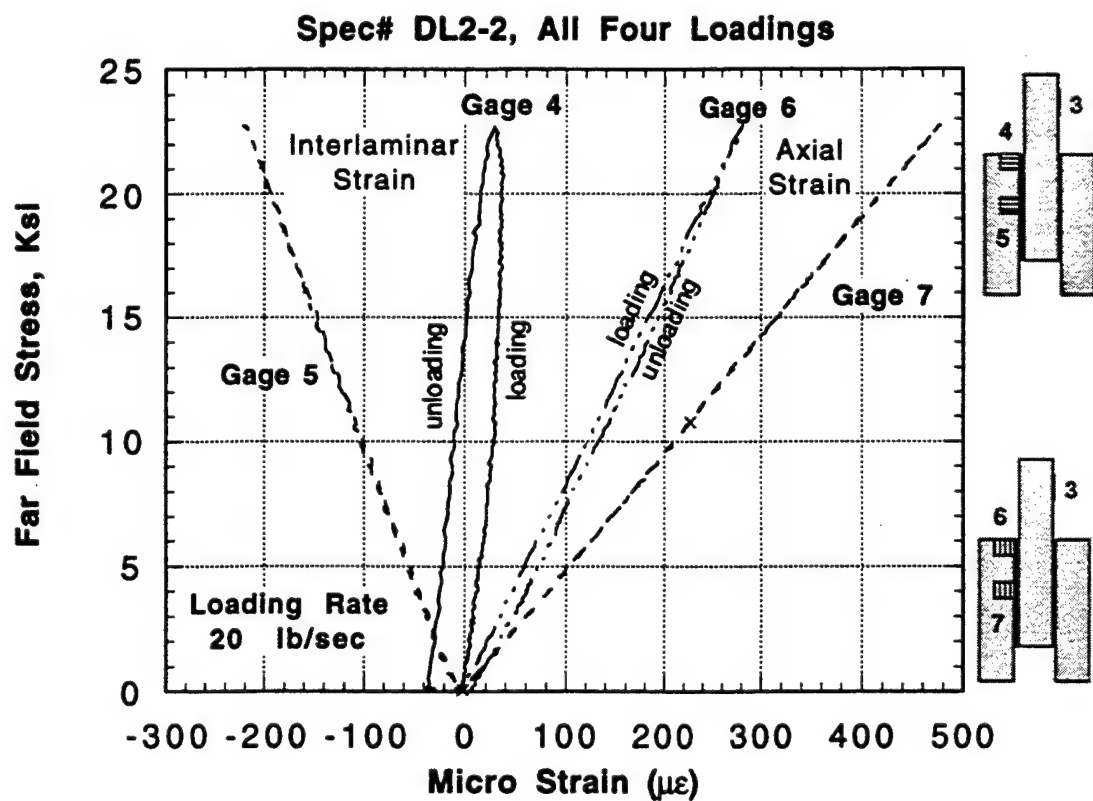


Figure 31. Measured Strains at Locations 4, 5, 6, and 7.

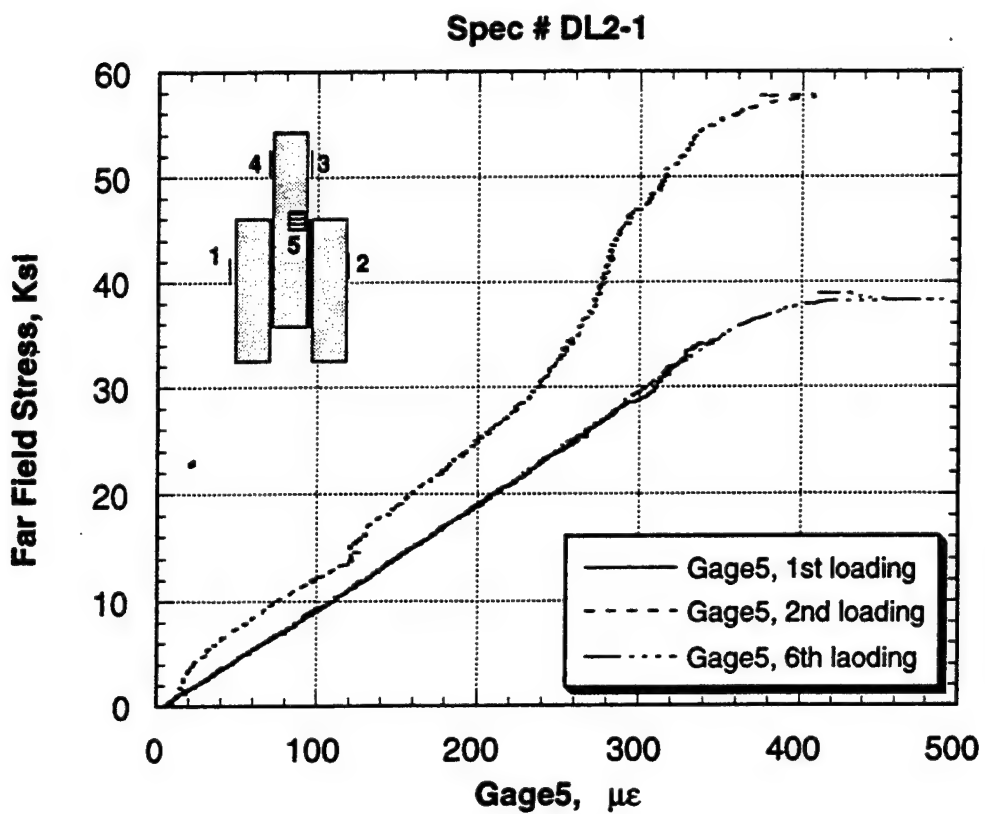


Figure 32. Interlaminar Normal Strains at a Damage-Sensitive Location for Several Incremental Loadings.

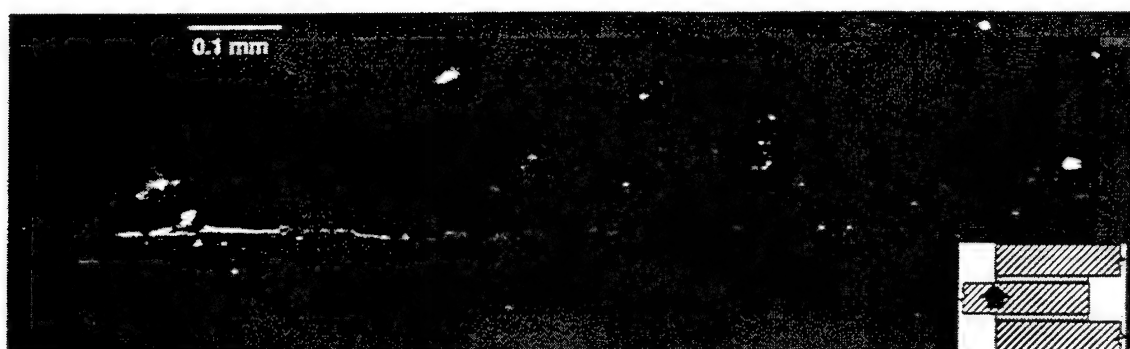


Figure 33. Micrograph (in Fluorescent Field) Indicating Crack Initiation at the Middle Adherent Interface.

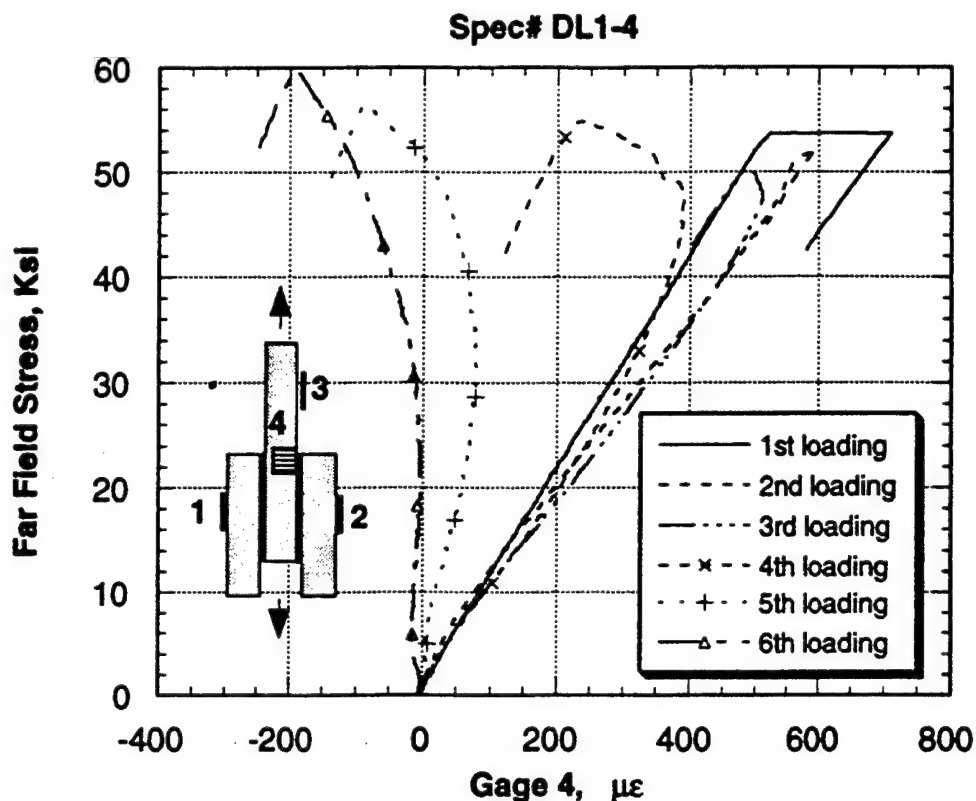


Figure 34. Interlaminar Normal Strains at a Damage-Sensitive Location for Several Incremental Loadings Beyond Crack Initiation in the Bond.

the first loading, the strain gage, accompanied by the acoustic emission sensor, indicated damage development. The edge micrograph of the specimen (Figure 35) showed a crack developed at the middle adherent interface. Observation of the crack along the bond line revealed that the crack moved from the middle adherent interface to the outer adherent interface at a distance of 19 mm from the crack initiation end of the bond (Figure 36). The micrographs shown in Figures 35 and 36 were taken at a loading of 90 percent of the failure load. The crack moving from one interface to the other was consistently observed in all specimens. The crack propagation phenomenon, from initiation to failure, is summarized in Figure 37. Observation of crack initiation and its propagation, that was made in this study, will be used for stress analysis of damage development in bonded joints.

2.2.2 Processing of FM300 Adhesive

A processing study was conducted on FM300 adhesive to reduce the porosity during fabrication of lap-shear specimens. The manufacturer recommended cure cycle stated that pressure should be applied prior to heating; however, this results in excess resin flow because of the low melt viscosity. Viscosity data generated from a parallel plate test (Figure 38)

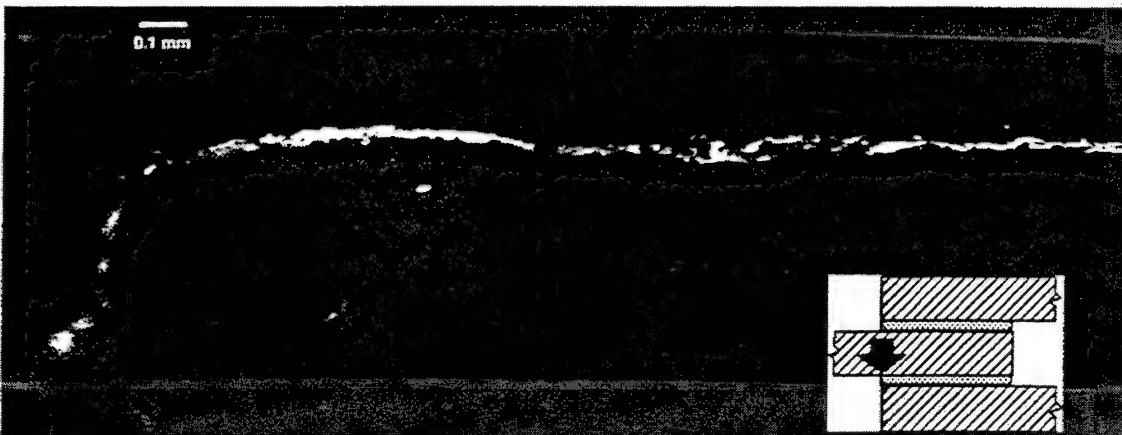


Figure 35. Edge Micrograph Showing Interface Crack at the Middle Adherent Interface taken After a Load of 90 Percent of Failure.

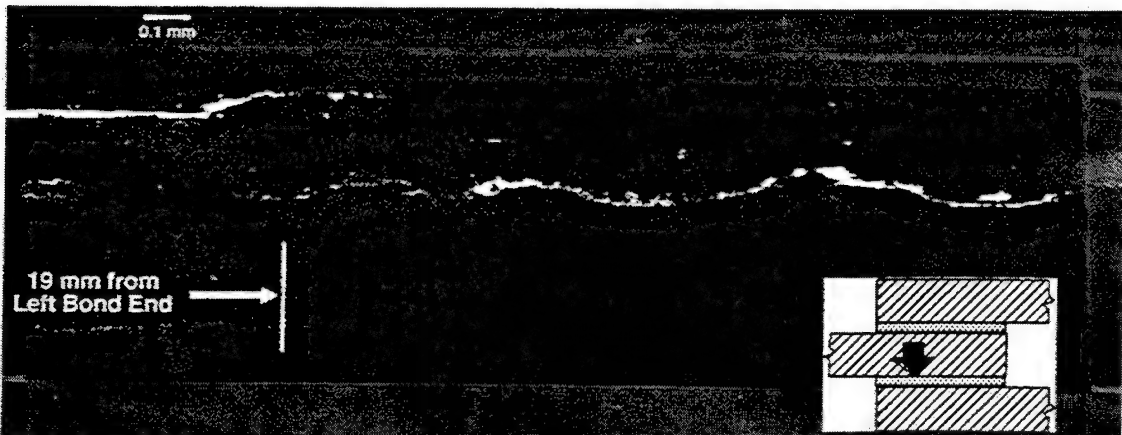


Figure 36. Edge Micrograph Showing Interface Crack Moving from One Adherent Interface to the Other. The micrograph was taken after a load of 90 percent of failure.

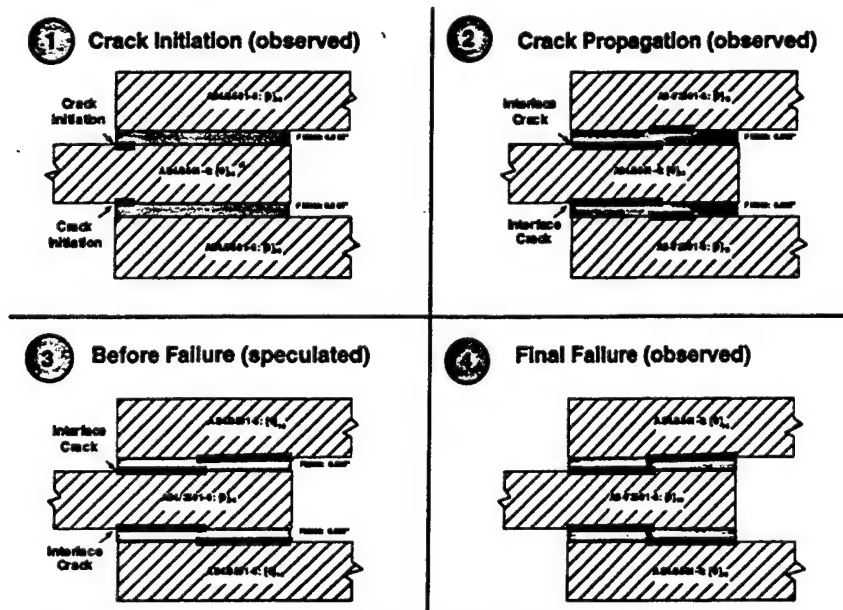


Figure 37. Representative Sequential Crack Propagation Event.

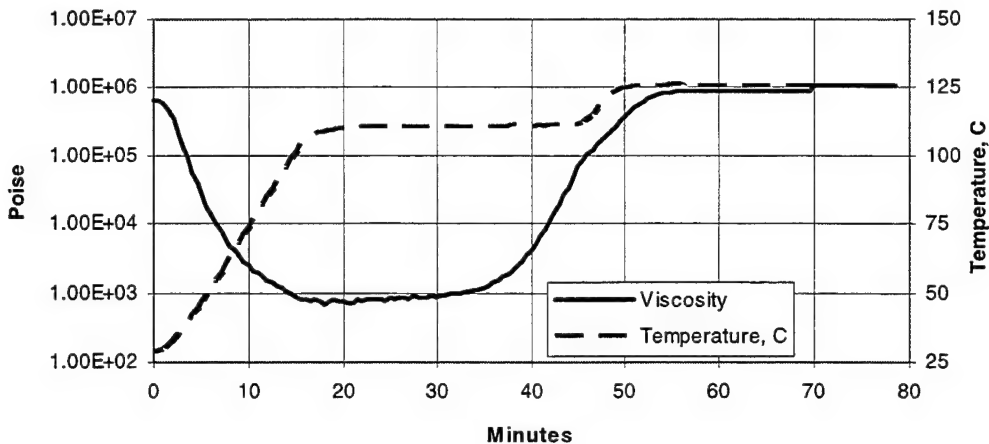


Figure 38. Parallel Plate Experiment of FM300 Adhesive.

indicates that a 20 to 30 minute hold at 110°C prior to pressure application will prevent excess resin flow.

2.3 DAMAGE PROCESS FOR COMPOSITE LAMINATES WITH CENTER HOLES

An experimental program was initiated on damage initiation and its progression in composite laminates with open and filled holes. The main objective of this program is to validate the spline variational elastic laminate theory (SVELT) and to assess the damage evolution for development of a suitable failure prediction theory. The evaluation of the current design allowables for composite bolted joints will also be performed. The material system chosen was graphite-toughened epoxy, IM7/5250-4. Laminates considered at present are: $[0]_{8T}$, $[90]_{8T}$, $[\pm 45]_{2S}$, $[0/90]_{2S}$, $[\pm 30/90]_S$ for open-hole tension and $[0/90]_{4S}$ and $[\pm 30/90]_{2S}$ for filled-hole compression. For design allowables a variety of laminates will be considered. Composite panels were fabricated in an autoclave according to the manufacturer's cure cycle and subjected to postcure at 440°F for four hours. All cured panels are examined by ultrasonic C-scan to insure the quality of the panel. The fiber volume was determined using the acid digestion method. Straight-sided specimens were cut from the panels using a diamond-impregnated saw with water cooling. Specimen width and hole size are given in Table 6. A milling machine was used to drill 0.25-inch holes. The drill speed and pressure were previously established to produce a damage-free hole. Holes with a diameter of 0.5 inch were drilled using a Cavitron machine on unidirectional laminate specimens. X-ray radiographs indicate that the Cavitron method appears to produce better results for 0.5-inch holes. Hole edge regions are inspected prior to test by x-ray radiography to examine any damage induced by drilling.

TABLE 6
SUMMARY OF CENTER HOLE COMPOSITE TEST MATRIX

Test Type	Laminate	Width (in)	Hole Diameter (in)	Replication	Loading	No. of Strain Gages
OHT	[0]8T	3	0.5	3	INC	5
OHT	[90]8T	3	0.5	3	INC	5
OHT	[±45]2S	3	0.5	3	INC	5
OHT	[0 ₂ /90 ₂]S	3	0.5	3	INC	5
OHT	[±30/90 ₂]S	3	0.5	3	INC	5
FHT	[0 ₂ /90 ₂]S	1.25	0.25	2	INC	6
FHT	[0 ₂ /90 ₂]S	1.25	0.25	2	INC	6
FHT	[±30/90 ₂]S	1.25	0.25	2	MON	6
FHT	[±30/90 ₂]S	1.25	0.25	2	MON	6
OHC	[0 ₂ /90 ₂]S	1.5	0.25	2	INC	3
OHC	[0 ₂ /90 ₂]S	1.5	0.25	2	INC	3
OHC	[±30/90 ₂]S	1.5	0.25	2	MON	3
OHC	[±30/90 ₂]S	1.5	0.25	2	MON	3

OHT: Open-hole tension

INC: Incremental loading

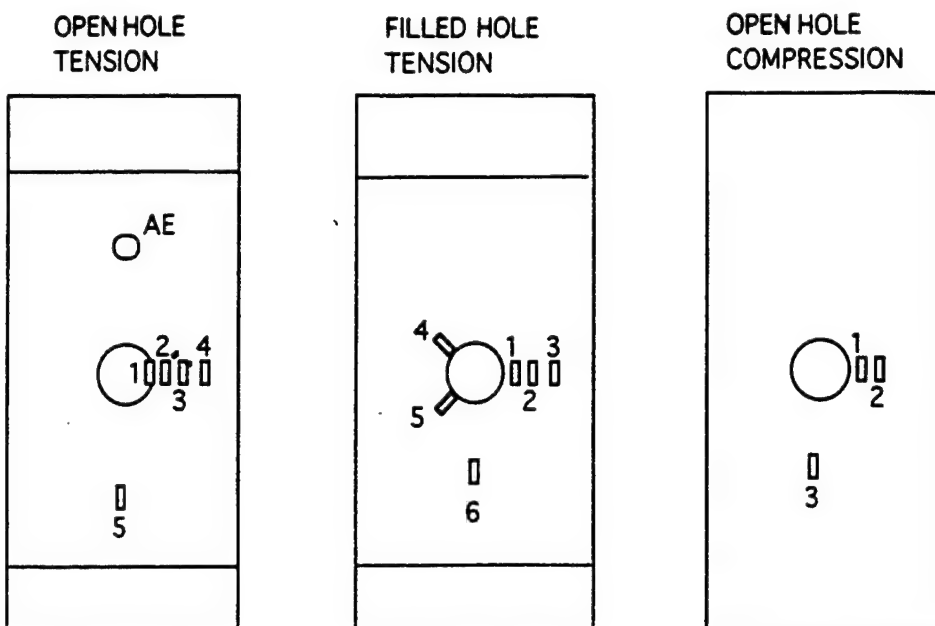
FHT: Filled-hole tension

MON: Monotonic loading

OHC: Open-hole compression

Specimens were tested under incremental loading for damage evolution study, and others were tested under monotonic loading up to failure for design allowables. For verification purposes the local strains on or near the vicinity of the hole edge, as indicated in Figure 39, are measured using miniature strain gages 0.008 inch in gage length. The initiation and progression of damage in the vicinity of the hole was observed using x-ray radiography after incremental loading. Acoustic emission was also incorporated to determine the onset of matrix cracking. The location, magnitude, and load corresponding to the occurrence of transverse cracks, longitudinal cracks, and delamination were recorded. For filled-hole compression, titanium fasteners were used, and the Boeing compression fixture was used to prevent premature buckling failure.

During the current reporting period, a total of 31 specimens were involved (Table 6). Some preliminary results on open-hole tension are presented in this report. The experimentally-measured strains for three locations from the hole edge were compared with analytical



1: on the edge
 2: 0.05" from the edge
 3: 0.15" from the edge
 4: 0.35" from the edge
 5: far field

1: 0.04" from the edge
 2: 0.15" from the edge
 3: 0.35" from the edge
 4: 45° from horizontal
 5: -45° from horizontal
 6: far field

1: 0.04" from the edge
 2: 0.15" from the edge
 3: far field

Figure 39. Specimen Showing Strain Gage Locations.

calculations [5] in Figures 40-44. The symbols and solid lines represent experiment and calculations, respectively. Since the measured strain with a miniature strain gage closely represents the strain at the center of the strain gage location for nonuniform state of strain distribution, the center of the strain gage location is taken as the abscissa of the data point. Stress-strain curves are presented for all gage locations in Figures 45-49. The stress-strain relation is initially linear and becomes nonlinear as the applied stress increases for all cases except [0]_{8T} and [90]_{8T} laminates. The proportional limit varies as a function of the distance from the hole edge. Figures 50-55 show damages obtained by x-ray radiographs. Longitudinal cracks in the [0]_{8T} laminates emanated at the hole edge and propagated along the fiber at subsequent incremental loadings. The SVELT analysis indicates that the shear stress appears to be responsible for the longitudinal crack. The [90]_{8T} specimens failed without exhibiting any damage prior to final failure and show net tension failure along the ligament between the hole and straight free edge. For the [±45]_S laminate, cracks occurred at the hole edge and propagated along the fiber direction (45°) (as shown in Figure 51) and reached the free edge before final failure. Limited delamination occurred between the ±45° cracks at higher loads.

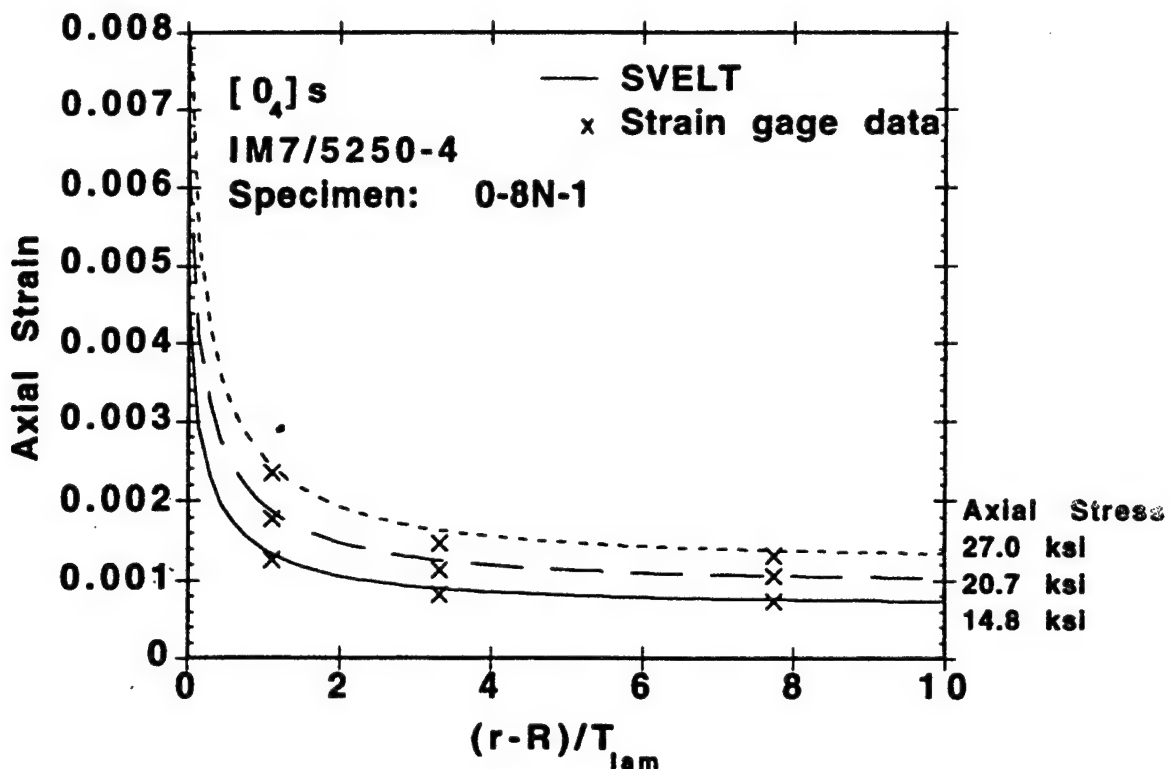


Figure 40. Comparison of Analytical and Experimental Strains at Hole Vicinity for $[0]_{8T}$ Laminate.

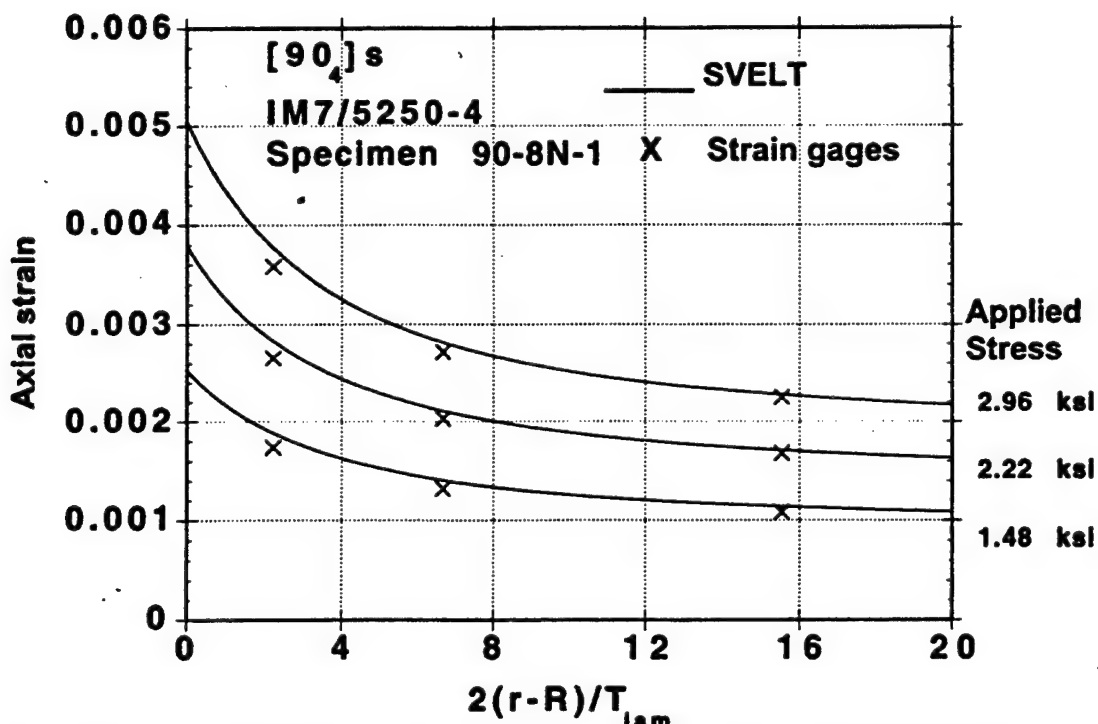


Figure 41. Comparison of Analytical and Experimental Strains at Hole Vicinity for $[90]_{8T}$ Laminate.

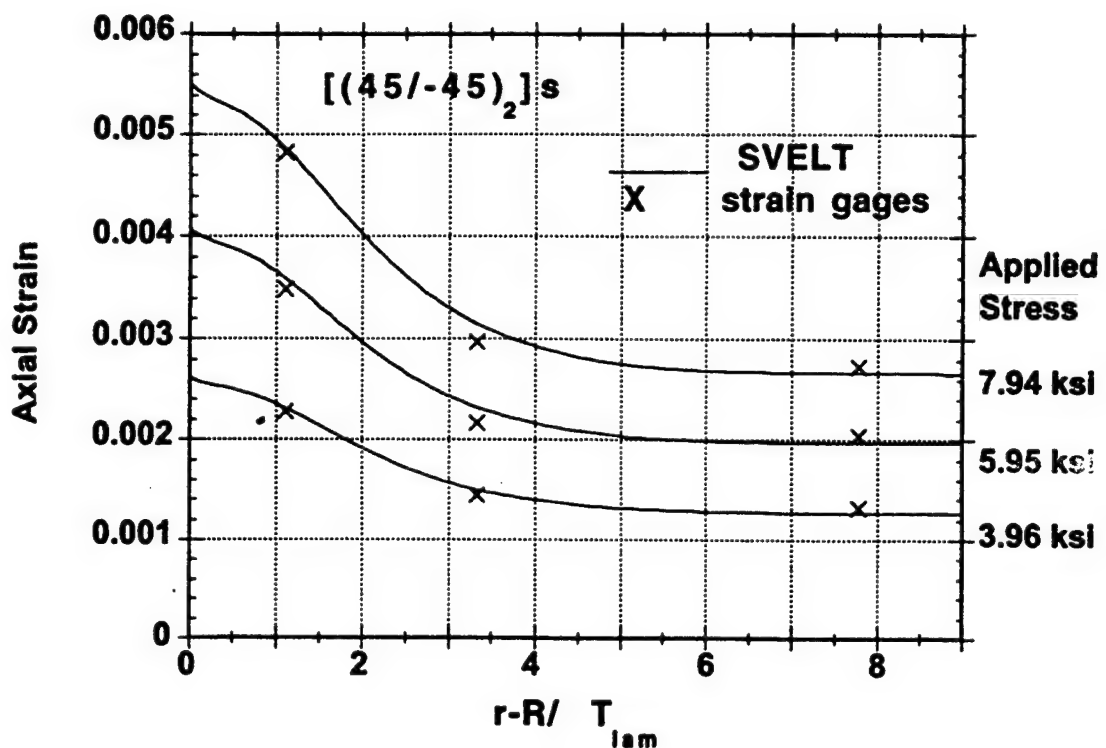


Figure 42. Comparison of Analytical and Experimental Strains at Hole Vicinity for $[\pm 45]_{2S}$ Laminate.

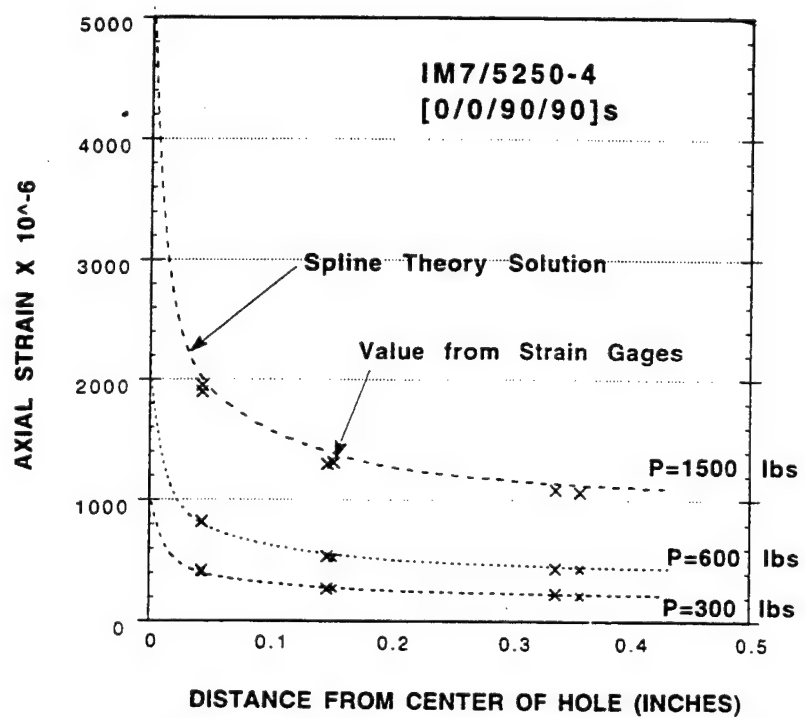


Figure 43. Comparison of Analytical and Experimental Strains at Hole Vicinity for $[0/90]_2s$ Laminate.

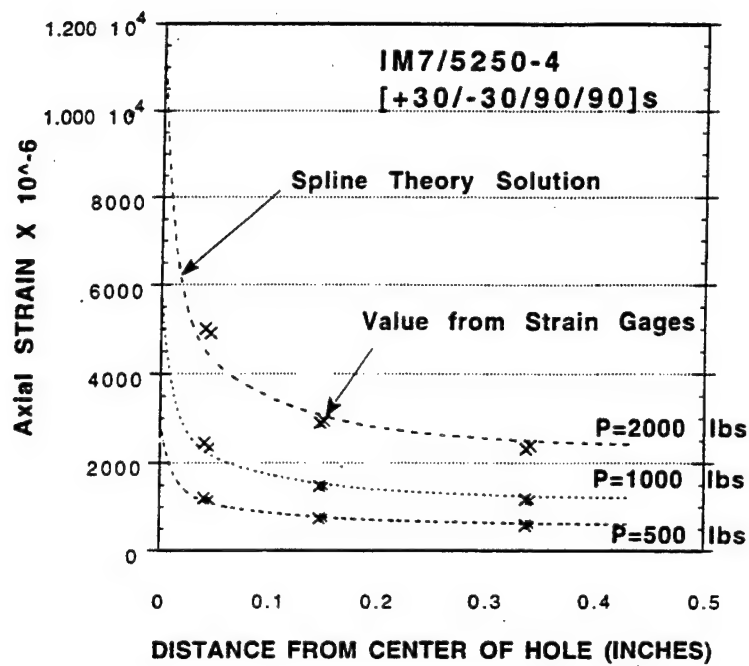


Figure 44. Comparison of Analytical and Experimental Strains at Hole Vicinity for $[\pm 30/90_2]_S$ Laminate.

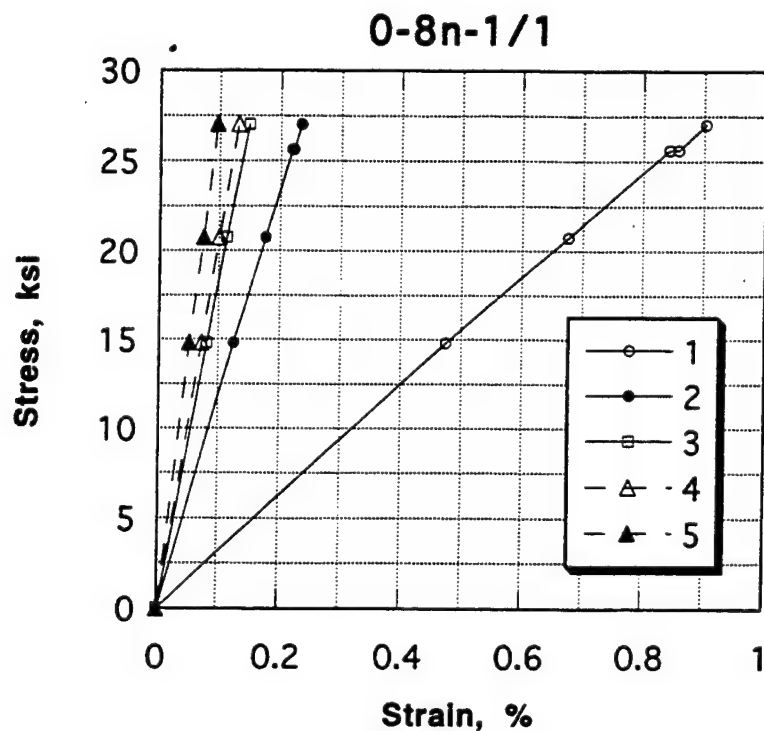


Figure 45. Experimental Stress-Strain Relation for $[0]_{8T}$.

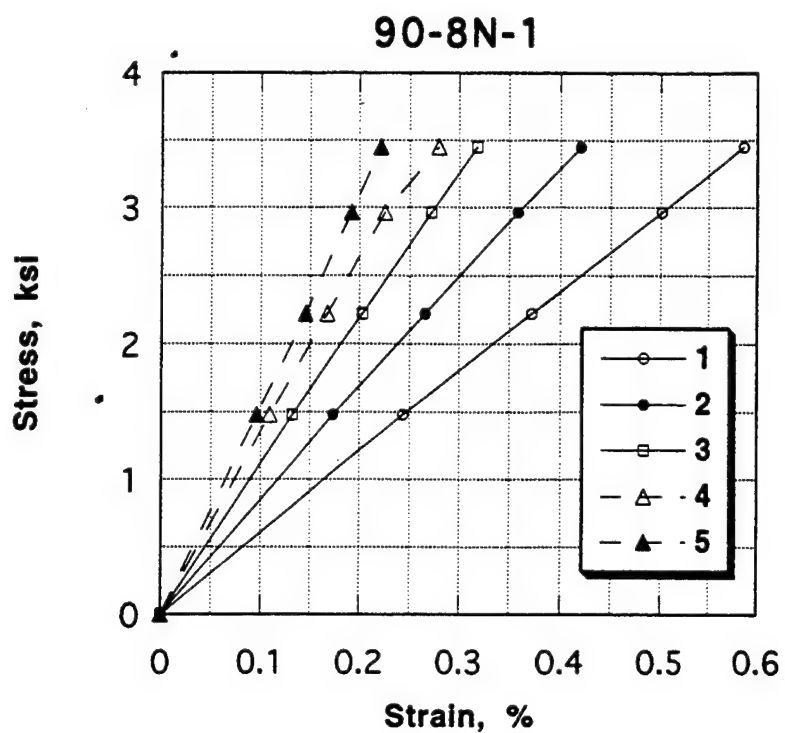


Figure 46. Experimental Stress-Strain Relation for [90]_{8T}.

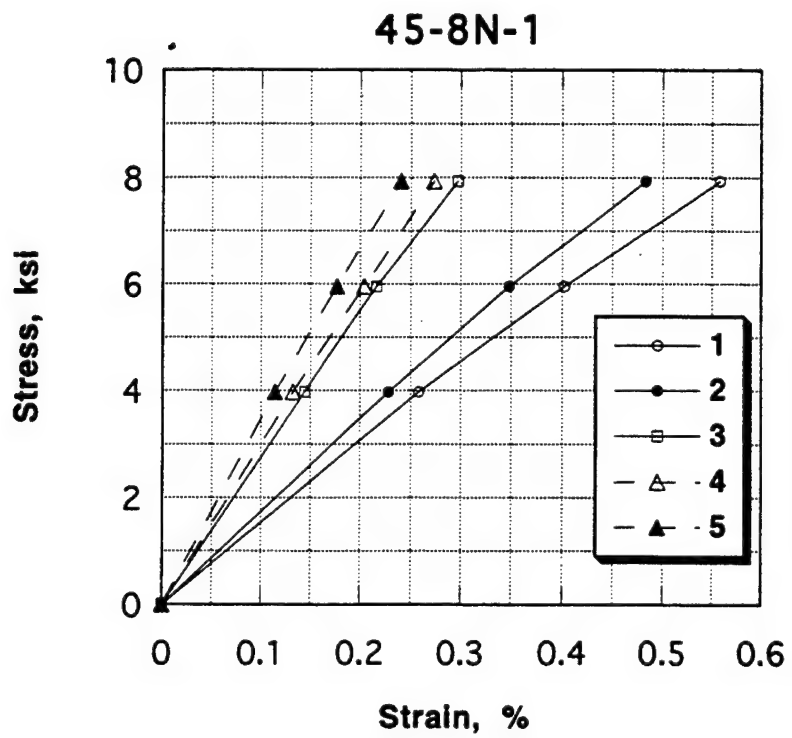


Figure 47. Experimental Stress-Strain Relation for [±45]_{2S}.

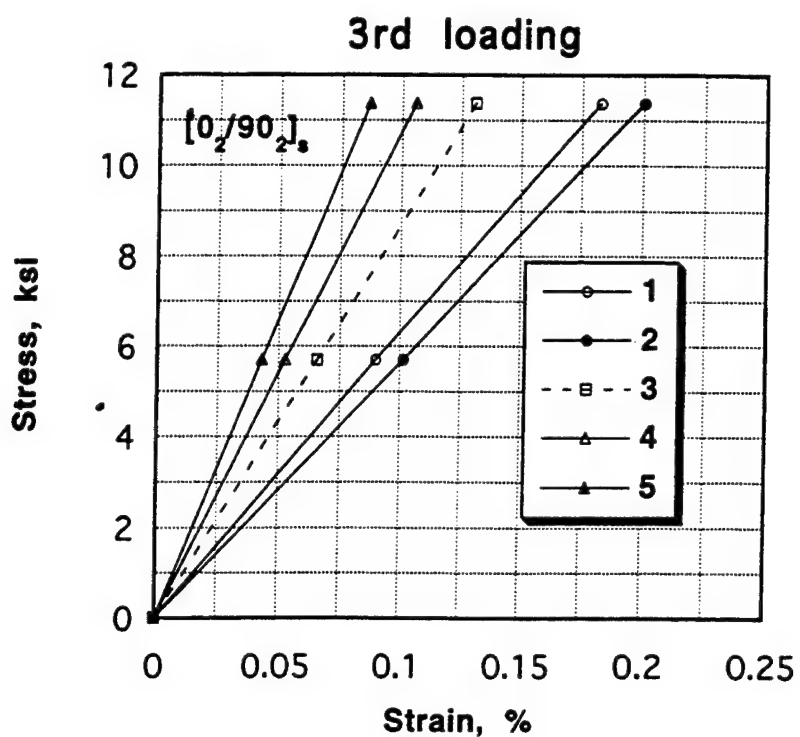


Figure 48. Experimental Stress-Strain Relation for $[0/90]_s$.

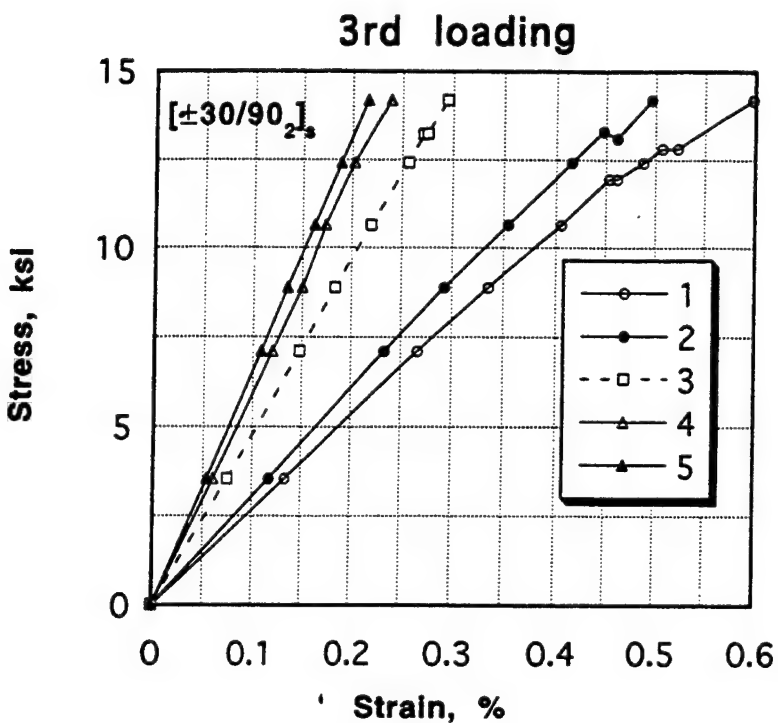


Figure 49. Experimental Stress-Strain Relation for $[\pm 30/90]_s$.

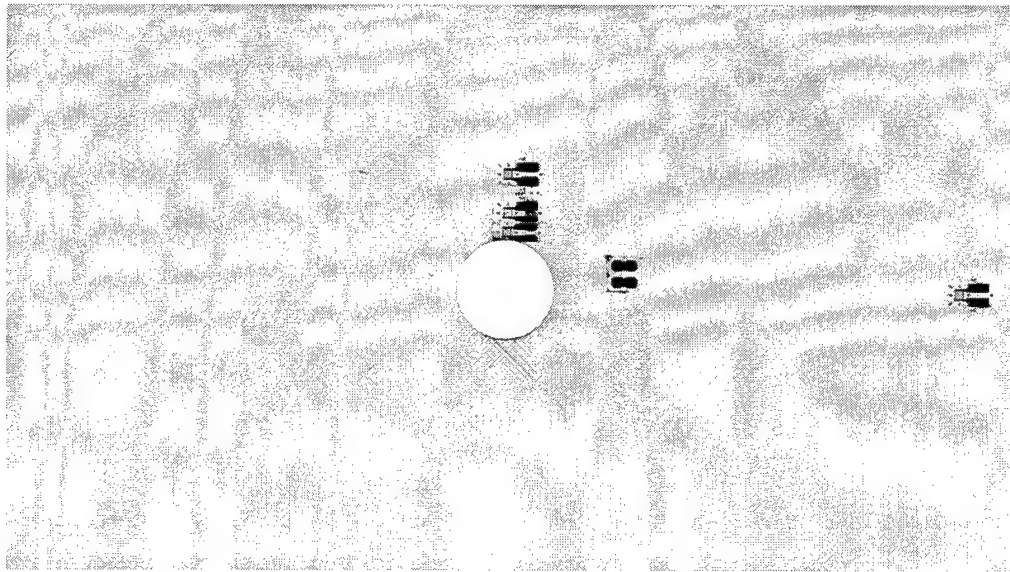


Figure 50. Radiograph Showing Damage Around the Hole in a $[0]_{8T}$ Specimen at an Applied Stress of 39.25 ksi.

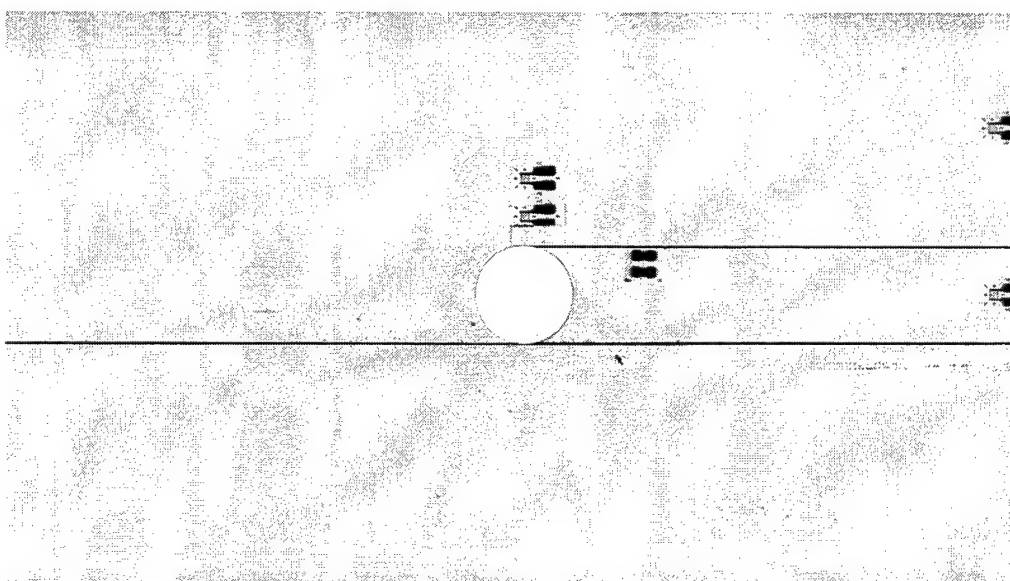


Figure 51. Radiograph Showing Damage Around the Hole in a $[\pm 45]_{2S}$ Specimen at an Applied Stress of 21.83 ksi.

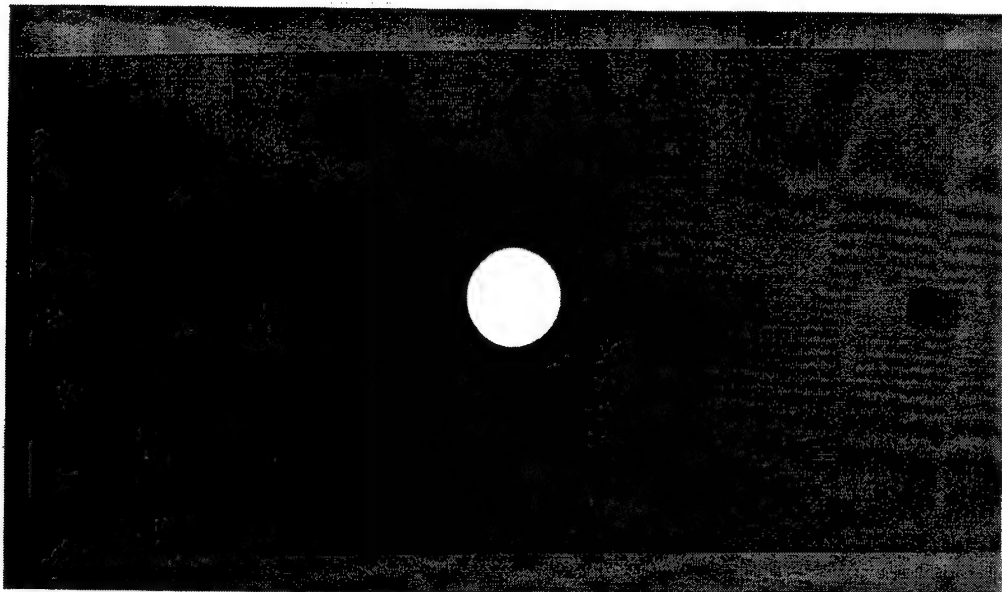


Figure 52. Radiograph Showing Damage Around the Hole in a $[0/90]_{2s}$ Specimen at an Applied Stress of 24.67 ksi.

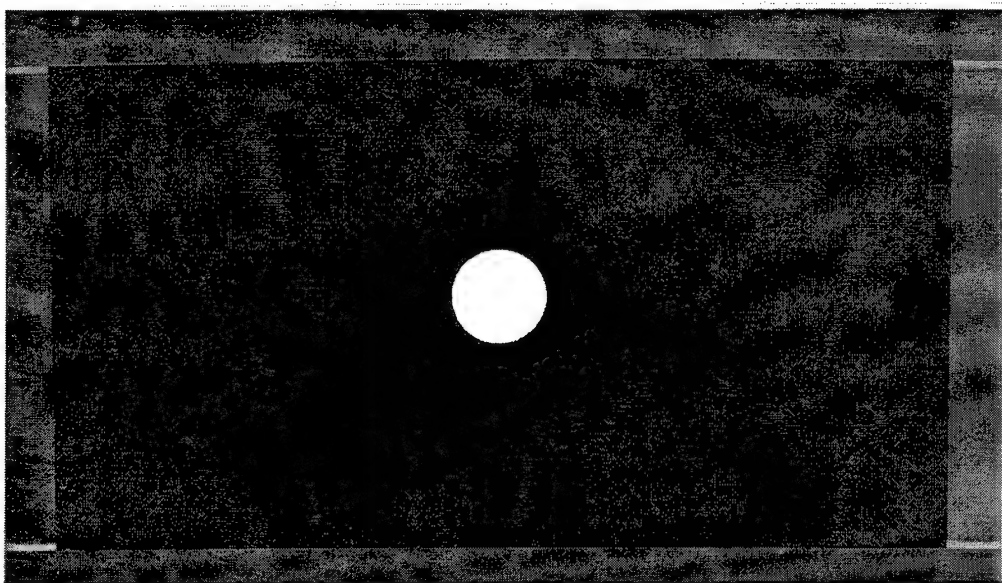


Figure 53. Radiograph Showing Damage Around the Hole in a $[\pm 30/90]_{2s}$ Specimen at an Applied Stress of 20.4 ksi.

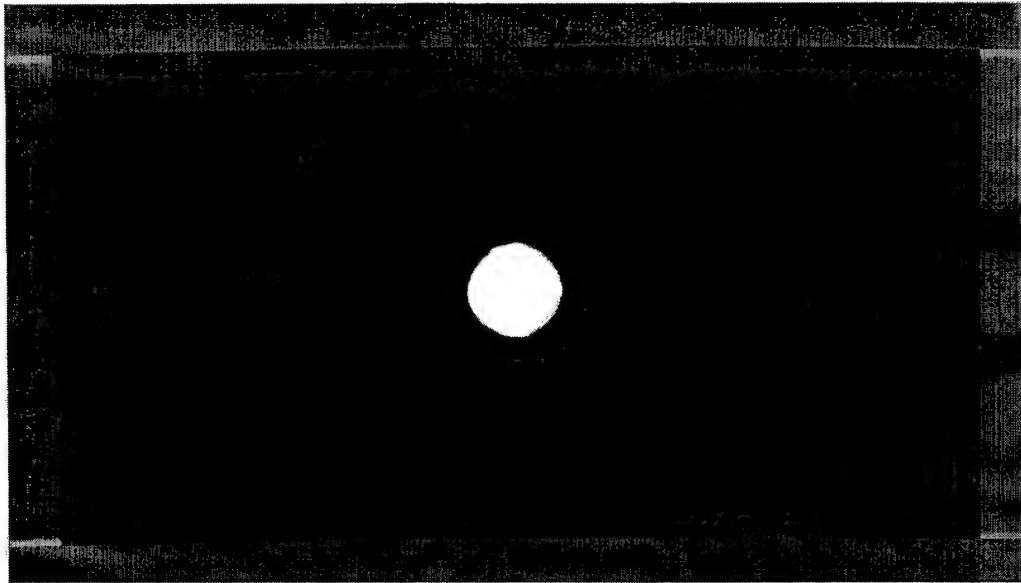


Figure 54. Radiograph Showing Damage Around the Hole in a $[0/90]_{2s}$ Specimen at an Applied Stress of 130.56 ksi.

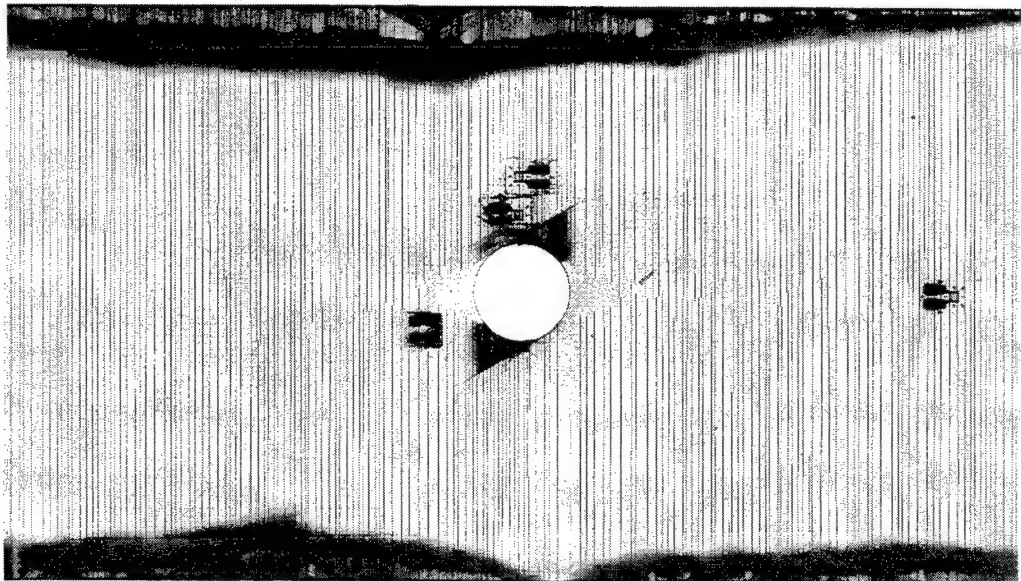


Figure 55. Radiograph Showing Damage Around the Hole in a $[\pm 30/90]_{2s}$ Specimen at an Applied Stress of 56.91 ksi.

In prediction of the onset of damage, the maximum stress theory is employed for the 3-D stress solution calculated by SVELT. The effective stress concept (average over a ply thickness from the hole edge) is employed in this work. This approach shows encouraging results when compared with the limited amount of experimental observation on the onset of transverse cracks for both the $[0/90]_{2s}$ laminate and $[\pm 30/90]_{2s}$ laminate. Extensive damage occurred in both laminates prior to final failure as shown in Figures 54 and 55. Longitudinal cracks for the $[0/90]_{2s}$ laminate and a 45° crack (along the fiber) for the $[\pm 30/90]_{2s}$ laminate occurred at higher stress levels. A considerable amount of delamination occurred on the straight free edges and the hole edge in the $[\pm 30/90]_{2s}$ laminate as shown in Figure 55. This work is continuing.

2.4 EXAMINATION OF SPACECRAFT-GRADE CYANATE ESTER COMPOSITES

2.4.1 CTE of Composite Laminates for Space Application

Many composite structures require not only high stiffness but precision alignment and dimensional stability as well, which makes the low coefficient of thermal expansion (CTE) of carbon fiber composites attractive. Strain gages provide an inexpensive yet accurate means of measuring the CTE of composite laminates, provided care is taken to avoid extraneous sources of error. These include apparent strains due to heating of the gage element and differential resistances of the gages, leads and lead wires, etc.

In this work the strain gage technique is refined to improve accuracy and reproducibility of the CTE measurement and is applied to the CTEs of a candidate material for space structures XN70/RS3, a high-modulus graphite fiber-reinforced cyanate ester and a general aerospace-grade graphite/epoxy AS4/3501.

2.4.1.1 Measurement Technique

Composite CTEs were measured using strain gage techniques in conjunction with a computer-controlled temperature chamber and data acquisition system. Ultralow expansion titanium silicate (with a maximum thermal strain of 10 ppm over the temperature range of interest) was used as the reference material. WK-series 350Ω strain gages (6.35-mm gage length) from Micro-Measurements, Inc. were employed for this study. Heat generation in the strain gage from the excitation current, which gives rise to an apparent strain, was minimized by reducing the input voltage to the strain gage circuit to one volt. Two strain gages, one on the reference specimen and one on the test specimen, were taken from the same

manufacturing lot to assure a close match of their apparent strain outputs. The strain gages were mounted with a high-temperature adhesive, cured as recommended by the manufacturer, and connected as adjacent arms of the bridge circuit. The output (apparent strain) of this half-bridge configuration is equal to the difference in the individual strains. This difference becomes zero when the two gages are electrically identical. Extremely stable precision resistors were used to complete the strain gage bridge. All lead wires were of equal length and maintained physically together throughout their length to minimize differential resistance changes. The reference and test specimens were placed near each other in a forced-air convection oven to minimize temperature differences. The temperatures of the specimen and oven were measured with separate thermocouples to check for thermal lag between them. Up to four strain gages were mounted on a composite specimen which, with complementary gages on the reference material, formed four strain gage bridges.

The measurement system can accommodate five channels; one was used for temperature and the remaining four for collecting thermal strains. A software program controlled the chamber temperature, allowing prescribed ramps to a series of temperatures, holds for a fixed period of time to allow the specimen temperature to equilibrate, and continuous acquisition of temperature and strain data. Data were collected during both heating and cooling cycles. A specimen was cycled between -101°C and 121°C at a heating rate of 3°C/min and held for 15 minutes at each temperature increment of 22°C. Thermal strains recorded at the end of each holding period were utilized for determination of CTE. The resolution of strain and temperature measurement with this experimental setup is 1×10^{-6} and 0.56°C, respectively. The correction for transverse sensitivity of the strain gage was made from the transverse sensitivity supplied by the manufacturer. Since the longitudinal thermal strain is two orders of magnitude smaller than the transverse thermal strain of a unidirectional composite, the transverse sensitivity correction is significant. Furthermore, the transverse sensitivity of the WK series gage employed is approximately four percent which is an order of magnitude greater than other types of gages. The gage factor correction was also performed according to the calibration curve supplied with the strain gages.

Although strain gages on the test specimen and reference specimen are from the same manufacturing lot, this does not guarantee that their electrical properties will be identical. To examine this effect, four strain gages were mounted on each of the titanium silicate and titanium specimens. Two gages were used as reference gages, while the other two were used as test gages with one reference gage and one test gage forming a half-bridge. If the titanium silicate and titanium are assumed to be homogeneous in thermal expansion, any output from this

arrangement is considered apparent strain due to the difference in electrical properties between the reference gage and test gage. Figure 56 shows the results of the measurements with this setup; the measured CTE from this exercise ranged from near zero to $1.66 \times 10^{-7}/^{\circ}\text{C}$.

The accuracy and reliability of this CTE measurement technique was verified with two materials of known CTE – aluminum Al-2024-T4 and Invar. Figures 57 and 58 show the thermal strains for the aluminum and Invar alloys, respectively. The symbols represent the experimental data. Curve fitting of the data (depicted by the solid lines) shows very little deviation of the thermal strains from linear behavior for aluminum, whereas the Invar is considerably nonlinear. The average CTE, obtained by dividing the total thermal strain by the temperature range, is $22.81 \times 10^{-6}/^{\circ}\text{C}$ for the aluminum alloy and $1.38 \times 10^{-6}/^{\circ}\text{C}$ for the Invar alloy. These values compare very well with the corresponding published handbook values of $23.22 \times 10^{-6}/^{\circ}\text{C}$ and $1.35 \times 10^{-6}/^{\circ}\text{C}$. The excellent reproducibility of the measurement technique was demonstrated by a variation of less than one percent in the CTE between consecutive measurements with all strain gages. Between runs the strain gage lead wires were detached and resoldered to simulate actual measurements.

2.4.1.2 CTE of Unidirectional Composites

Lamina longitudinal and transverse CTEs are fundamental thermal properties of a composite material and are used to calculate the thermal properties of various laminate orientations. To measure these CTEs a rectangular coupon 25 mm wide x 100 mm long was sectioned from a $[0]_{8T}$ composite panel. Two longitudinal and two transverse strain gages were mounted with a high-temperature adhesive which was cured for four hours at 163°C . Thermal strains from all four gages were measured simultaneously in the temperature range of -101°C to 121°C . Figures 59-62 show some typical strain data recorded. The longitudinal thermal strains are corrected for the transverse sensitivity of the strain gages. An average CTE of three specimens is found to be $-1.18 \times 10^{-6}/^{\circ}\text{C}$ for XN70/RS3 and $0.75 \times 10^{-6}/^{\circ}\text{C}$ for AS4/3501-6. The transverse thermal strains show linear behavior (with a CTE of $29.7 \times 10^{-6}/^{\circ}\text{C}$ for XN70/RS3 and $26.1 \times 10^{-6}/^{\circ}\text{C}$ for AS4/3501-6) and are an order of magnitude greater than the longitudinal strains. The results for XN70/RS3 compare very well with the results obtained using a Michelson laser interferometer by Precision Measurements and Instruments Co. under a Hughes Aircraft contract, Space and Communications Division (an average of four specimens of XN70/RS3 – 1.24×10^{-6} for longitudinal CTE and 31.60×10^{-6} for transverse CTE [6]).

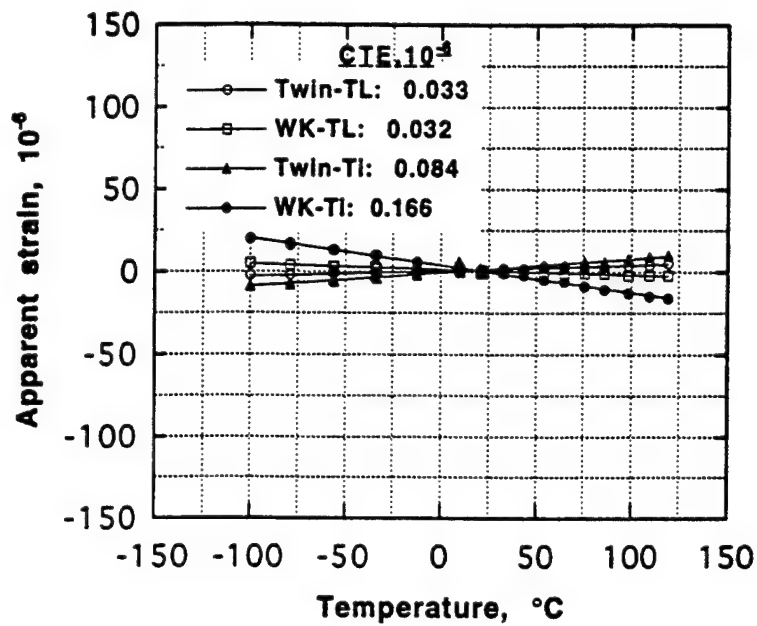


Figure 56. Apparent Strain for WK-Series Strain Gages.

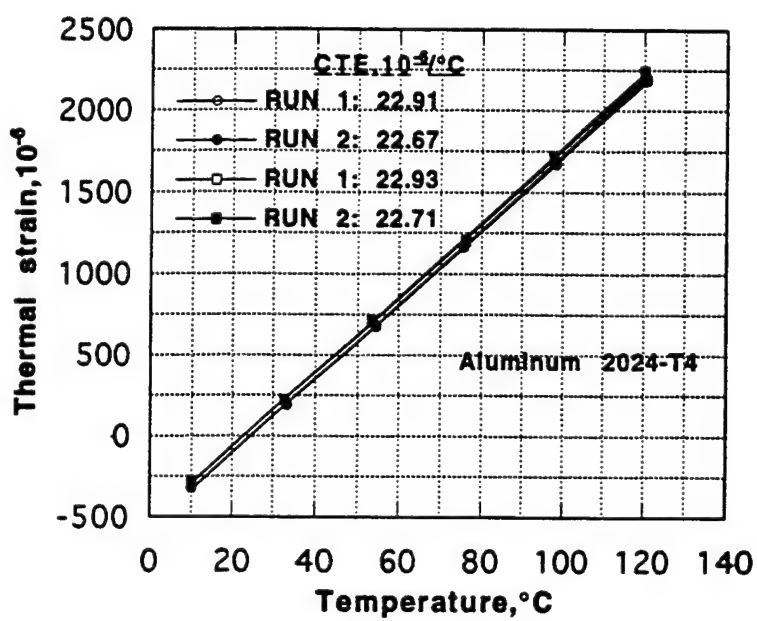


Figure 57. Thermal Strain vs. Test Temperature for Aluminum.

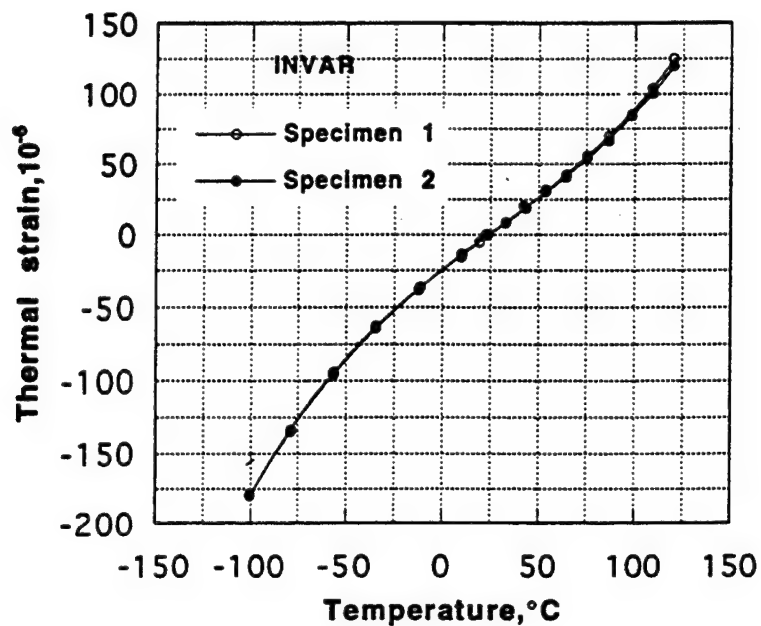


Figure 58. Thermal Strain vs. Test Temperature for Invar.

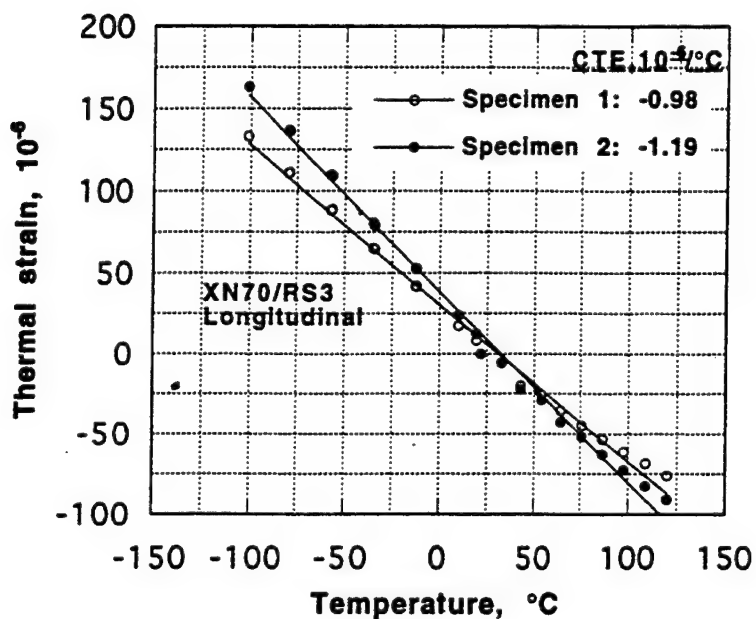


Figure 59. Thermal Strain in the Longitudinal Direction vs. Temperature for XN70/RS3 Unidirectional Specimen.

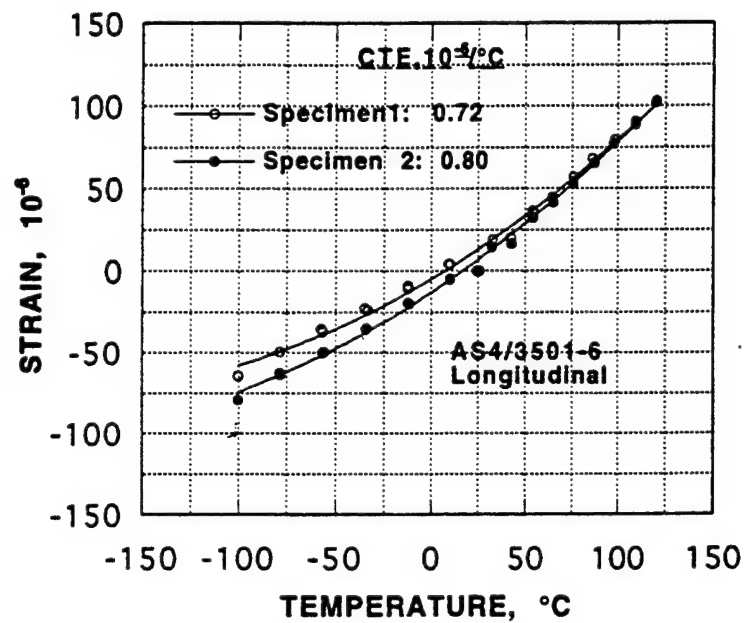


Figure 60. Thermal Strain in the Longitudinal Direction vs. Temperature for AS4/3501-6 Unidirectional Specimen.

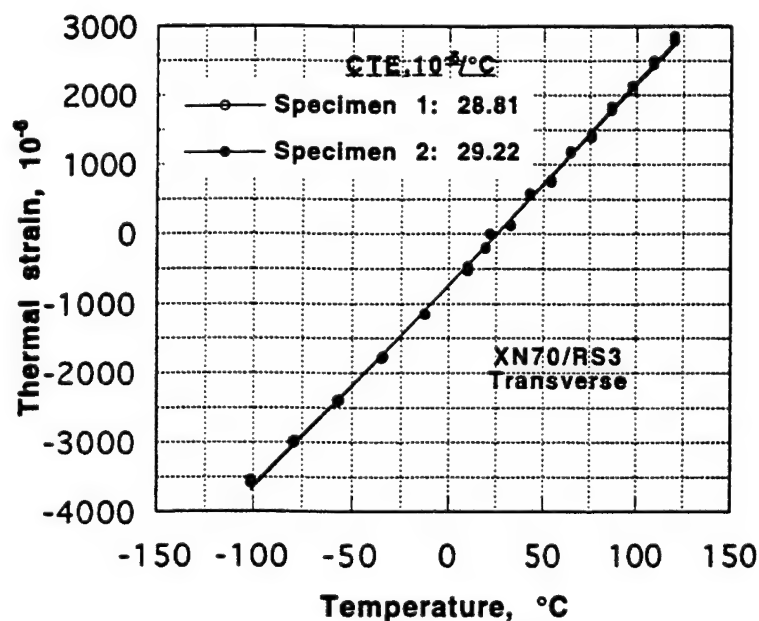


Figure 61. Thermal Strain in the Transverse Direction vs. Temperature for XN70/RS3 Unidirectional Specimen.

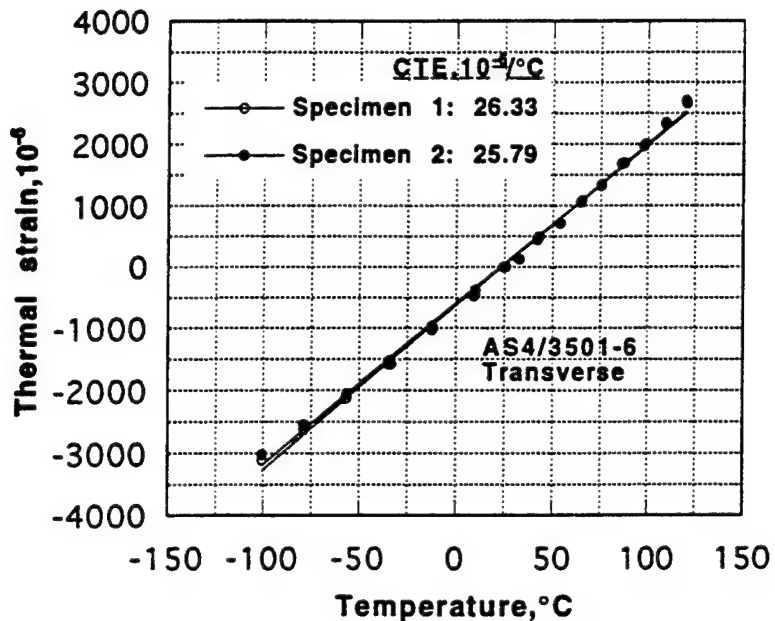


Figure 62. Thermal Strain in the Transverse Direction vs. Temperature for AS4/3501-6 Unidirectional Specimen.

2.4.1.3 CTE of Off-Axis and Multidirectional Composites

The CTEs of unidirectional composites of XN70/RS3 at angles of 5, 10, 15, 30, 45, 60, 75, 80, and 85° to the fiber direction were calculated using the longitudinal and transverse CTEs determined above and laminated plate theory and the results compared with experimental data. Two strain gages were mounted on each specimen at right angles to each other to simultaneously obtain thermal strains for two off-axis angles. For small off-axis angles, the correction for transverse sensitivity becomes significant, and it was therefore employed for all thermal strains. Figure 63 shows a comparison of the experimentally-determined CTEs with analytical predictions calculated from classical laminated plate theory. In most cases experiment and prediction agree well. Slight discrepancies in some cases are possibly due to a limitation of the current technique with respect to apparent strains from the strain gages and the difficulty in accurately aligning strain gages along small off-axis angles.

CTEs of $[0/90]_{4S}$ and $[0/90/\pm 45]_{2S}$ laminates of AS4/3501-6 were only determined experimentally. Specimens, 5 cm x 5 cm in size, were sectioned and their edges polished. The thermal strains of both laminate orientations, shown in Figures 64 and 65, appear to be fairly linear in the temperature range studied. Theoretically, longitudinal and transverse

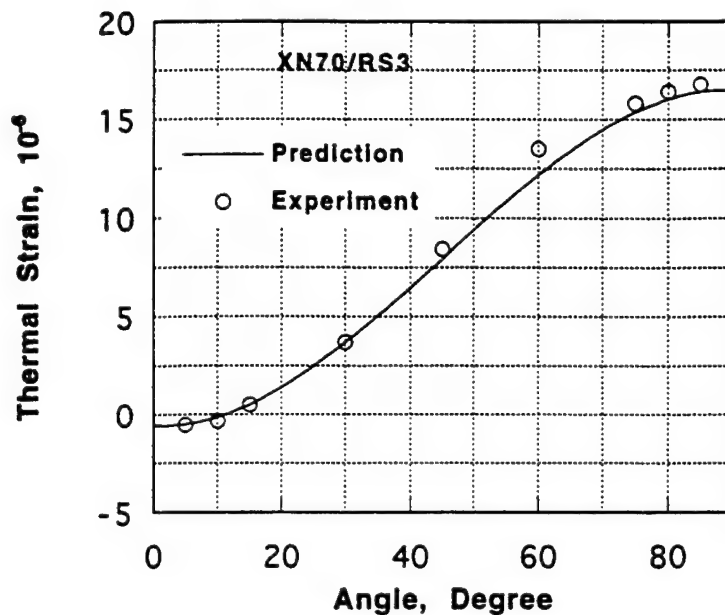


Figure 63. Comparison of CTE between Prediction and Experiment for a Variety of the Off-Axis Angles for XN70/RS3 Composites.

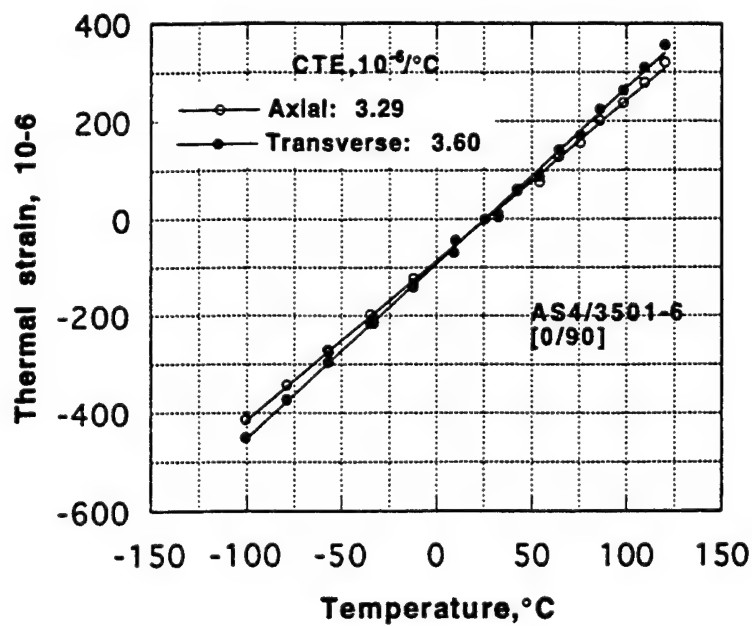


Figure 64. Thermal Strain vs. Temperature for the $[0/90]_{2s}$ of AS4/3501-6 Composite.

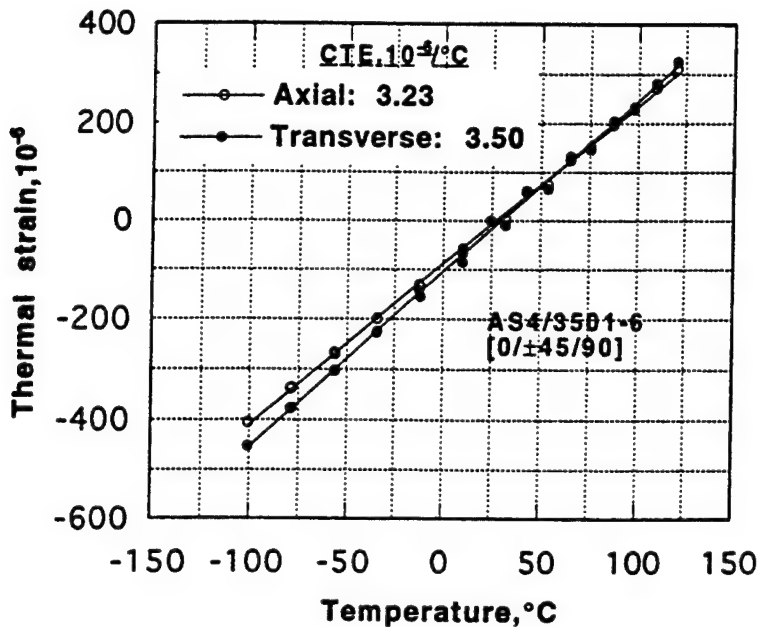


Figure 65. Thermal Strain vs. Temperature for the $[0/\pm 45/90]_s$ of AS4/3501-6 Composite.

strains in both cross-ply and quasi-isotropic laminates are identical, and the predicted CTE is $3.4 \times 10^{-6}/^{\circ}\text{C}$. The experimental values, on the other hand, are $3.44 \times 10^{-6}/^{\circ}\text{C}$ for the cross-ply laminate and $3.37 \times 10^{-6}/^{\circ}\text{C}$ for the quasi-isotropic laminate.

2.4.1.4 Influence of Microcracking on Laminate CTE

Cross-ply $[0/90]_{4s}$ laminates of AS4/3501-6 were used to investigate the change in laminate CTE due to microcracking brought about by mechanical loading, and simultaneously evaluate the sensitivity of this CTE measurement technique. The 15-cm x 2.5-cm coupons were tested under incremental tensile loading. The CTE of the specimen was measured prior to loading. This specimen was loaded to the stress level above the first-ply failure stress and unloaded for crack spacing and CTE measurements. This procedure was repeated three to four times until the cracks were saturated. Table 7 shows the crack density and CTE change under incremental loading.

Microcracking, induced by mechanical loading, is reflected in a change in laminate CTE. However, due to the very high stiffness in the fiber direction, the absolute change in CTE is minimal. The use of strain gages provides the flexibility to correlate localized damage with changes in composite CTE.

TABLE 7

CHANGES IN AS4/3501-6 LAMINATE STIFFNESS AND CTE WITH MICROCRACKING

Laminate	Applied Stress (ksi)	Average Crack Density		Laminate Modulus (Msi)	Average CTE (ppm/°C)
		90° plies (in ⁻¹)	45° plies (in ⁻¹)		
[0/90] _{2S}	0	0	-	10.48	3.31
	50	0	-	10.48	3.31
	80	26.7	-	10.15	2.95
	100	50.7	-	9.99	2.68
	100	52.0	-	-	2.47
[0/45/90/-45] _S	0	0	0	7.28	3.24
	50	56.0	4.0	7.21	2.75
	70	102.4	16.0	6.94	2.14
	73	110.4	32.0	-	1.85

2.4.2 Wright Connection: Edge Effects on Microcracks

Advice and training were given to three Northmont High School teachers participating in the Air Force Wright Connection program. Optical microscopy was performed on cyanate ester composite specimens (XN70/RS3) thermally cycled by Hughes Spacecraft. The purpose of this research was to investigate whether cracks initiating at the edge of samples are caused by the free edge, and therefore the small coupon sample size overestimates the total number of cracks in real composites.

2.4.3 Processing of XN70A/RS3

The autoclave cure cycle recommended by Hughes for XN70A/RS3 resulted in voidy laminates. An ionic viscosity measurement conducted on the prepreg during cure (Figure 66) shows that pressure application occurs after the resin has gelled. A new cure cycle was developed which applies pressure when the viscosity begins to rise, as shown in Figure 67. This new cure cycle resulted in high quality laminates. In another study a modified, large-area sensor was used to determine that RS3 resin begins to wet the breather while under vacuum pressure at approximately 120°F. It is therefore important to utilize bagging films which will reduce resin flow to prevent excess resin loss.

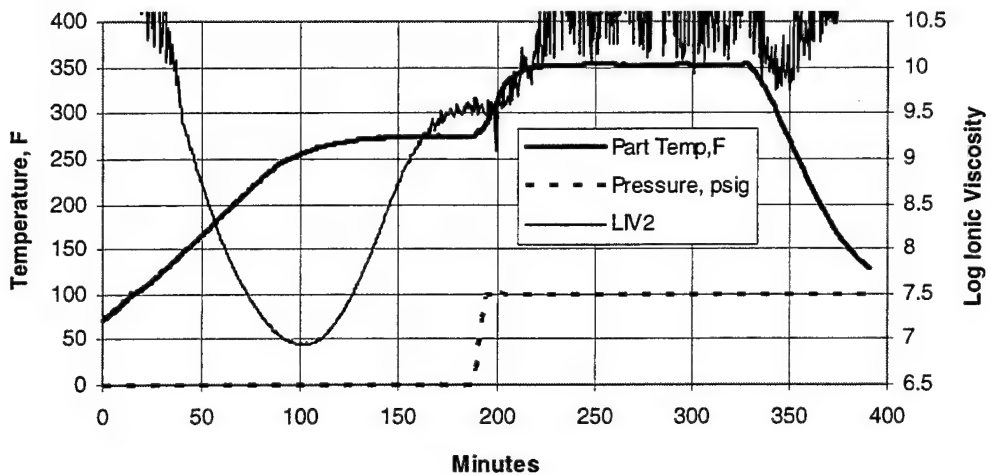


Figure 66. Autoclave Cure of XN70A/RS3 with Hughes Cure Cycle.

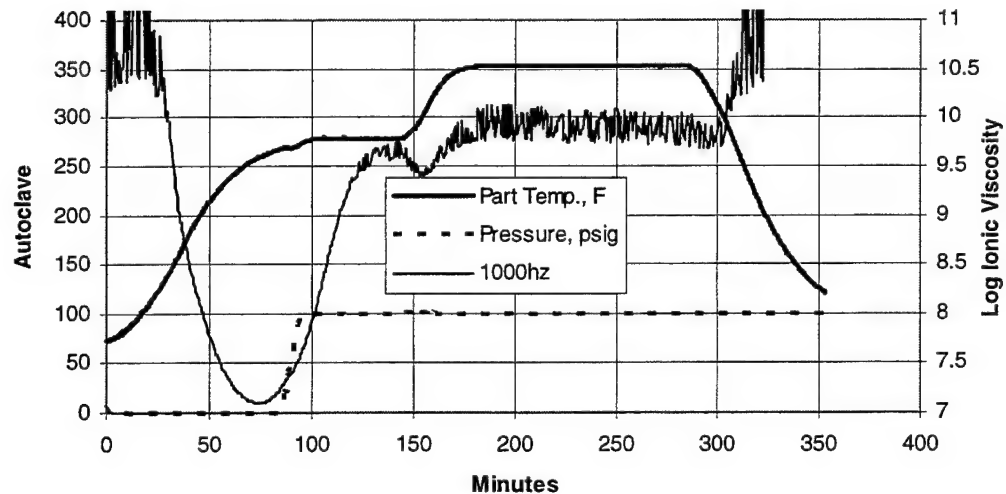


Figure 67. Autoclave Cure of XN70A/RS3 with Modified Cure Cycle.

2.5 DAMAGE INITIATION IN COMPOSITE LAMINATES UNDER MECHANICAL AND THERMAL CYCLIC LOADINGS

Composite laminates exhibit damage before final failure under applied mechanical loading as well as thermal loading. Ply failure and free-edge delamination are the major initial damages observed in composites, and a great amount of work has been reported in the literature regarding prediction of initiation and the nature of damage under static mechanical loading. However, very little work has been reported on this problem under mechanical and thermal cyclic loadings.

The objective of this work is to develop the predictive capability of initial damage due to transverse cracking and delamination of composite laminates subjected to mechanical cyclic loadings as well as thermal cyclic loadings and a combination of both. Thermal cycling, like the mechanical cyclic loading, produces cyclic stress on each ply within a laminate due to the mismatch of the coefficient of thermal expansion of the ply orientation.

Cross-ply laminates of $[0_2/90_2]_S$ orientation and quasi-isotropic laminates of $[90_2/\pm 30]_S$ orientation were used for the transverse matrix cracking and onset of delamination, respectively. The free-edge delamination occurs in the $[90_2/\pm 30]_S$ laminate under applied axial compression prior to first-ply failure. The material system chosen is carbon fiber-reinforced toughened BMI composites (IM7/5250-4). All panels were fabricated from prepreg tape according to the manufacturer's recommended cure cycle and subjected to postcure and examined by ultrasonic C-scan. The average fiber volume was found to be 63.3 percent with the coefficient of variation at 3.5 percent. Test specimens were cut from composite panels, and free edges were polished for microscopic examination of ply failure and delamination. This work is currently involved in the onset of delamination due to mechanical loading.

2.5.1 Analytical Background and Approach

The thermomechanical properties of the material system are determined by experiment for analytical calculations and are listed in Table 8.

The stress-free temperature, ΔT , was determined by both unsymmetric $[0_4/90_4]_T$ laminate strips and peel ply technique using $[0_5/90_{10}/0_5]_T$.

The ply stresses in the cross-ply laminate were determined by laminate plate theory, taking into consideration curing residual stresses. The interlaminar stresses at the free-edge region were calculated, using a global-local model, taking into consideration curing residual stresses [7]. The maximum-stress failure theory was applied to predict the first-ply failure and the onset of delamination. Because of the presence of a severe stress gradient along the free edge of the specimen, the concept of an effective stress (the average stress over a distance from the free edge equivalent to one-ply thickness) was utilized [8].

In order to predict the onset of delamination and the first-ply failure for a given fatigue load (below the static load), S-N curves are established for transverse loading and in-plane shear loading. Experimental study shows that the interlaminar shear strength appears to be equal to the in-plane shear strength [9]. From these S-N curves and the calculated critical

TABLE 8
THERMOMECHANICAL PROPERTIES OF IM7/5250-4

E_{11} , ksi	24
$E_{22}=E_{33}$, ksi	1.57
$G_{12}=G_{13}$, ksi	0.84
$\nu_{12}=\nu_{13}$	0.31
ν_{23}	0.56
α_L , min/in/°F	0.25
α_T , min/in/°F	12.3
ΔT , °F	-275
Y^* , psi	9,870
S^* , psi	17,700

*Y = transverse strength and S = shear strength

stress component in the respective laminate, the number of fatigue cycles for damage initiation is calculated for a given applied load. Specimens for the S-N curves for transverse and shear loading were subjected to tension-tension sinusoidal stress with 10 Hz of frequency, considering four different stress amplitudes to obtain life data. The S-N relations for transverse and shear loading were used $[90]_{8T}$ and $[\pm 45]_{2S}$, respectively. Five replications were tested at each stress level. The fatigue life data were statistically reduced using the procedure described in Reference [10].

2.5.2 Free-Edge Delamination Results

All specimens were five inches long (two inches in gage section) and were tested under compression with the aid of an antibuckling device. Four specimens were tested under static compression to determine the stress level for onset of delamination. The onset of delamination was determined by visual observation of the entire free edges during testing. The onset of delamination was accompanied by an audible noise and a change in load-deflection curve. After observation of delamination, the specimen was immediately unloaded and the free edge examined to confirm the delamination and determine at which interface delamination occurred.

The onset of delamination was also investigated under compression-compression fatigue with $R=0.1$ and a frequency of 10 Hz. The dimensions, antibuckling device, and delamination observation were identical to the static loading case. Two fatigue stress levels were

chosen and three specimens tested at each stress level until the onset of free-edge delamination was observed. Because of the visual observation, the fatigue stress levels were chosen in such a way that all delaminations occurred within a couple of hours. An effort is being made to improve the detection of the onset of delamination under fatigue loading using an acoustic emission technique.

Figures 68-71 show the distribution of interlaminar stresses at the 30/-30 interface and at the midplane in the free-edge region, calculated using the global-local model, due to the curing residual stresses and mechanical loading. Interlaminar stresses were calculated for -275°F temperature difference and for 100 psi of the applied compressive loading. The maximum-stress theory predicts delamination at the 30/-30 interface due to the interlaminar stress of τ_{xz} . The photomicrograph shown in Figure 72 shows delamination at the predicted interface under static loading. Delamination occurred at the interface for all specimens and in many cases turned into the middle -30 ply and caused the whole mid-ply failure. Fatigue life data for the [90/ \pm 30]_s laminate are plotted in the S-N curve shown in Figure 73. The interlaminar shear stress, τ_{xz} , was calculated for the maximum fatigue stress applied to the laminate specimen and used for comparison. All delamination under fatigue loading also occurred at the 30/-30 interface as shown in Figure 72. This work is continuing.

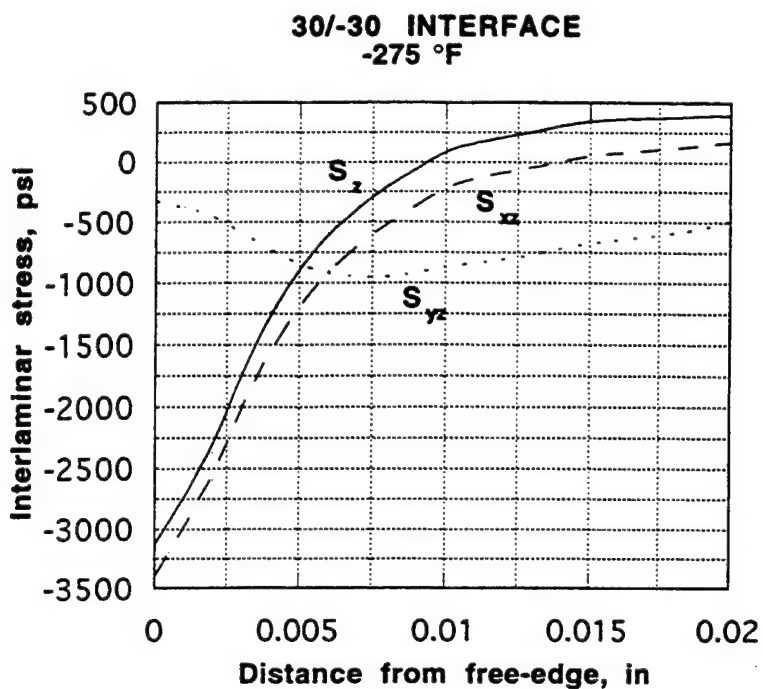


Figure 68. Interlaminar Stress Distribution at the 30/-30 Interface Due to Residual Curing Stress.

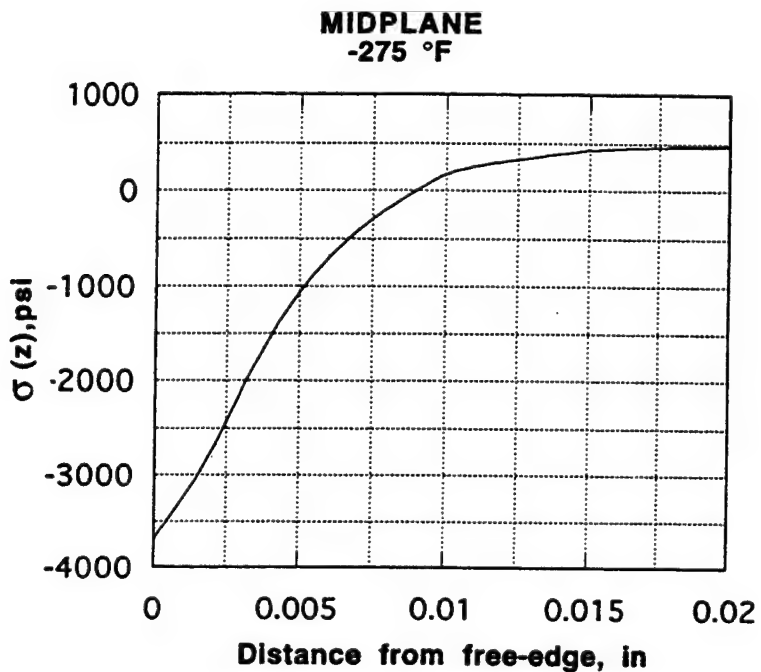


Figure 69. Interlaminar Stress Distribution at the Midplane Due to Residual Curing Stress.

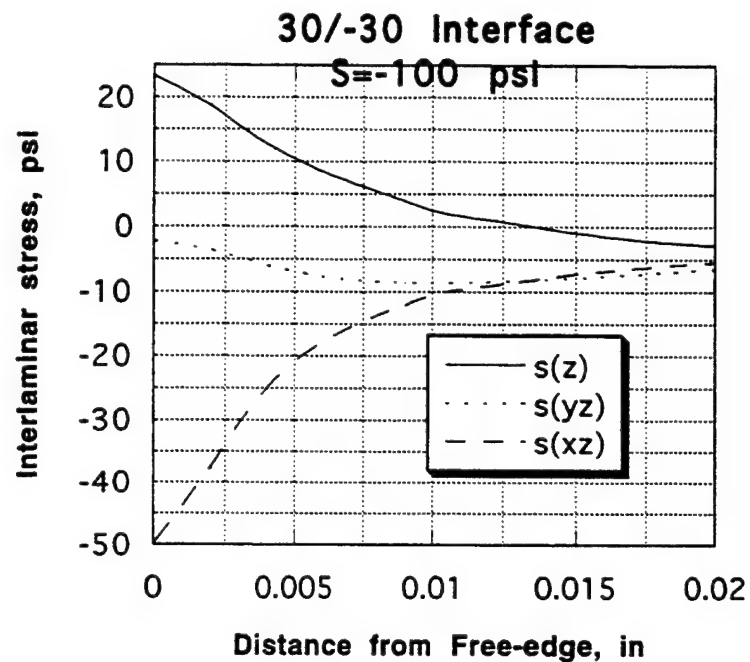


Figure 70. Interlaminar Stress Distribution at the 30/-30 Interface Due to Mechanical Loading.

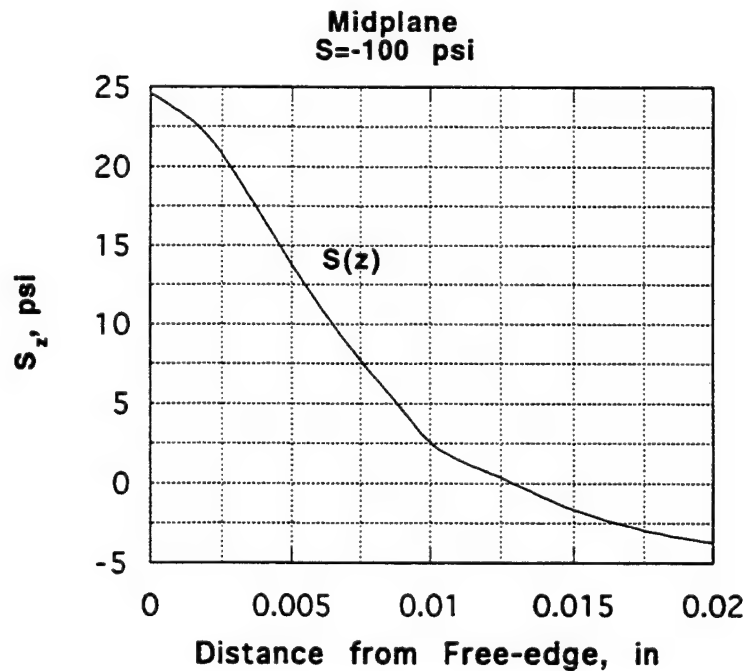


Figure 71. Interlaminar Stress Distribution at the Midplane Due to Mechanical Loading.

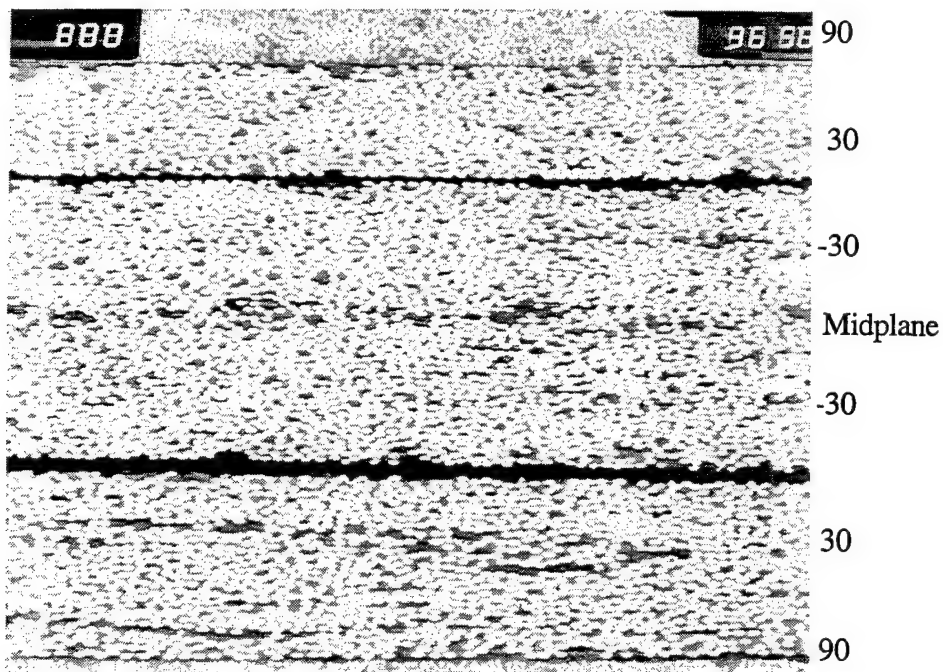


Figure 72. Microphotograph Showing Free-Edge Delamination Under Static Loading.

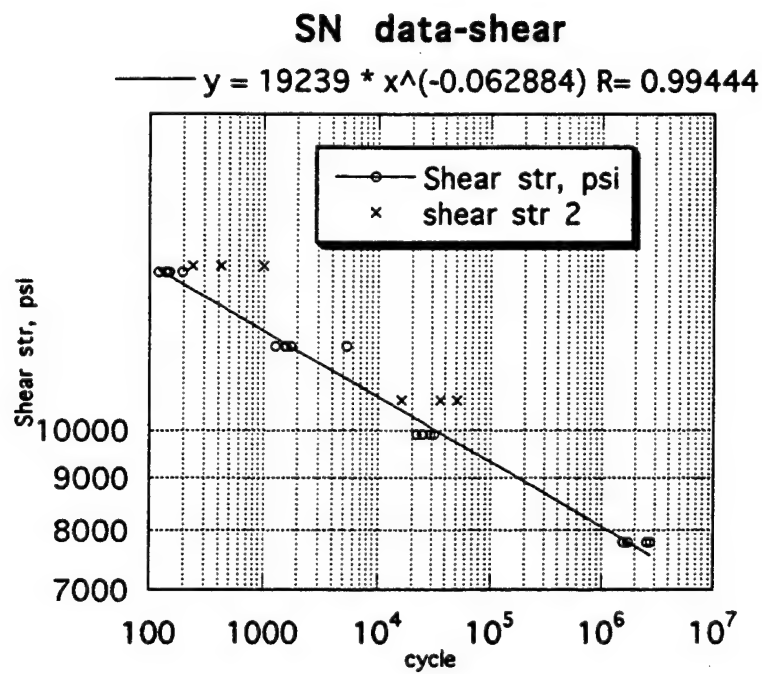


Figure 73. Interlaminar Shear S-N Relation. Symbol x represents the fatigue data obtained from $[90_2/\pm 30]_S$ specimen under compression-compression cyclic loading.

SECTION 3

PROCESSING SCIENCE OF COMPOSITES/TASK 3

3.1 INTEGRATION OF SENSORS FOR INTELLIGENT COMPOSITES PROCESSING

The major work in this area has been the use of a back-propagation neural network (BNN) for modeling material behaviors such as reaction rate, dc-resistance, and viscosity changes during cure. These models allow the prediction of process behavior and interpretation of monitored sensor data.

3.1.1 Neural Network Development Tool

Neural network software has been modified to run under the new 32-bit version of Visual Basic and Neural Windows. Some tests have been conducted to compare the performance of the new 32-bit version. There is some, but not significant, improvement in program execution speed; however, the new version of the language is likely to be the new standard for Windows programming and will be adopted for future software development.

3.1.2 Neural Network Model for Reaction Rate

A paper describing the neural network reaction rate model for Hercules 3501-6 has been submitted for presentation at the 28th International SAMPE technical conference in November 1996 [11]. This section outlines the results presented in that paper and some additional findings that were not included in the paper.

The neural network structure for the reaction rate model is shown in Figure 74. We shall refer to this structure as a 2-5-4-1 network. The first number represents the number of neurons in the input layer, and the last, that in the output layer. The numbers in between represent the number of neurons in the hidden layers. The input layer of the network contains two neurons: temperature and degree of cure. The output layer contains a single neuron which is the reaction rate. This reaction rate is integrated over time to yield degree of cure which becomes the input for the next time step. The 2-5-4-1 network is the simplest structure that has yielded good results. In a later section some observations on other network structures are summarized.

The neural network was trained by using temperature, degree of cure, and reaction rate data from DSC runs at 0.2, 1, 2, and 5°C/min ramp rates. Figure 75 shows the four sets of data used for training. These data were presented to the network without any particular sequence

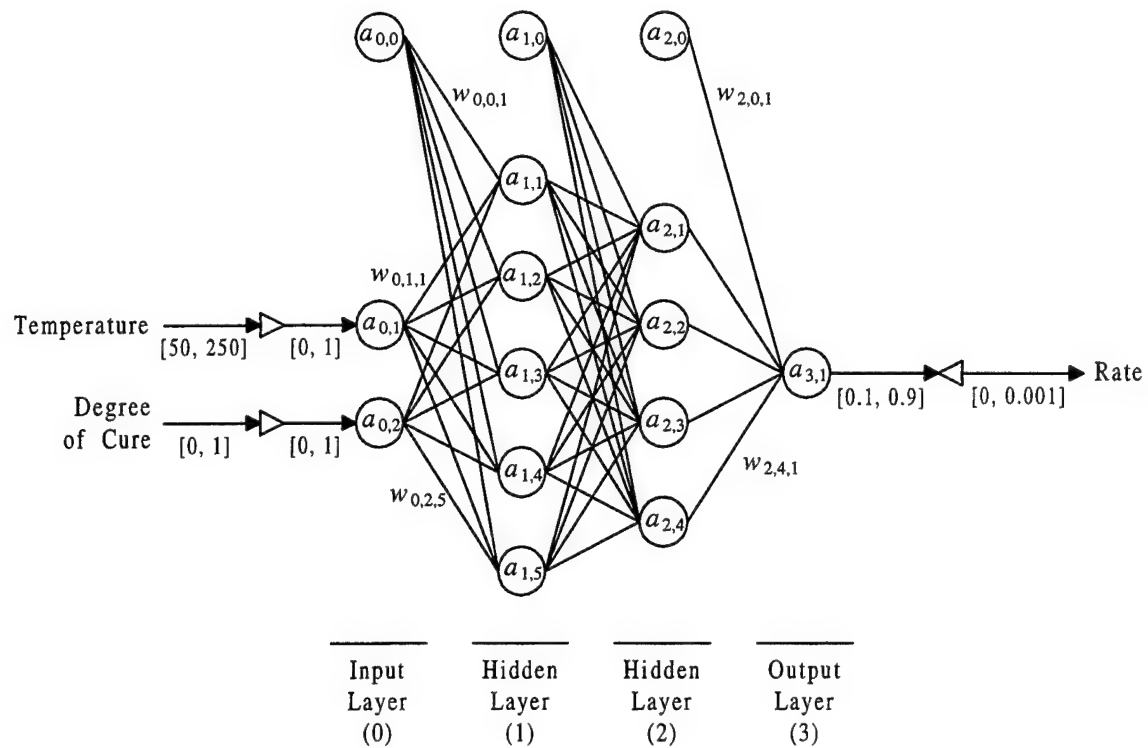


Figure 74. The Structure of the Back Propagation Neural Network Reaction Rate Model.

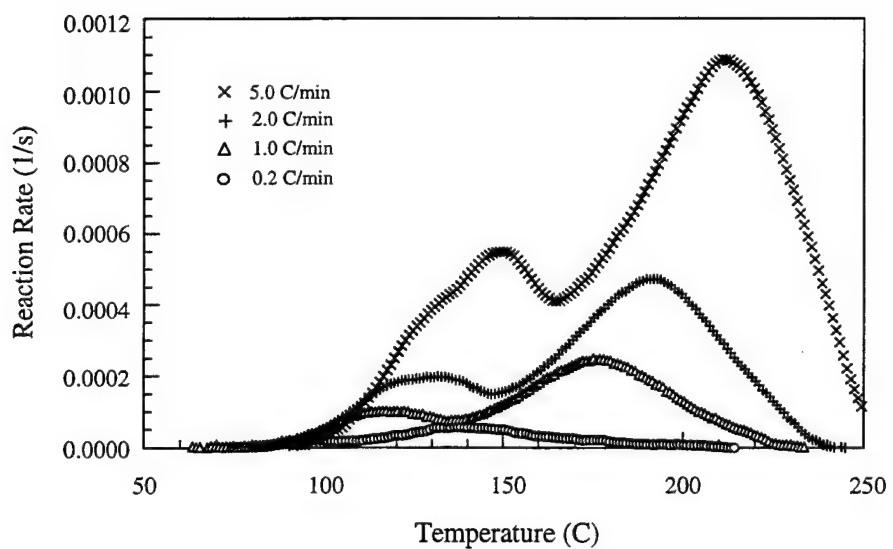


Figure 75. The Training Set from DSC Scans at 0.2, 1, 2, and 5°C/min.

in time or temperature. The link weights of the network after 10,000 iterations were used as the model parameters. Table 9 lists the link weights for the neural network reaction rate model. The inputs, temperature, and degree of cure are scaled to yield the activities of the neurons in the first layer, $a_{0,1}$ and $a_{0,2}$ (see also Figure 74). The activities of the neurons in the subsequent layers are calculated using the following code segment with link weights, $w_{i,j,k}$, given in Table 9. (It should be noted that this code segment is the same for any neural network model.) The activity of the last layer, $a_{3,1}$, is then rescaled to yield the output, the predicted reaction rate.

```

FOR i = 1 TO nLayers - 1
  FOR j = 1 TO nNeurons(i)
    s = 0
    FOR k = 0 TO nNeurons(i - 1)
      s = s + a(i - 1, k) * w(i - 1, k, j)
    NEXT
    a(i, j) = 1 / (1 + EXP(-s))
  NEXT
NEXT

```

TABLE 9
LINK WEIGHTS ($w_{i,j,k}$) OF THE BNN REACTION RATE MODEL
FOR 3501-6 EPOXY RESIN

		$k = 1$	2	3	4	5
$i = 0$	$j = 0$	-28.5113	-5.2629	-7.2896	5.1274	-4.6926
	1	6.2032	0.8277	10.7357	9.6543	11.9382
	2	20.6651	21.9899	0.1172	-14.9512	-4.0963

		$k = 1$	2	3	4
$i = 1$	$j = 0$	-5.5719	-4.1387	-4.3776	0.8924
	1	-3.8342	14.0272	0.8261	0.6289
	2	-7.2250	3.0481	4.1117	7.3470
	3	4.9659	0.7964	4.7585	2.5187
	4	4.3182	-2.1499	-1.8305	-0.6892
	5	5.3127	-1.6449	2.9860	-4.1794

		$k = 1$
$i = 2$	$j = 0$	-5.5859
	1	5.8232
	2	-7.1419
	3	1.3189
	4	3.6830

For verification of the model, a DSC run was made using a standard cure cycle with a shorter hold at 350°F so that the resin was not fully cured. The neural network model predicted a 92 percent degree of cure, while the DSC data indicated a 95 percent degree of cure. Compared to the Loos-Springer model, which predicted 100 percent cure, the neural network model gives a more accurate prediction. These results are shown in Figure 76. The neural network model was also verified by comparing the predicted reaction rate and degree of cure to data obtained by thermopiles in 1990 (Figures 77 and 78). In all cases the neural network model performed better than the analytical Loos-Springer model. In some cases the thermopile yields better reaction rate data than does the DSC, as the DSC causes a baseline shift when there's a change in the heating rate.

The BNN model predicted degree of cure results for 3501-6 resin under four isothermal conditions were also compared to published Tg data as shown in Figure 79. The BNN model was able to predict under cure conditions as the Tg data suggested, while the Loos-Springer model always predicted complete cure. For these isothermal hold conditions, the BNN model appears to perform much better than the Loos-Springer model.

3.1.3 Neural Network Models for dc-Resistance and Viscosity

The Rheometrics system was used for measurement of dc-resistance and viscosity of the resin to provide training data for the neural network models. Data for temperature and viscosity were measured using the Rheometrics system, and those for dc-resistance were measured concurrently using a PC-based data acquisition system.

The neural network structure used for the reaction rate model was used for the dc-resistance model as well as the viscosity model. Both models use temperature and degree of cure as input. Data for degree of cure were calculated using a previously-developed neural network reaction rate model based on temperature and degree of cure. Four runs at 0.2, 1, 3, and 5°C/min temperature ramp rates were made. The dc-resistance data were shifted to have an initial value of $10^7 \Omega$ at 50°C with the assumption that the degree of cure at this point is zero. The training data for the dc-resistance model and viscosity model are shown in Figure 80. Similar to the development of the reaction rate model, each dc-resistance model and viscosity model was obtained by training a 2-5-4-1 network over 10,000 iterations. The resulting link weights for these two models are shown in Tables 10 and 11. The models were verified by data from a standard cure cycle, and the results are shown in Figure 81. The results are satisfactory for both dc-resistance model and viscosity model. Although the accuracy of the viscosity model appears to be better than that of the dc-resistance model, the dc-resistance data provide more detail at the

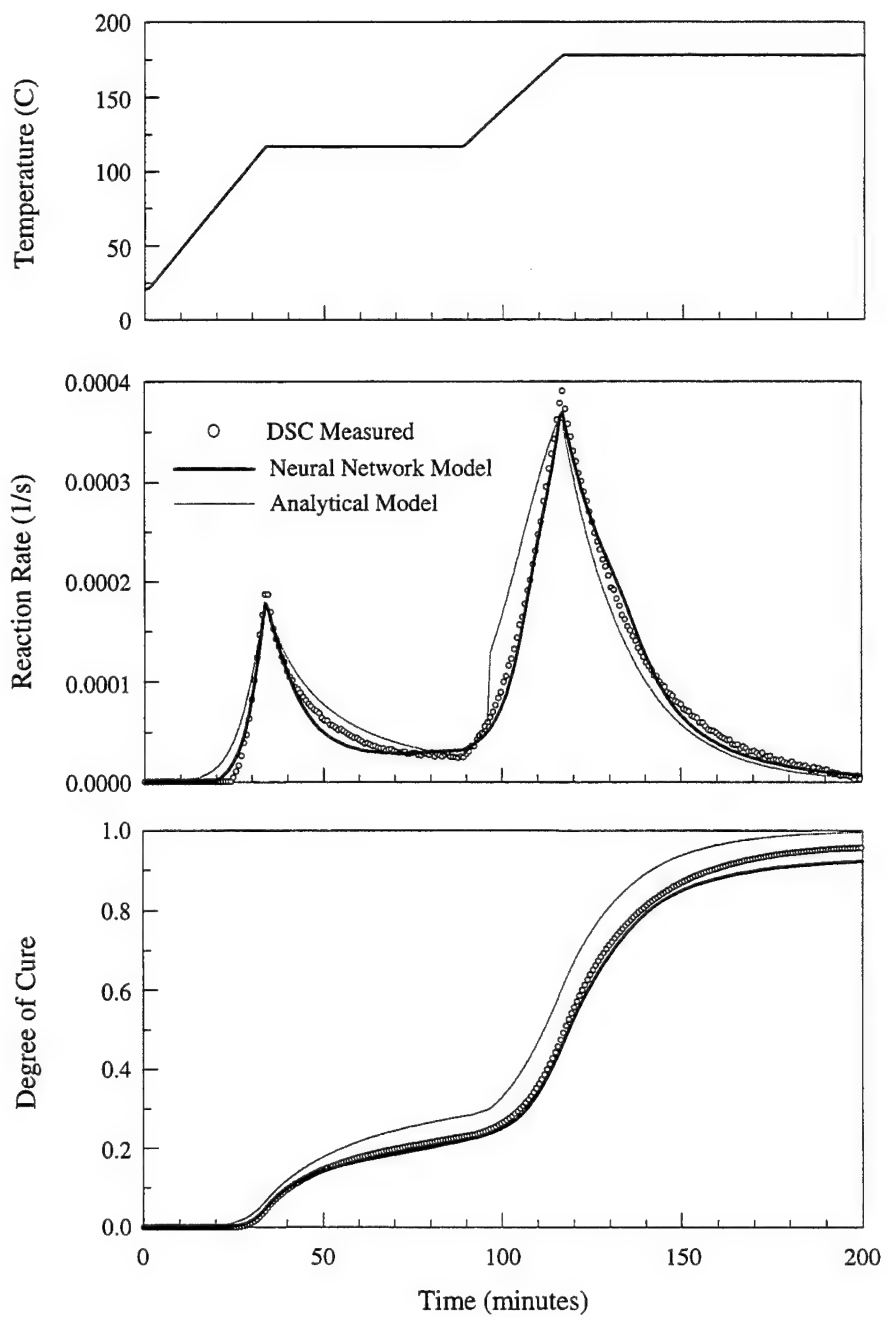


Figure 76. Verification of BNN Model Against DSC Data and Comparison to Loos-Springer Analytical Model.

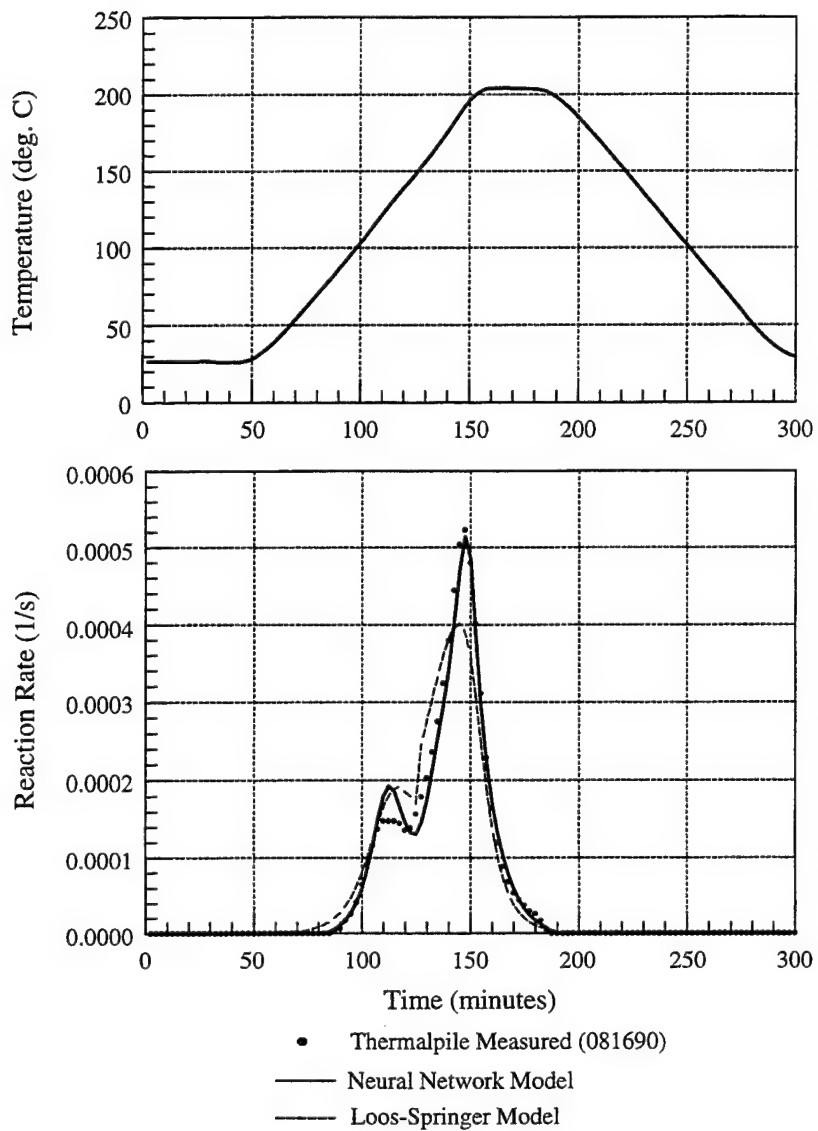


Figure 77. Verification of BNN Model Against Thermopile Data from a Single Ramp Cycle and Comparison to Loos-Springer Analytical Model.

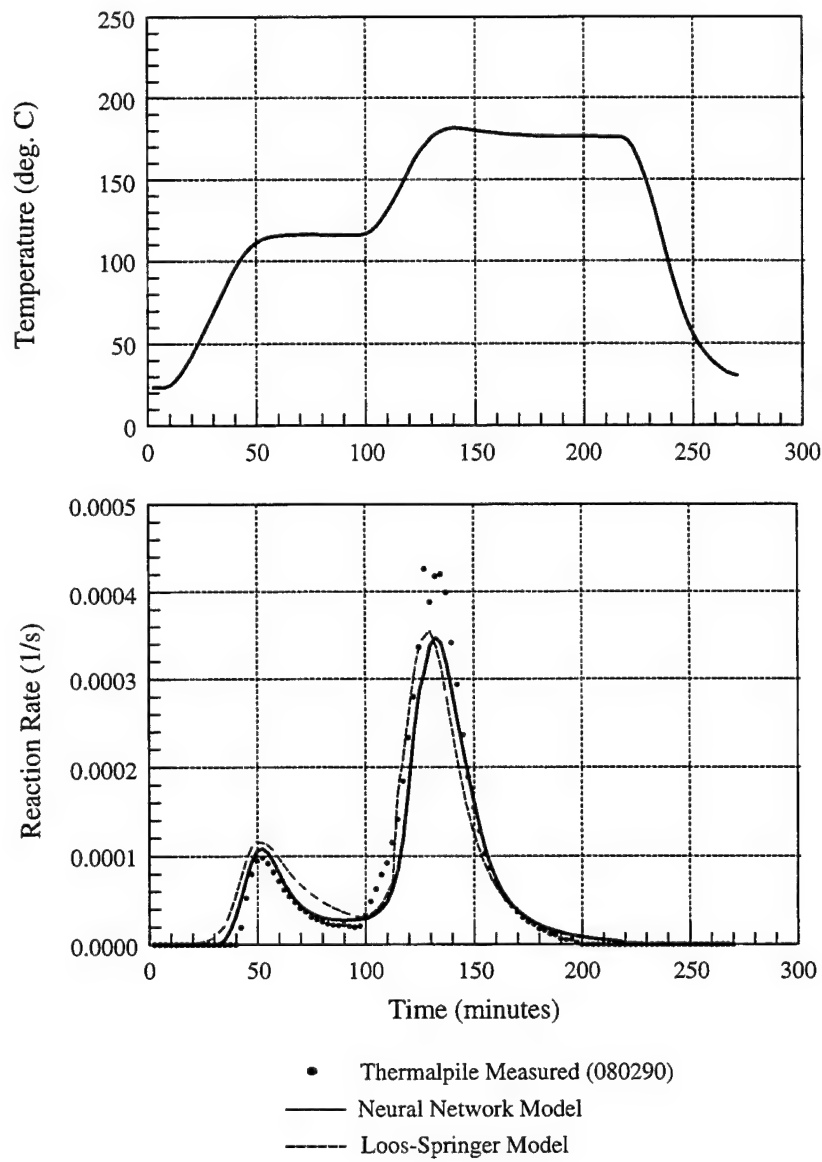


Figure 78. Verification of BNN Model Against Thermopile Data from a Standard Cure Cycle and Comparison to Loos-Springer Analytical Model.

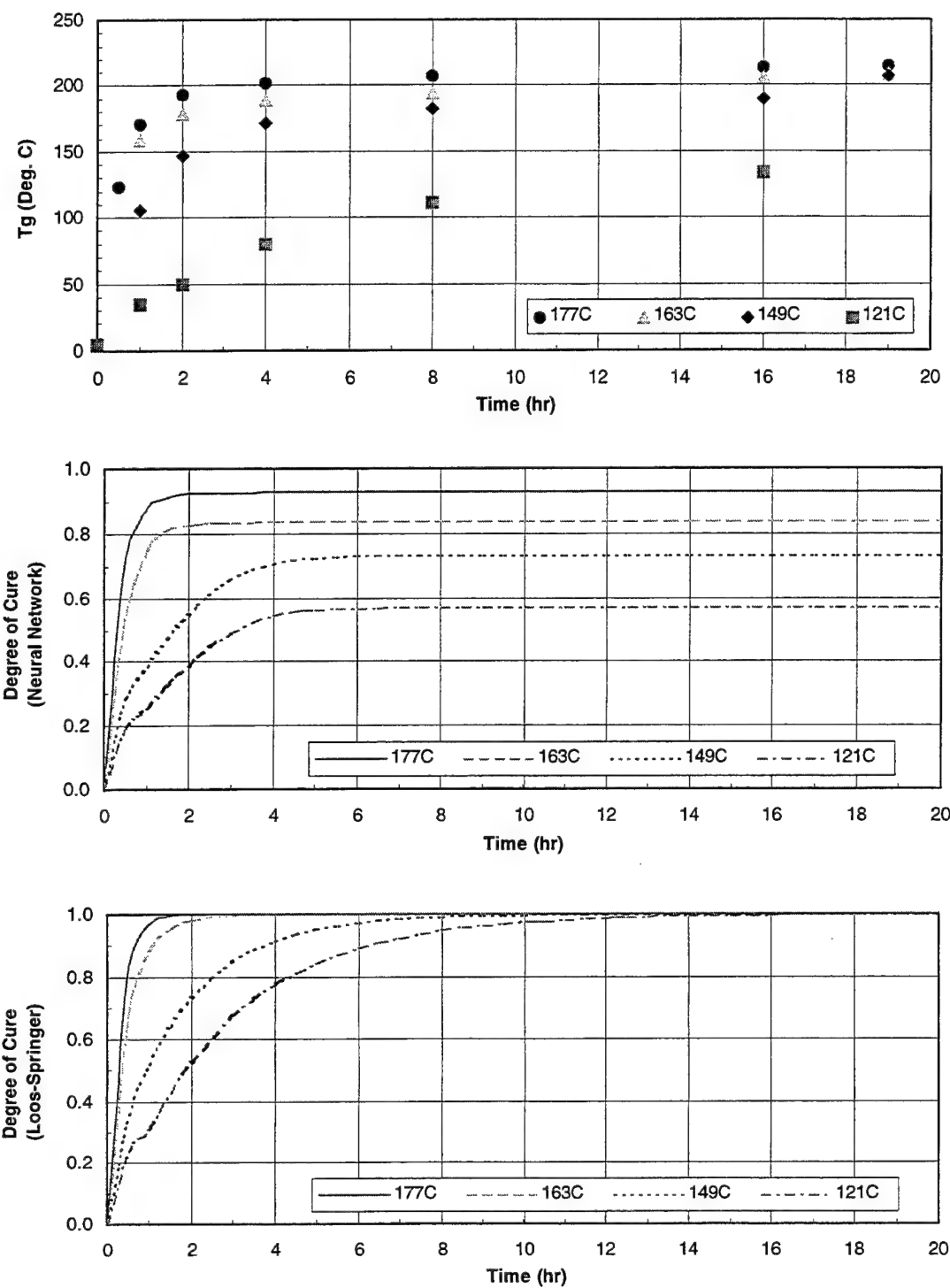


Figure 79. Glass Transition Temperatures and Predicted Degree of Cure of Hercules 3501-6 Resin Undergoing Isothermal Cure Reaction.

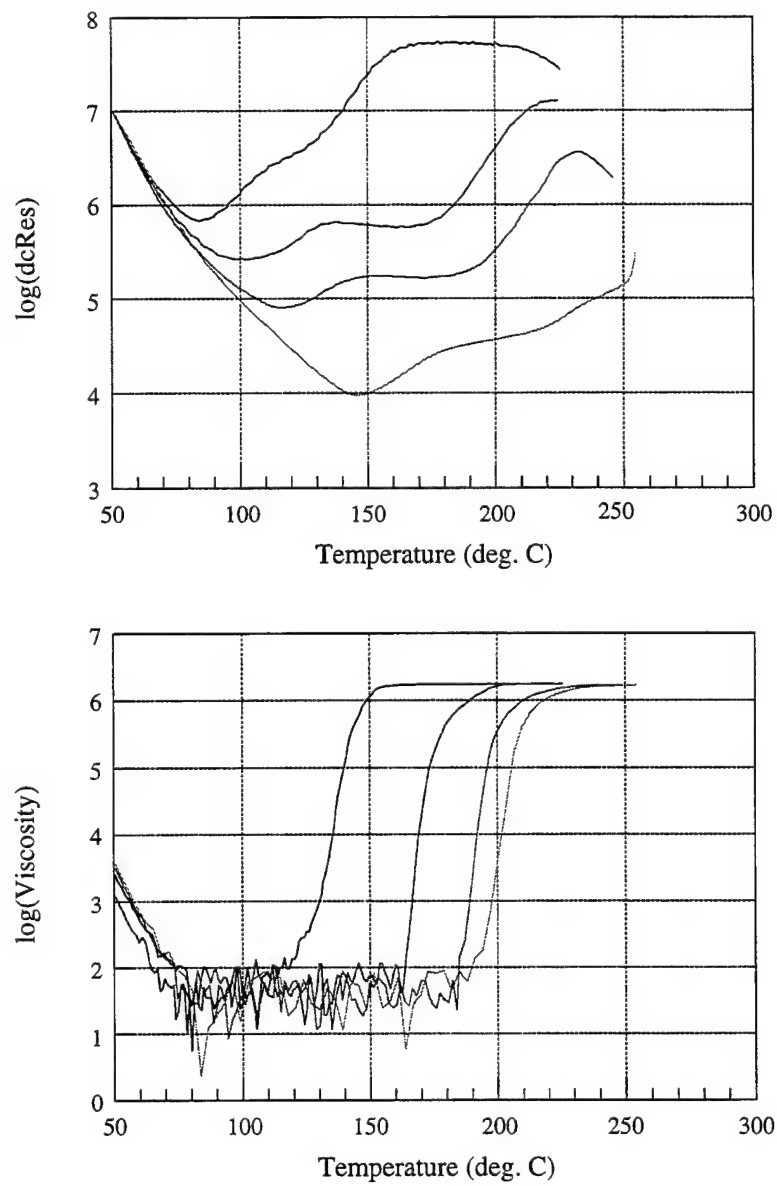


Figure 80. Measured dc-Resistance and Viscosity of 3501-6 Resin at Different Temperature Ramp Rates for Training the BNN Models. The top curve was measured at 0.2°C/min, and the subsequent ones were at 1, 3, and 5°C/min, respectively.

TABLE 10
LINK WEIGHTS ($w_{i,j,k}$) OF THE BNN dc-RESISTANCE MODEL
FOR 3501-6 EPOXY RESIN

		$k = 1$	2	3	4	5
$i = 0$	$j = 0$	9.2919	5.8444	1.0147	-7.3017	0.3524
	1	1.5287	-14.6627	-9.4017	5.8798	-5.5314
	2	-9.3150	3.4933	8.5657	1.1633	14.9903

		$k = 1$	2	3	4
$i = 1$	$j = 0$	-1.6880	3.5349	0.0819	-3.8577
	1	-7.7926	3.5607	-3.3867	-1.6823
	2	3.1509	-4.7906	2.1674	10.8107
	3	5.9156	1.1973	-0.0729	5.3406
	4	5.2572	-0.2352	3.9738	-6.8776
	5	0.6003	-1.9445	4.6931	6.9368

		$k = 1$
$i = 2$	$j = 0$	-4.1788
	1	3.8754
	2	-2.6801
	3	1.7149
	4	5.4905

TABLE 11
LINK WEIGHTS ($w_{i,j,k}$) OF THE BNN VISCOSITY MODEL FOR 3501-6 EPOXY RESIN

		$k = 1$	2	3	4	5
$i = 0$	$j = 0$	6.8084	-0.4560	0.1918	-2.2421	1.6338
	1	-0.1635	4.1622	-0.7046	8.1451	-7.3937
	2	-11.7072	-0.9181	2.3595	-2.1832	11.7862

		$k = 1$	2	3	4
$i = 1$	$j = 0$	0.4232	1.6979	-2.3971	0.7249
	1	4.9726	0.8294	10.1255	-0.1020
	2	-0.1275	1.1034	2.3170	1.8206
	3	-2.0445	0.9546	-1.9816	0.7016
	4	2.2550	1.0135	5.0660	3.2738
	5	-2.0529	1.0892	-10.4460	-0.1555

		$k = 1$
$i = 2$	$j = 0$	-0.2050
	1	-0.7324
	2	-0.3449
	3	-1.3526
	4	1.6784

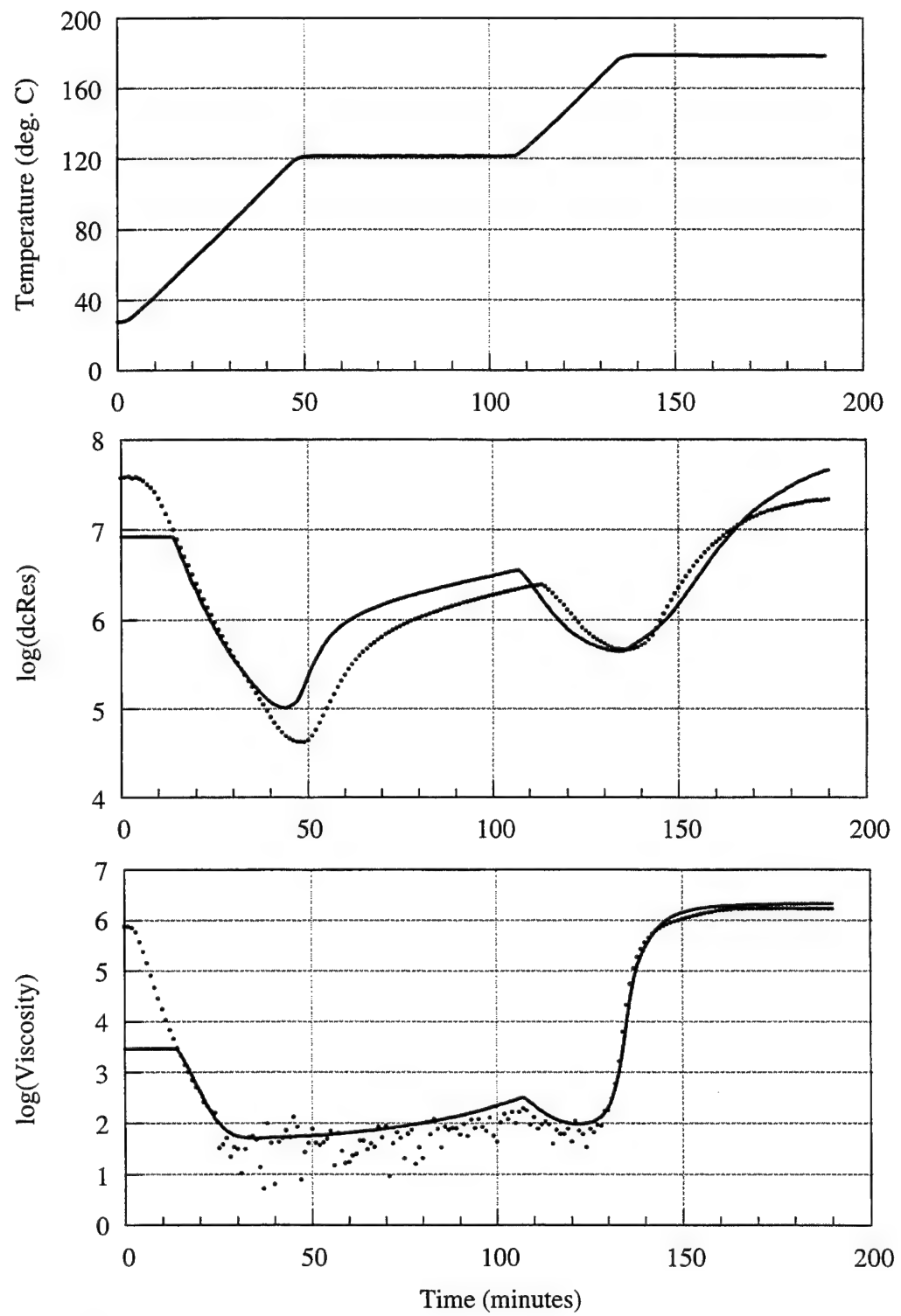


Figure 81. Verification of BNN Models for dc-Resistance and Viscosity.

low-viscosity region than do viscosity data. The dc-resistance data seem to suggest some advancement of the sample used. These data confirm again that the dc-resistance is a good representation of the viscosity of the resin undergoing cure.

3.1.4 On Neural Network Structure

In general one chooses the simplest network structure that yields acceptable results, and there are no set rules for choosing the network structure. Several different neural network structures were tested. The network performance was poor when a single hidden layer was used (2-3-1, 2-4-1, 2-5-1, and 2-10-1). In the case of two hidden layers (2-4-4-1, 2-5-3-1, 2-5-4-1, 2-5-5-1, and 2-30-15-1), the performance of the 2-5-4-1 structure yielded the best results. When a large number of neurons (30-15) in the hidden layers were used as suggested in the literature, the performance of the network degraded. A 2-30-15-1 network contains 570 weights compared to 43 for a 2-5-4-1 network. Considering the fact that only 654 examples were used for training the reaction rate model, it is not a reasonable choice.

For the dc-resistance and viscosity models, since they both use the same inputs (temperature and degree of cure), a test was made to see whether the two can be trained using a single network without changing the network structure. While the individually trained 2-5-4-1 networks performed well, a 2-5-4-2 network structure is not sufficient for an added output.

3.1.5 On Neural Network Training

Several tests were performed using reaction rate data to check whether fewer than four sets of training data could yield acceptable results. Of particular interest is to remove the DSC data from the very slow heating rate of 0.2°C/min. It was found that data from the slow heating rate are necessary for good prediction of reaction rates during temperature holds in a run, since the training set lacks data of true temperature holds. Eliminating data from either of the two intermediate heating rates (1 and 2°C/min) degrades the performance of the network. The highest heating rate used for training (5°C/min) sets the upper limit.

Several more tests were made in an attempt to further improve the neural network performance. These tests included using more training patterns, using lower/higher precision in the training data, using the logarithm of reaction rate, and adding one more hidden layer. None of these changes made any significant change to the outcome; in fact, in some cases the performance of the network degraded. In one test the network was trained without randomizing the input patterns. The resulting network performed poorly. It is important that the training patterns be randomized, so that they are not in any particular sequence in time or temperature.

Some issues regarding the accuracy of network models during long holds are being studied. As the current neural network models were trained with data using constant temperature ramp rates, there seems to be a lack of data for training the network model to predict behavior under long periods of isothermal holds. In general this is not a serious problem for a curing process which typically does not involve excessively long isothermal holds. Long isothermal holds, however, can be important for slow processes such as moisture absorption and desorption rates in the study of hygrothermal stability of polyimide composites.

3.1.6 Neural Network for Sensor/Process Modeling

Incorporating the neural network reaction kinetics and viscosity (using dc-resistance) models of 3501-6 into an existing one-dimensional heat transfer model is underway. The combined model will serve as a simulator for CPC control strategy development which will incorporate feed forward feature. How this information will be used by the CPC controller is also being considered.

It is also desirable to be able to use the monitored dc-resistance and temperature to determine the degree of cure of the resin. However, this cannot be done by simply training the network differently, as dc-resistance is not a one-to-one function of temperature and degree of cure.

Some initial attempts have been made to use the neural network for modeling transient behavior. The focus is on modeling equipment transient responses such as autoclave and press heating and cooling responses. It is hoped that equipment response can be quickly modeled by a neural network using existing CPC data from previous runs. For an autoclave the main focus will be on extracting heat transfer coefficient, while for a press the focus will be on the large thermal mass (which is also present for autoclave processing using tools with a large thermal mass).

SECTION 4

CARBON-CARBON AND CARBONACEOUS MATERIALS

4.1 CARBONIZATION OF PITCH AND OTHER PRECURSORS

Forty carbonization runs were made during this reporting period. They include full and partial carbonization cycles. A variety of materials were run including pitch resin, phenolic composites, natural materials such as wood, experimental high char yield resins, and University of Akron PAN and pitch fibers.

4.2 DAMAGE EVOLUTION IN CARBON-CARBON COMPOSITES

The structural application of two-dimensional carbon-carbon composites is currently very limited, due to a lack of understanding of failure mechanisms under mechanical loading. The fiber reinforcement in two-dimensional carbon-carbon composites is normally in fabric form, mostly in satin weave. Failure in woven composites, in general, occurs in the vicinity of yarn crimping (due to two perpendicular yarns crimping over and under to each other, Figure 82) where the stress is known to be three-dimensional [12]. Due to the presence of two perpendicular yarns crimping at the failure location, a difficulty exists in identifying experimentally the influence of the stress components on the failure of two-dimensional carbon-carbon composites.

In order to optimize the material properties and improve the performance of carbon-carbon composites, there is a need to understand the physics and identify the influence of stress components on the failure mechanism. A model carbon-carbon composite was fabricated to simulate the fabric yarn crimping only in one direction (in a plane) as shown in Figure 83. In the vicinity of the planar yarn crimping, the stress field is two-dimensional (except for edge effects). Thus the model composite, to some extent, simplified the process of understanding the influence of the stress components on the failure of the composite in the vicinity of the yarn crimping. For the convenience of defining the waviness in the model laminates, the ratio of the yarn (or lamina in this case) waviness amplitude, a , to the length of the wave, λ , is defined as the lamina waviness ratio. The objective of this work is to study the damage evolution and failure in the model laminates with a view toward using the data in understanding the failure mechanism in two-dimensional carbon-carbon composites.

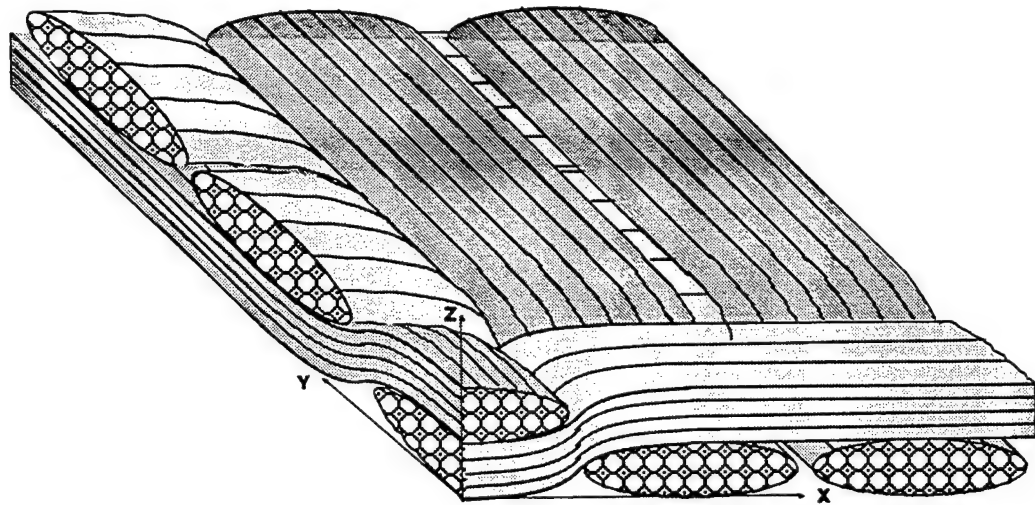


Figure 82. A Representative Volume Element (RVE) of Woven Fabric Composite.

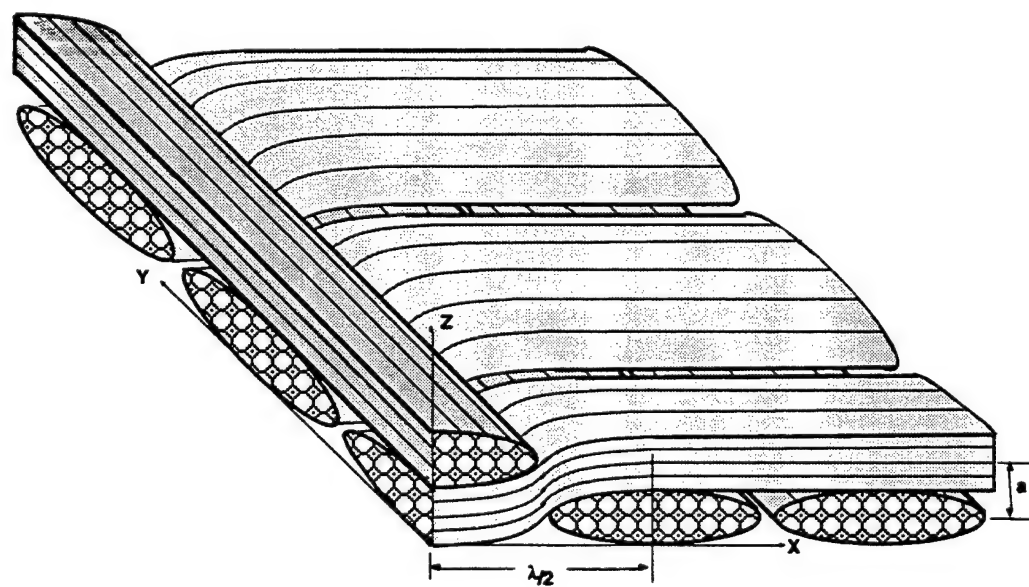


Figure 83. The Model Carbon-Carbon Composite with Simulated Planar (x-Plane) Yarn Crimping.

4.2.1 Processing of Model C-C Laminates

A unidirectional AS4/SC1008 phenolic prepreg was used as the precursor for the model laminates. The unidirectional prepreg was made by a wet-filament winding process. The prepreg was B-staged before being used for the laminate lay-up. Waviness in the composite laminates was produced by inserting narrow strips of the unidirectional prepreg perpendicular to the longitudinal direction of the laminates. The laminates were cured and carbonized at the Wright Laboratory Materials Directorate. The CVD densification of the laminates was performed at the BF Goodrich SuperTemp facility. The geometrical configuration of the model laminates was characterized by the lamination sequence away from the wavy region, lamination sequence at the midsection of the wavy region, and the lamina (yarn) waviness ratio. Consequently a new laminate notation was used for the model laminates to indicate these characteristics. For example, the notation used for the model laminate shown in Figure 84 was $([90_2/0_2]_S, [0_2/90_2]_S, 0.054)$, indicating the lamination sequence away from the wavy region, mid-section lamination sequence of the wavy region, and the lamina waviness ratio, respectively. In eight-harness satin (8HS) balanced carbon-carbon composites (made of 12k tow of 24 tows per inch), the yarn waviness ratio, a/λ , is found to be approximately 0.050. A cross-ply laminate, $[90_2/0_2]_S$, was also fabricated to use as a baseline laminate for data comparison purposes.

4.2.2 Experimental Procedure

The objective of the present work, as stated before, was to generate experimental data on damage development and failure in the model carbon-carbon laminates, which will later be correlated with stress analysis for assessing damage and developing failure criteria for two-dimensional carbon-carbon composites. Among the available damage detection techniques, e.g., acetate film replication, fluorescent dye resin impregnation, etc., the *in situ* microscopic observation of damage under load was found to be more promising than any other damage detection techniques. The specimens were tested in tension. In order to observe and record *in situ* damage development through a microscope, a portable load frame was used for this study. The description of the portable load frame and the *in situ* damage detection technique is described in Reference [3].

4.2.3 Laminate Stress-Strain Behavior

During testing of the specimens in the portable frame, all specimens failed in the vicinity of the grip area which was attributed to the excessive stress concentration at the grip section. Thus, to obtain reliable failure and strengths of the laminates, standard size specimens

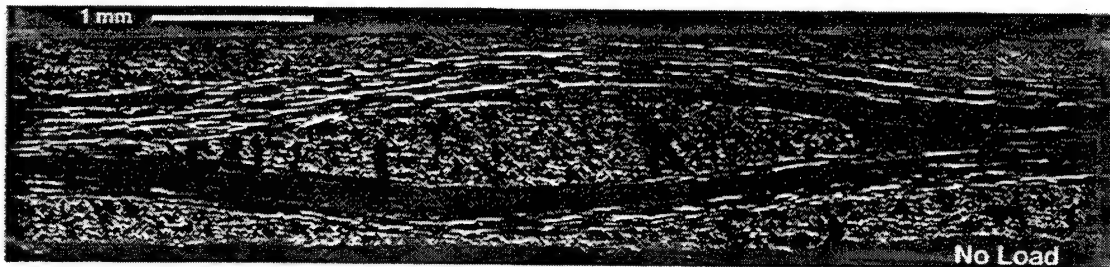


Figure 84. Cross-Sectional Micrograph of the Virgin ([90₂/0₂]_s, [0₂/90₂]_s, 0.054) Laminate.

(width of 19 mm and gage length of 101 mm) were tested in an MTS servo-hydraulic load frame. In order to correlate stress-strain curves with damage development, the specimens were loaded and unloaded several times to different strain levels. The representative stress-strain curves of the laminates are shown in Figures 85-87. Further, the average stress-strain behavior and the failure load of the laminates obtained from the portable load frame was found to be practically the same as that shown in Figures 85-87. The stiffness and strength data shown in these figures were the averages of three specimens tested for each laminate. The micrographs of the damage of the specimens shown were of the small specimens tested in the portable load frame.

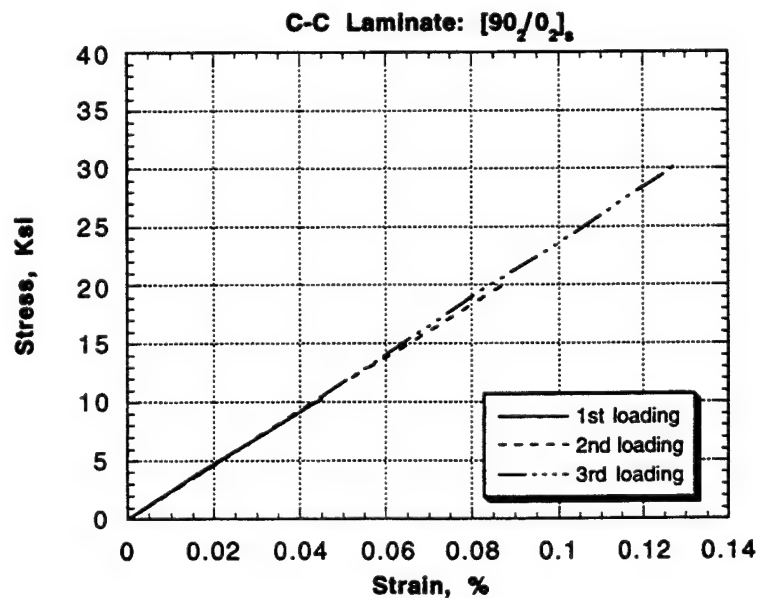


Figure 85. Stress-Strain Behavior of a Model Cross-Ply [90₂/0₂]_s Carbon-Carbon Laminate with Incremental Loading.

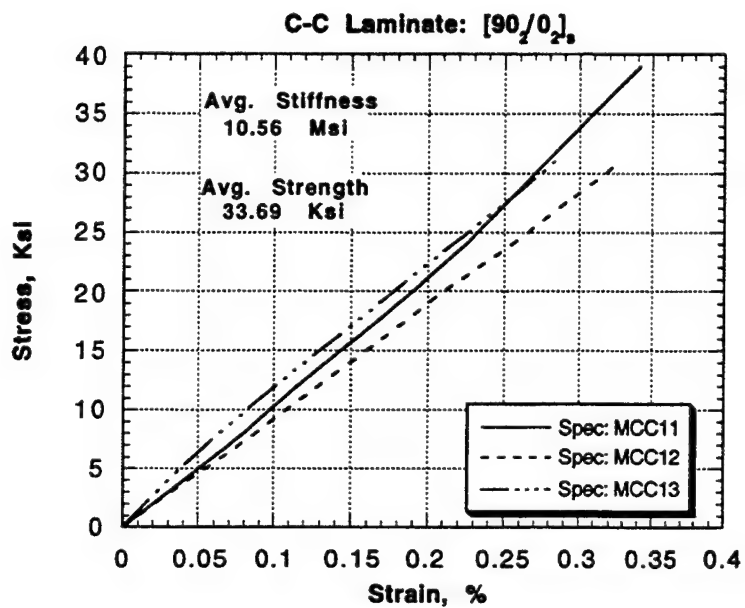


Figure 86. Stress-Strain Behavior of Three Specimens of a Model Cross-Ply [90₂/0₂]_s Carbon-Carbon Laminate.

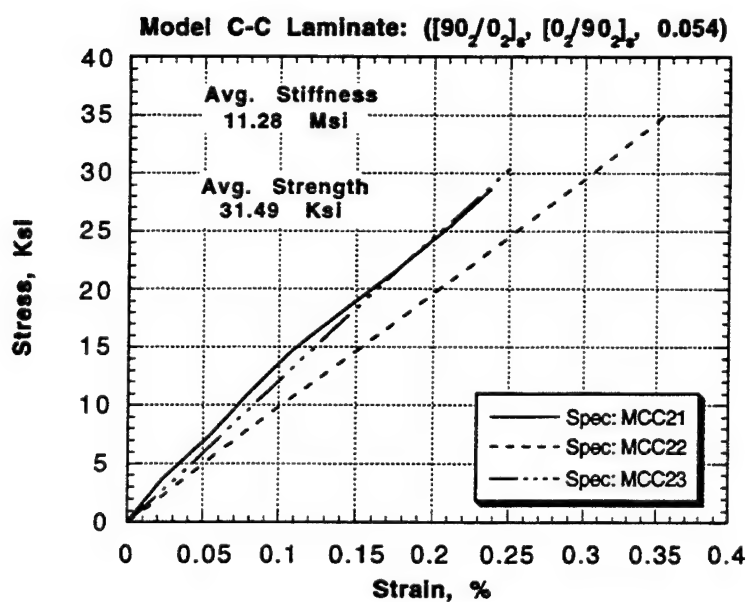


Figure 87. Stress-Strain Behavior of Three Specimens of the Model-([90₂/0₂]_s, [0₂/90₂]_s, 0.054) Carbon-Carbon Laminate.

4.2.4 Damage Observation

The *in situ* cross-sectional micrographs of the model laminate at different strain levels before failure are shown in Figures 88-90. Noticeable damage (besides process-induced cracks and voids) in the laminate appeared at a far-field tensile strain level of 0.162 percent (Figure 88) as an interface crack at the right end of the crimp area. With increased loading another interface crack developed at the left end of the crimp area at a far-field tensile strain of 0.195 percent (Figure 89). With further increasing load these two interface cracks grew and got connected and propagated away from the crimp area along the length of the laminate (Figure 90). The laminate failed at a strain level of 0.238 percent. The micrograph of the failed specimen is shown in Figure 91. In addition a representative extent of matrix damage at failure is shown in Figure 92. The failure micrographs of the specimen revealed that the interface crack practically separated the transverse insert in the crimped location, and the laminate finally failed near the middle of the crimp under tension. An analytical model to analyze the failure mechanism is being developed.

4.3 MEASUREMENT OF COMPOSITE THERMAL CONDUCTIVITY

The data acquisition system for thermal conductivity measurements has been installed and tested. A prototype program for shutter control and DMA data acquisition has been completed. The current program has a simple user interface and a simple data file structure. Program details will be modified when the test procedure is completely determined.

A data analysis method for determination of thermal diffusivity has been developed. A constant flux to the specimen will be used rather than the ASTM standard flash method. With a constant flux to one face of the specimen, the temperature change of the other face will become linear in time. From the slope (m) and the intercept (b) of this straight line, thermal diffusivity (α) can be calculated:

$$\alpha = \frac{L^2}{6} \frac{m}{(-b)},$$

where L is the thickness of the specimen. There is no need for data conversion from bit count to temperature, since only the ratio of slope to intercept is required, and the temperature coefficient of the thermocouple is nearly constant in the small temperature range of measurement. Figure 93 shows the results from an initial test. It can be seen that the data contain 60 Hz noise at 1 kHz sampling frequency. However, this noise does not present a problem because the analysis

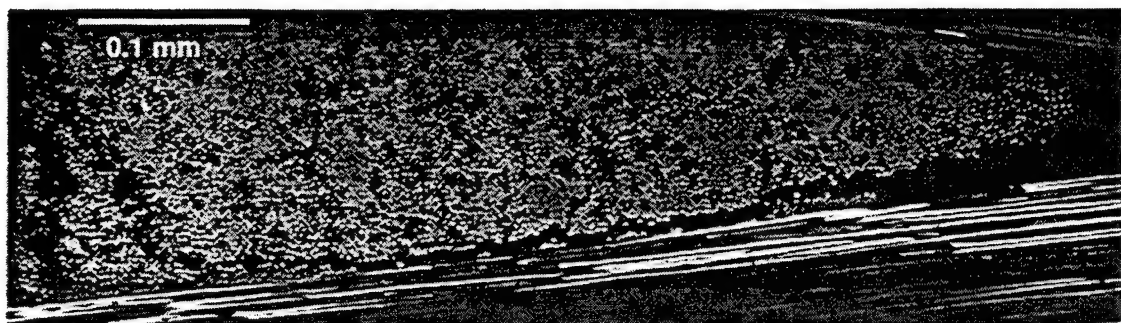


Figure 88. *In Situ* Cross-Sectional Micrograph of the $([90_2/0_2]_n, [0_2/90_2]_n, 0.054)$ Laminate at a Strain Level of 0.162 Percent.



Figure 89. *In Situ* Cross-Sectional Micrograph of the $([90_2/0_2]_n, [0_2/90_2]_n, 0.050)$ Laminate at a Strain Level of 0.195 Percent.

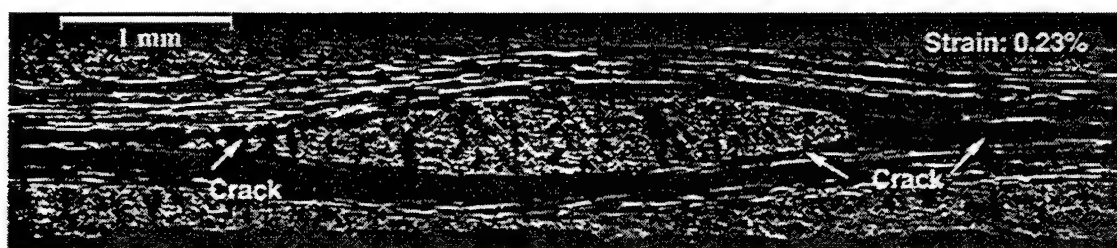
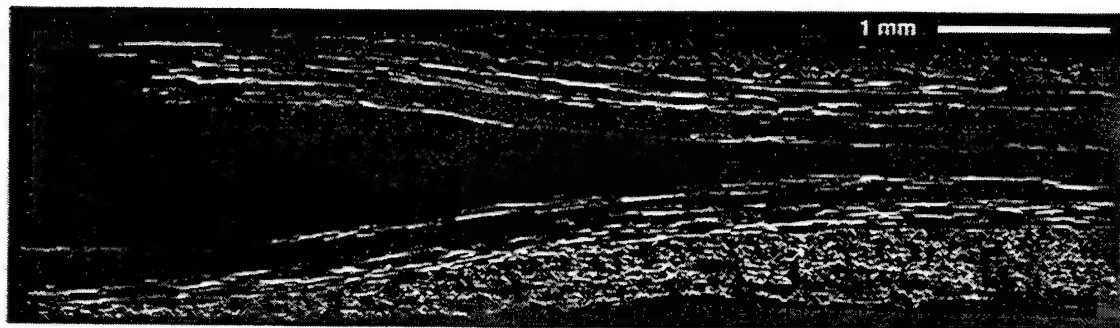


Figure 90. *In Situ* Cross-Sectional Micrograph of the $([90_2/0_2]_n, [0_2/90_2]_n, 0.050)$ Laminate at a Strain Level of 0.23 Percent.



(a)



(b)

Figure 91. (a) Micrograph of the Left Side of the $([90_2/0_2]_s, [0_2/90_2]_s, 0.054)$ Laminate After Failure; and (b) Micrograph of the Right Side of the $([90_2/0_2]_s, [0_2/90_2]_s, 0.054)$ Laminate After Failure. Failure occurred at a strain level of 0.238 percent on both sides.



Figure 92. Micrograph of the $([90_2/0_2]_s, [0_2/90_2]_s, 0.054)$ Laminate After Failure Indicating Extent of Matrix Damage.

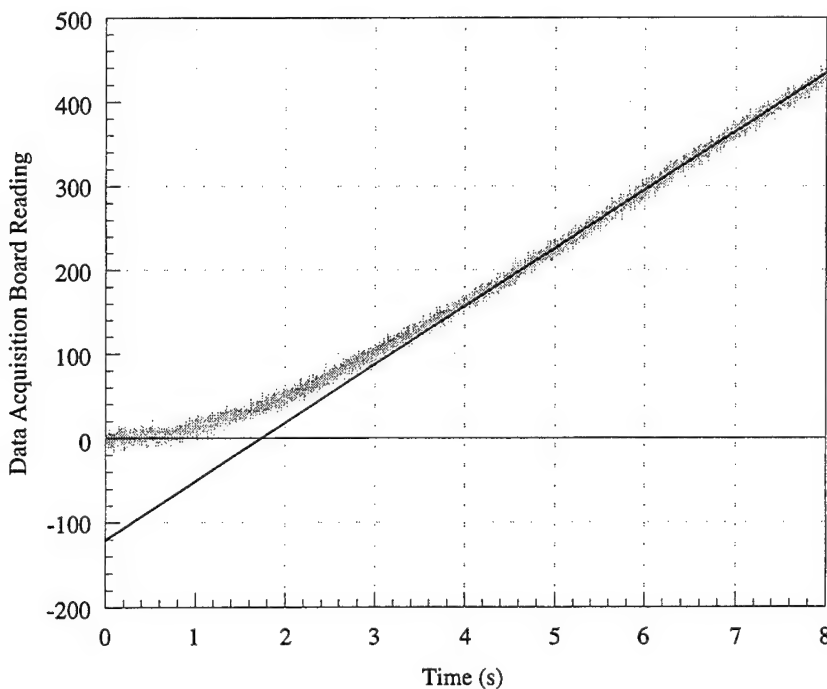


Figure 93. Temperature Change of Specimen in Terms of Data Acquisition Board Reading at 1 kHz. The straight line is least-squares fit of data from 5 to 8 sec.

method requires only the slope and the intercept which can be obtained by the least-squares method. The least-squares fit essentially filters out the 60 Hz sinusoidal line noise. The validity and accuracy of the setup and the analysis method will be verified by using samples of known thermal diffusivities.

The thermal conductivity of the sample can be determined after the density and the heat capacity are determined. It is possible to use this apparatus to obtain the product of the density and the heat capacity if the flux is known. The flux can be determined by using a second specimen of known thermal diffusivity with the same emissivity.

4.4 VAPOR-GROWN CARBON FIBERS

There were several series of vapor-grown carbon fibers analyzed by XRD for degree of crystallization and the presence of other crystalline forms. These series are described below and the results are also given in Tables 12-17.

The first analysis set consisted of six fiber samples that were "as-grown," "heat-treated," and "oxidized." As seen in Table 12 heat-treating Pyrograf IIITM fibers to 3100 and 3200°C had

TABLE 12
EFFECTS OF OXIDATION AND HEAT TREATMENT ON
PYROGRAF IIITM CRYSTALLINITY

Sample	$d_{(00,2)}$ (nm)	g_p	L_c (nm)
AN-169 HT 3200°C	0.3377	0.737	13.8
AN-201	0.3390	0.586	11.0
Oxidized 08/04/95	0.3388	0.606	11.4
Oxidized 08/24/95	0.3390	0.578	9.3
Fiber Produced 6/21/95	0.3415	0.287	3.8
HT 3100°C	0.3385	0.638	18.8

TABLE 13
CRYSTALLINITY OF "AS-MADE" AND HEAT-TREATED PYROGRAF-ITM SAMPLES

Sample #	Condition	$d_{(00,2)}$ (nm)	g_p	L_c (nm)
95	as made	0.3499	-0.682 ^a	3.4
	heat-treated	0.3360	0.925	42.1 ^b
96	as made	0.3501	-0.704	2.9
	heat-treated	0.3369	0.822	36.1
101	as made	0.3478	-0.439	3.1
	heat-treated	0.3362	0.902	26.6
107	as made	0.3494	-0.623	3.2
	heat-treated	0.3368	0.836	31.5
113	as made	0.3492	-0.599	2.8
	heat-treated	0.3365	0.871	71.7
116	as made	0.3495	-0.643	2.7
	heat-treated	0.3361	0.916	35.6
117	as made	0.3497	-0.664	3.9
	heat-treated	0.3362	0.906	43.7
136	as made	0.3491	-0.592	3.0
	heat-treated	0.3366	0.859	26.8

a - g_p values of less than one indicate a mixture of turbostratic and amorphous carbon not a true degree of graphitization.

b - L_c values greater than 30.0 nm are subject to large errors.

TABLE 14
FIRST PRODUCTION MONITORING OF PYROGRAF IIITM CRYSTALLINITY

Sample	$d_{(00,2)}$ (nm)	g_p	L_c (nm)	Other Phase
α -C1	0.3392	0.56	10.8	trace
C-D1	0.3388	0.60	13.9	trace
C1	0.3388	0.61	13.7	trace
C2	0.3383	0.66	12.5	some
C3	0.3379	0.71	10.6	trace

TABLE 15
REPRODUCIBILITY OF PYROGRAF IIITM CRYSTALLINITY

Sample	$d_{(00,2)}$ (nm)	g_p	L_c (nm)
F-S #1	0.3398	0.485	10.4
F-S #2	0.3392	0.557	11.2
F-S #3	0.3389	0.594	10.4
F-A, Hi #1	0.3403	0.429	8.7
F-A, Hi #2	0.3395	0.528	10.8
F-A, Hi #3	0.3399	0.482	8.5
F-A, Lo #1	0.3396	0.510	10.2
F-A, Lo #2	0.3390	0.576	10.2
F-A, Lo #3	0.3406	0.390	10.5
F-O #1	0.3399	0.472	8.3
F-O #2	0.3400	0.464	10.5
F-O #3	0.3390	0.581	11.3

TABLE 16
SECOND PRODUCTION MONITORING OF PYROGRAF IIITM CRYSTALLINITY

Sample	$d_{(00,2)}$ (nm)	g_p	L_c (nm)	a_{diamond} (nm)
ADNH-24/29	0.3429	0.124	4.1	
ADNH-176 (shot 51)	0.3389	0.595	9.7	0.3631
ADNH-176 (shot 52)	0.3398	0.484	8.1	0.3632
ADNH-86 control	0.3390	0.578	8.9	0.3636
ADNH-86 (shot 7)	0.3387	0.622	10.2	
ADNH-86 (shot 8)	0.3381	0.692	15.4	0.3603

$a_{\text{diamond}} = 0.35667$ nm accepted JCPDS value

TABLE 17
THIRD PRODUCTION MONITORING OF PYROGRAF IIITM CRYSTALLINITY

Sample	$d_{(00,2)}$ (nm)	g_p	L_c (nm)	a_{diamond} (nm)
ANC-27 (shots 10 & 11)	0.3392	0.558	7.6	
ANC-27 (shots 12 & 13)	CVD diamond is the main phase			0.3625

$a_{\text{diamond}} = 0.35667$ nm accepted JCPDS value

very little effect on the crystalline parameters; one sample had a slightly larger crystallite size and the other a slightly higher degree of graphitization but neither change was as significant as the changes observed for heat-treated Pyrograf ITM fibers. The results from the oxidized samples were also very typical of Pyrograf IIITM, and no degradation of the fibers is indicated. The small differences between the oxidized and the control samples are well within the previously observed measurement variability.

The effect of heat-treatment on Pyrograf ITM fibers was also examined. The results are shown in Table 13. For these fibers the "as-grown" state is a mixture of amorphous and turbostratic carbon which can be converted to graphite by heat treatment. Examination of the

data in Table 13 shows significantly greater degrees of graphitization and larger crystallite sizes for the heat-treated Pyrograf ITM versus the Pyrograf IIITM results.

The results for the second fiber set are given in Table 14. These fibers were from standard production runs. Little differences were noted within this set or between these results and other production runs.

One significant difference worth noting in these samples is the presence of an unknown phase (observed in other Pyrograf IIITM samples). All five samples had trace amounts of this other phase, but "C2" had significantly more than the other four samples. This other phase was still significantly less than the graphitic phase. The major peaks for this phase correspond to d-spacings of 0.435, 0.268, and 0.2515 nm.

The third fiber set consisted of four Pyrograf IIITM fiber samples with three replicates each. In Table 15 the consistency in the results from the replicates is good. All of these samples have degrees of graphitization and crystallite sizes typical of other Pyrograf IIITM samples.

All 12 samples showed evidence of another phase besides graphite with peaks about 20-21° and near 30° 2θ. This is the same minor phase observed in previous samples but never identified. The F-A, Lo and F-O samples also appeared to have more amorphous material than the F-S and F-A, Hi samples.

The fourth fiber set was a duplication of previous standard production runs which had produced diamond as a minor component. CVD diamond was indeed found in these fibers as shown in Table 16.

The fifth set of Pyrograf IIITM fibers were made partially from a coal feedstock. The first sample was fairly typical of the Pyrograf IIITM samples examined in the past (see Table 17). The second sample, however, was not; it consisted mostly of a CVD diamond phase with some iron oxide (also seen in many previous samples). The diamond phase appears to be dominant in the second sample. In fact this sample has the strongest diamond diffraction of any Pyrograf IIITM sample examined. See Figure 94 for the phase identification notation in these samples.

4.5 UPGRADE OF CARBONIZATION FACILITY

The carbonization furnace was upgraded to allow digital data acquisition and control. This was accomplished by the purchase and installation of an Aerospace Services and Controls composite processing controller which has the capability of 20 channels of thermocouple data

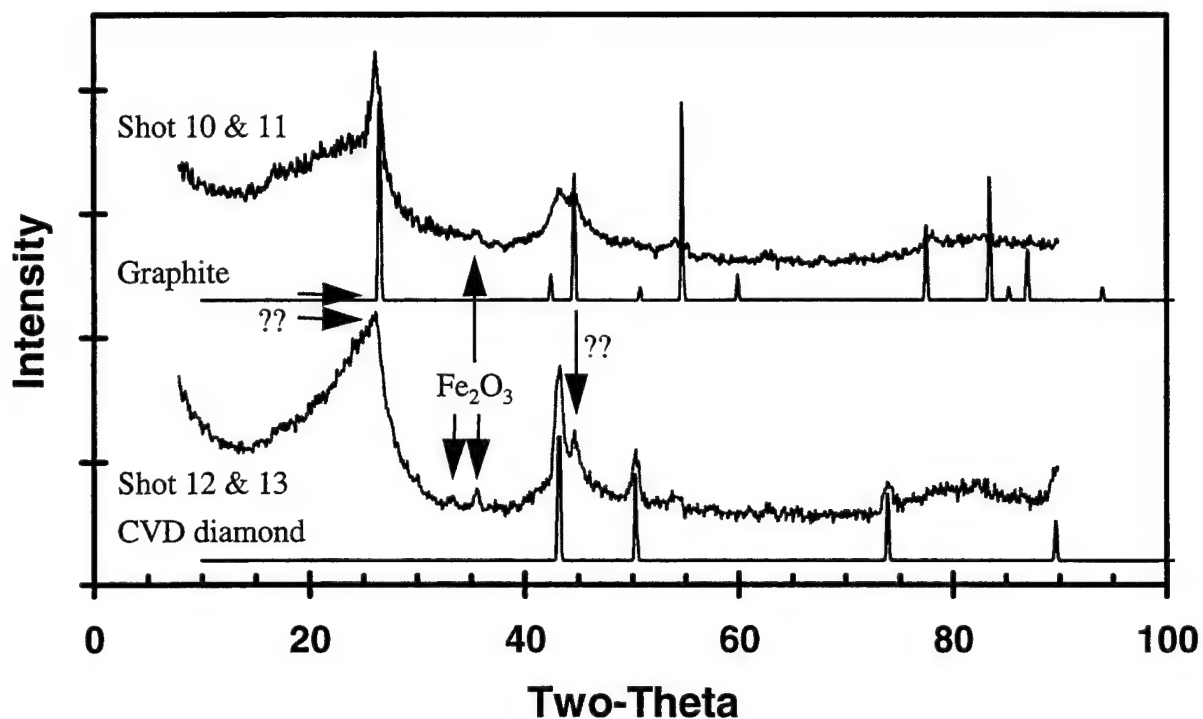


Figure 94. Phase Identification in the ANC-27 (Coal Precursor) Samples.

and 14 channels of analog inputs/outputs. The custom-designed software allows control of all parameters related to the operation of the carbonization furnace and monitoring of the incinerator. The data are digitally stored for later analysis or displayed in real-time for monitoring purposes. Since most runs are between 18 and 48 hours in duration, the system must perform the majority of its functions while unattended. The installation of the equipment will lead to better reliability and increase the safety of the facility.

4.6 INTELLIGENT PROCESSING OF CARBON-CARBON

The development of sensors for studying carbonization parameters is the current effort of this task. Numerous sensors have been looked into, with the decision being made to study them in the following order: (1) GC/MS, (2) FTIR, (3) resistivity, and (4) acoustic monitoring. During the current reporting period, GC/MS was investigated as a possible sensor for monitoring pitch resins during carbonization. Pitch resins give off volatiles when heated to 450°C. This temperature is used to partially carbonize the material to reduce bloating when the final product is made. There appears to be an optimum level of volatile release that makes the material not bloat while retaining processability. The goal is to study when this level is reached by determining what materials are released and monitor a few key components in the volatile stream

for decision-making. A Cahn TG-171 connected to a Hewlett-Packard 5890 GC and a 5971A mass spectrometer is being used in preliminary studies to set the chromatographic conditions. The current method involves sampling the gas stream once an hour, injecting a sample into the GC/MS at room temperature, and heating to 325°C in 20 minutes and holding there for 35 minutes. The injector temperature is 250°C, while the mass spectrometer transfer line is 325°C. A sample size of 20 μ L is used to perform this analysis. Once the analysis is complete, the instrument is cooled down using cold nitrogen gas to facilitate a quicker turnaround time. Results from the Cahn experiments showed some low molecular weight hydrocarbons, C1-C12, being evolved at temperatures lower than 450°C. Due to unforeseen transfer line problems, the higher molecular weight species are not being transferred in enough quantity for analysis. The transfer line needs to be heated to a much higher temperature. The current design needs slight modification, which is already underway, to accomplish the desired goal. Once the preliminary results are finished, the mass spectrometer will be transferred to the carbonization furnace and installed to do real-time monitoring of the actual process. The transfer system has been designed and partially installed on the furnace. This method shows promise to make this a viable sensor system to monitor off-gassing during carbonization.

4.7 INVESTIGATION OF SINTERED CARBON PROCESSING

The rapidly increasing number of potential applications for carbon products and carbon-carbon composites has found limited success due to material design complexities and the high cost of manufacture. Traditionally, these materials would be produced by repeated impregnation, carbonization, and graphitization or by chemical vapor infiltration of a fiber preform. This investigation focuses on the broadening of a technique originally referred to as binderless graphite and more recently called sintered carbon. The intent is to identify conditions and a process window in which fibers or precursor fibers may be compacted in a press mold and sintered to produce a high-density, self-reinforced carbon material in a single step (without the need for densification). This process should be much lower cost than any current processes due to the significant reduction in process time and complexity.

4.7.1 Background

Recent advances in isotropic graphite materials have identified methods of producing high-density, fine-grained graphite from micron-size particles of anisotropic (mesophase) pitch. Isotropic graphite blocks are produced by forming, baking, and graphitizing fine mesophase powders. Several commercial products have evolved to serve producers of industrial products such as EDM electrodes. They include powders such as "Kawasaki

Mesophase Fine Carbon Powder" (KMFC) where 1.9 Mg/m^3 density and 98 MPa bending strength are obtained. The powders are formed by cold isostatic or mold pressing under a pressure of 50 to 150 MPa. The carbonization rate was stated as being a function of the size and shape of the carbon block [13,14]. Strengths of 137 MPa (bending) and 372 MPa (compression) were reported for graphites produced from "Meso-Carbon Microbeads" from Osaka Gas using a molding pressure of 196 MPa [15].

Research publications related to the binderless mesophase powder process have only recently become available in the open literature. Rand and Stirling published work that illustrates the importance of the interparticulate bond and contrasts the process with solid-state sintering [16]. A variety of mesophase powders similar to the above products were characterized by El Horr, et al. [17]. Important work by Hoffman and Hutterer [18-21] demonstrated that a liquid phase sintering process takes place, modeled the complex time-temperature-viscosity relationships involved, and developed the thermoplasticity test. Mochida, et al. [22] utilized crushed pitch grains to illustrate the effect of oxygen stabilization of different anisotropic pitches to obtain optimum fusibility and volatile content for the sintering process.

In order to produce fiber composites by this process, we must first identify a wider process space for the pitch powder process and provide knowledge essential to the prediction of processing conditions for different types of pitch resin, as the resin source greatly affects its sinterability. The introduction of fibers results in greater complexity but is believed necessary to increase material strength and toughness. The use of thermally- or oxidatively-treated "green" fibers could be applied once a better understanding of the behavior is achieved. This would result in the microstructure of a "fibrous monolith," similar to those seen in research on toughening of ceramics.

The formation of flat panels by this process represents a much more sensitive test of the process than the production of cylinders or small billets as seen in the prior work. Cracks, bloating, and warpage are much more evident in the thin plates, but they better represent how a composite panel would be dimensioned. Fabrication success should be possible by oxidatively preparing the materials in such a manner that, although infusible, they will bond and coalesce during heat treatment. The heating rate should be maximized for efficient sintering but is limited by the transport of gaseous pyrolysis products to the surface. If the rate is too high, voids will be formed by the released gases. Too slow a rate will allow the pitch to carbonize before the viscosity drops enough for sintering to take place. Characterization of the pitch material is also crucial to application of this study to the use of pitches from various sources.

4.7.2 Experimental

4.7.2.1 Thermoplasticity Measurement

The thermoplasticity measurement is believed to be much more sensitive to the properties which allow sintering than any analytical technique based on measurement of chemical properties. Synthetic mesophase pitch (AR resin) was oxidized in air at 220°C for increasing times to produce specimens for the thermoplasticity test. The oxidized powder was shatterbox crushed and pressed into flat 20-mm disks at 5000 psi. A standard TMA vertical penetrator, equipped with a conical tip probe, was used with a 1 g load to perform the penetration test. The curves were normalized to remove the effect of sample thermal expansion and the unitless-scale labeled absolute penetration, in Figure 95, illustrates a significant change in onset temperature and penetration depth for the samples oxidized 30 to 150 minutes. The test was used to characterize the thermal oxidation condition of pitches used in sintering studies. Testing of compacted panels will help illustrate the effects of compaction conditions and lead to explanations for variations in behavior, due to the physical properties and condition of the compacted pitch powder.

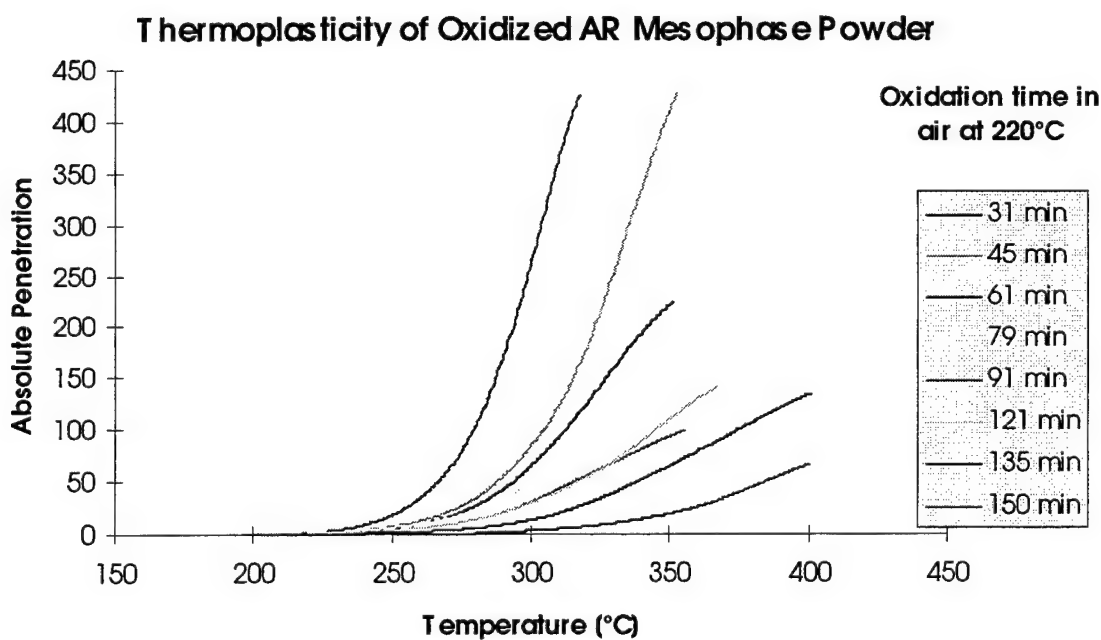


Figure 95. Thermoplasticity Measurement of Oxidized Pitch Resin.

4.7.2.2 Variation of Pressing Conditions

By varying the pressing conditions, the intent is to understand the range of possible conditions and determine if processing with fibers is practical. Statistical analysis of empirical data is being used to study the multidimensional interactions of the many processing variables within a defined range of processing conditions. A five-by-five hyper-Greco-Latin square was conceived with five levels of the five process variables in order to empirically determine correlations between fabrication success and the process variables of temperature, pressure, and time at pressure, for a range of powder sizes having different levels of oxidative weight gain. Considering particle size as an important variable, but lacking proper equipment to classify the jet-milled powders into discrete size distributions, the fifth variable of particle size was held constant. The range of pressing conditions was determined through evaluation of the dynamic mechanical behavior of the as-received AR resin and the predicted behavior of the oxidized powders. Oxidation weight gains of 2-10 percent, temperatures from ambient to 300°C, pressures of 300 to 15,000 psi, and 15- to 300-minute dwell times were selected and randomized to produce the test matrix shown in Table 18.

4.7.2.3 Milling of Resin

A Model 4 Micro-Jet fluid energy mill from Fluid Energy Aljet was used to pulverize the raw pitch pellets and further crush and mix the oxidized powders. Particle size distributions remained consistent for each successive jet-milling operation and are represented by the histogram plot of Figure 96. The very small average size of around 1.5 μm is much smaller and the distribution narrower than the powder obtained from the shatterbox crushing of earlier studies.

4.7.2.4 Oxidation Treatment

When the jet-milled powders were first utilized, unusual behavior was noted upon oxidation when compared to the crushed and sieved powders. The powder was observed to bond and form a hard crust more readily than the crushed powders and also formed the higher temperatures causing partial melting, increased bonding, and powder shrinkage. DSC was performed on the jet-milled powders in air and nitrogen to determine the maximum heating rate that may be used during initial oxidation without causing a significant temperature increase in the samples. Table 19 shows that 10°C per minute should be slow enough to prevent the exotherm. Reference to the importance of heating rate has been made in the literature [23], but it was not believed to have a large effect at the fairly low oxidation temperature of 220°C because

TABLE 18
HYPER-GRECO-LATIN SQUARE TEST MATRIX OF PRESSING CONDITIONS

Pressure (psi)						
% Wt. Gain						
Powder Batch		Temperature (°C)		3	4	5
		1	2			
A	15	25	75	150	225	300
	30	10000	1000	5000	15000	300
	60	6	2	8	10	4
	120	JM1DE	JM1F3A	JM4AB	JM2-AB	
	300	300	15000	1000	10000	5000
B	30	8	6	10	4	2
	60	JM1F3A	JM1DE	JM5EF6AB	JM2-AB	
	120	5000	10000	15000	300	1000
C	60	10	8	4	2	6
	120	JM4AB	JM1F3A	JM2-AB	JM6GH7ABCD	
	300	15000	5000	300	1000	10000
D	120	2	4	6	8	10
	300	JM2-AB	JM6GH7ABCD	JM1F3A	JM5EF6AB	
E	120	1000	300	10000	5000	15000
	300	4	10	2	6	8
		JM2-AB	JM5EF6AB	JM6GH7ABCD	JM6EF	

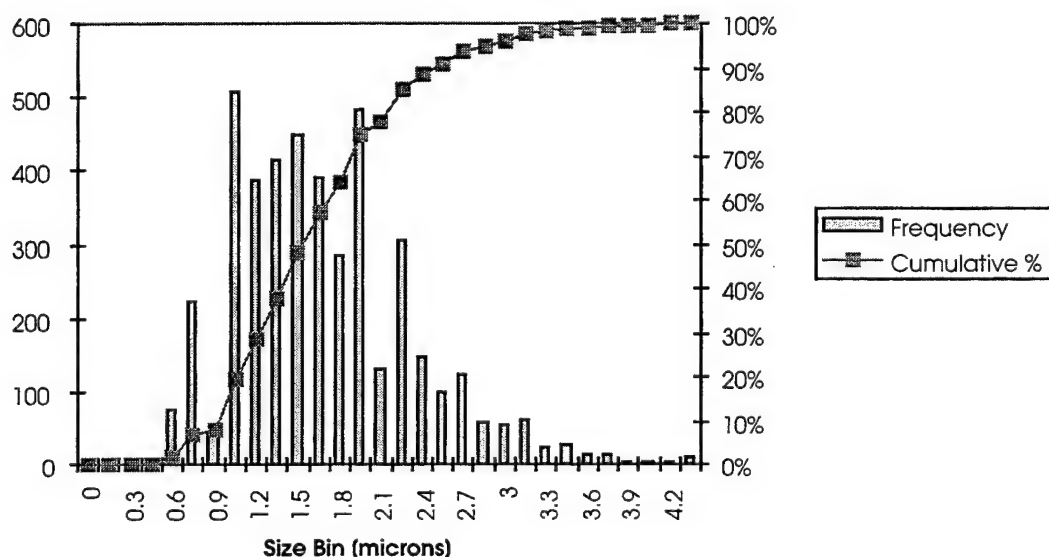


Figure 96. Representative Powder Size Distribution for Jet-Milled Pitch.

TABLE 19
EFFECT OF INCREASING RAMP RATES ON DEGREE OF EXOTHERM

DSC Data

Oxidation of Jet-Milled AR in Air at increasing ramp rates

Ramp 25°C to 400°C at 10, 20, 40, and 60°/min

Heating Rate °C/min	Exotherm Tmax °C	Onset temp °C	Heat of reaction cal/g
10	210		
20	228	208	9.46
40	242	220	7.74
60	253	227	13.70

high rates were used in a recent fiber study using stepwise oxidation with no melting [24]. The very small powder size, bed depth, presence of released gases, and decreased oxygen concentration are all believed to contribute to the rate of oxidation weight gain.

Oxidation in 8x10-in. aluminum baking pans with perforated aluminum foil covers was conducted using 50-g and 75-g batches of jet-milled AR powder. A convective air oven was programmed with a two-hour heat-up from room temperature to 220°C (1.6°/min) to minimize the exotherm, while still allowing comparison to isothermal oxidation studies, but a small temperature rise was observed as the raw pitch was initially heated. Powders which had been partially oxidized previously did not produce this exotherm. The high initial oxidation rate is due to the extremely high surface area and high diffusion rate for oxygen in the raw pitch. The diffusion rate for oxygen is believed to drop after surface oxidation occurs and the oxygen concentration decreases. Figure 97 shows that Fickian diffusion becomes the limiting rate relationship for oxidation weight gain for raw AR resin after an initial rapid weight gain. The high initial rate is believed to be reaction rate controlled but is also affected in this case by the short exothermic temperature rise. Use of a packed or fluidized bed of powder is recommended for oxidation studies in which any detailed chemical or kinetic information is to be obtained. The rate and temperature of the flowing air may be much more carefully controlled than for the static powder bed of this study.

The 50-g and 75-g oxidized batches were combined and jet-milled before pressing. Batches were combined according to weight gain to obtain mixtures averaging approximately 4, 6, 8, and 10 percent weight gain, as listed in Table 20.

Arrhenius Plot of Pitch Oxidation

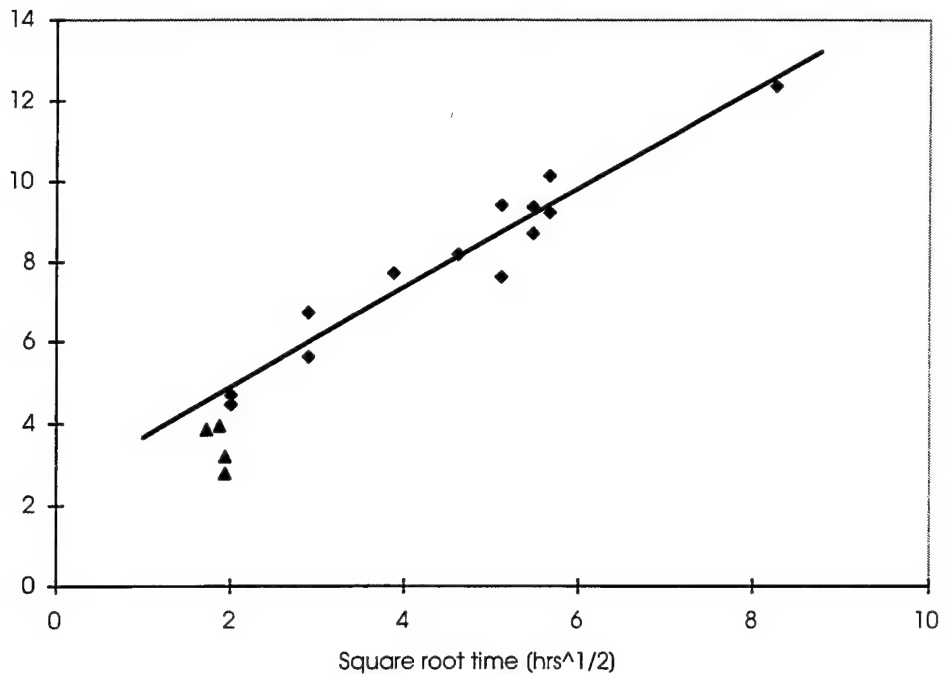


Figure 97. Percent Oxidation Weight Gain for Jet-Milled AR Resin.

TABLE 20
MIXING OF PAN OXIDIZED PITCH BATCHES

Mixed Batches	Mass (g)	% Wt. Gain	Mixed Batches	Mass (g)	% Wt. Gain
JM2-AB	151	4.0	JM5-E	89	9.8
JM1-E	53	5.6	JM5-F	86	11.2
JM1-D	53	6.7	JM6-A	84	11.7
JM1-DE	106	6.2	JM6-B	83	10.7
JM1-F	53	7.7	JM5EF6AB	342	10.8
JM3-A	54	8.2	JM6-E	82	8.8
JM1F3A	107	7.9	JM6-F	82	8.7
JM4-A	55	9.2	JM6-EF	163	8.7
JM4-B	55	10.1	JM6-G	82	8.7
JM4-AB	110	9.7	JM6-H	81	8.4
JM7-A	53	5.6	JM7-A	53	5.6
JM7-B	52	4.0	JM7-B	52	4.0
JM7-C	52	4.0	JM7-C	53	5.2
JM7-D	53	5.2	JM6GH7ABCD	372	6.4

4.7.2.5 Pressing of Panels

The mold used for sample pressing was designed to maintain a tight tolerance at high pressures while allowing forced die removal and sample temperature measurement. A 2x6-in. mold with square corners and one inch of die travel was constructed and is shown in Figure 98. The mold surfaces were treated with Frekote (44NC) silicone release interface prior to use and as needed during service to aid in sample removal after pressing.

Mold filling was performed by hand using 25 g of oxidized and jet-milled pitch. The material was smoothed and leveled in the mold using a spatula. For conditions above ambient temperature, the press was preheated before loading the mold, then the mold temperature was monitored and pressure applied as the temperature began to equilibrate. This heatup time before pressing ranged from 30 minutes to one hour depending on the setpoint and press type with most panels being pressed after 40 minutes of heat-up. The mold temperature was observed to lag the platen temperature at pressing time by up to 10°C, but the temperature equilibrated more quickly after pressure was applied. One significant difference in pressing conditions was due to the use of two different presses; a 300-ton press was used for the 10 ksi and 15 ksi conditions, and a 30-ton press was used for the 300, 1000, and 5000 psi conditions. The only difference was in the minimum contact pressure of the two presses; the minimum contact pressure is the lowest available force the press will apply when closed. For the large press this value is 2.3 tons, which exerts significant pressure on the mold as it is first placed in the press before it begins to heat up.

Removal of samples from the mold resulted in cracking of some specimens. This resulted from a combination of weakly compacted samples and inconsistent removal procedures. Crushing sounds were often heard when the pitch plaque just comes out of the die while pressing the sample out of the mold. This seems to cause cracking of the more firmly compacted samples, while the weakly compacted samples are damaged more in handling. Firmly compacted specimens often had smooth gray to shiny surfaces, while the weakly compacted ones were flat black. The cracked and/or shiny conditions after compaction are noted in column 7 and 8 of Table 21. Dimensions of the plaques were documented, before and after the sintering/carbonization step, to reveal the amount and uniformity of shrinkage, the degree of which is listed in Table 21, columns 9-12, based on a subjective scale of 0-3. Photographs of panel C2 before and after carbonization are shown in Figures 99a and 99b, illustrating a well-formed panel with good sintering properties. Panel C1 (Figures 99c and 99d) illustrates good compaction in Figure 99c, but partial bloating during sintering, which creates porosity, warpage, and cracking of the plaque in Figure 99d.

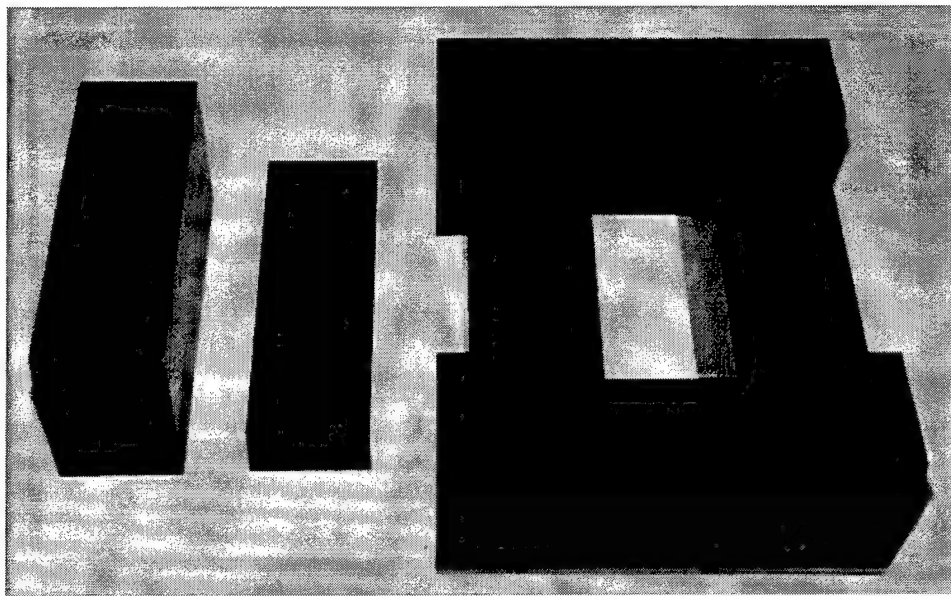
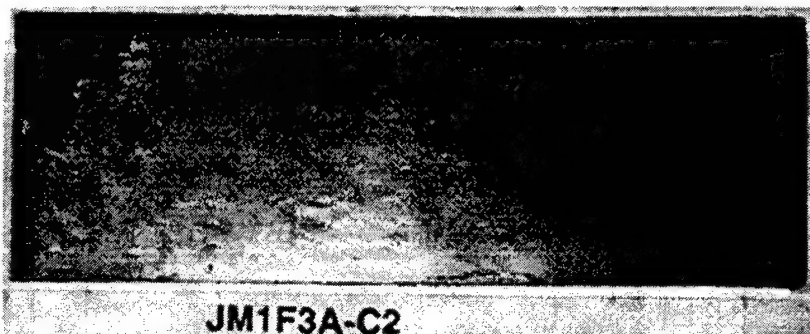


Figure 98. Photograph of 2"x6" Hot Press Mold.

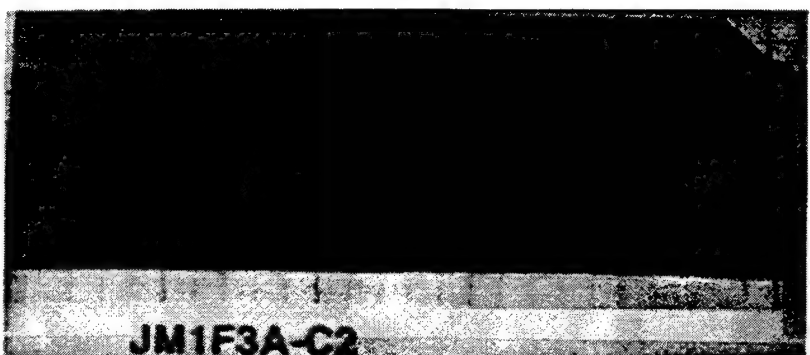
TABLE 21

PITCH SINTERING PRESSING CONDITIONS AND PROCESSING SUCCESS

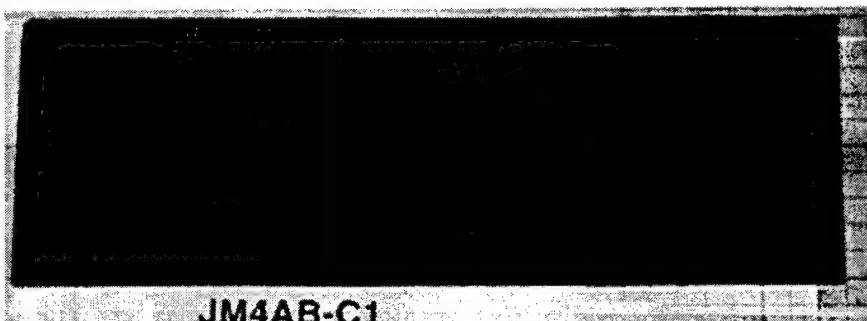
Pressing Data							Carbonization Data					
Panel ID	Intended Conditions	Prep	Compaction	Result	Sintering							
		Cond	Oxidat	Temp	Pressure	Time	Crack	Shiny	Bloating	Warpag	Cracks	Spalling
		(%)	(°C)	(psi)		(min)						
JM1DE-A1	A1	6	25	10000	15	0	1	1	1	0	1	0
	A2	2	75	1000	15				3			
JM1F3A-A3	A3	8	150	5000	15	0	0					
JM4AB-A4	A4	10	225	15000	15	1	0	2	1	2	2	2
JM2AB-A5	A5	4	300	300	15			3				
JM1F3A-B1	B1	8	25	300	30	1	0	0	0	0	0	0
JM1DE-B2	B2	6	75	15000	30	0	0	0	0	0	0	0
JM5EF6AB-B3	B3	10	150	1000	30	0	0	0	0	0	0	0
JM2AB-B4	B4	4	225	10000	30	0	0	3				
	B5	2	300	5000	30			3				
JM4AB-C1	C1	10	25	5000	60	0	0	1	2	1	0	
JM1F3A-C2	C2	8	75	10000	60	0	1	0	0	0	0	
JM2AB-C3	C3	4	150	15000	60	0	0	3				
	C4	2	225	300	60			3				
JM1DE-C5	C5	6	300	1000	60	1	1	0	0	0	0	
	D1	2	25	15000	120			3				
JM2AB-D2	D2	4	75	5000	120	0	0	3				
JM6GH7ABCD-D3	D3	6	150	300	120	0	0	0	1	2	0	
JM1F3A-D4	D4	8	225	1000	120	1	0	0	0	0	0	
JM5EF6AB-D5	D5	10	300	10000	120	1	1	0	0	1	2	
JM2AB-E1	E1	4	25	1000	240	0	0	3				
JM5EF6AB-E2	E2	10	75	300	240	1	0	0	0	0	0	
	E3	2	150	10000	240			3				
JM6GH7ABCD-E4	E4	6	225	5000	240	0	0	0	1	1	0	
JM6EF-E5	E5	8	300	15000	240	1	0	0	1	2	1	



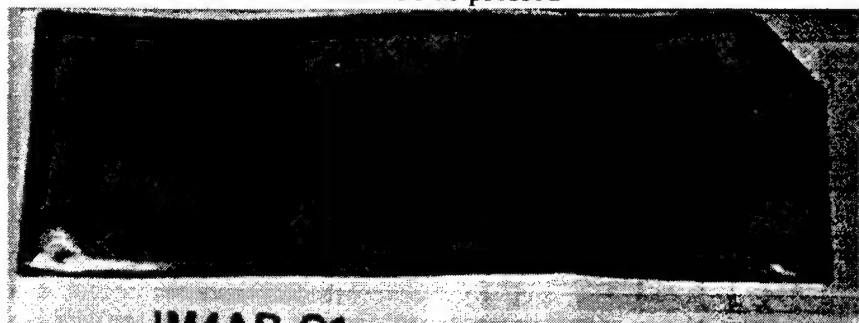
a. Panel C2 as pressed



b. Panel C2 sintered



c. Panel C1 as pressed



d. Panel C1 sintered

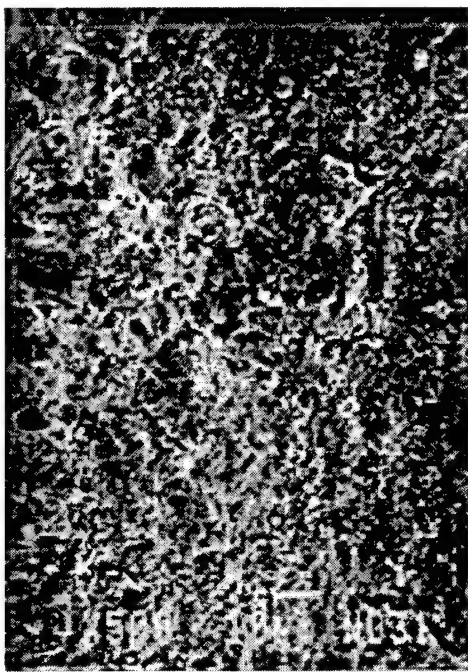
Figure 99. Whole Panels in the Compacted and Sintered Conditions.

Qualitative assessment of compaction and sintering behavior is displayed in Table 21. The relative values for bloating, warpage, cracking, and spalling range from 0 to 3. Panels which completely bloated could have no other values. The assessment of panels C1 and C2 may be compared with the images in Figure 99.

4.7.2.6 Microstructural Analysis

Particle bonding and sintering has been observed by scanning electron microscopy for both the as-pressed (compacted) and carbonized (sintered) conditions. The wide range of processing conditions that was utilized resulted in a large variation in sample microstructures. Samples were observed in the compacted and sintered conditions while considering the relative change in particle bonding and coalescence. In the compacted samples, relative degrees of packing were noted for different compaction pressures. When the particles were oxidized enough so that they did not bond, partial bonding was observed to occur between particles under some oxidation conditions. Complete consolidation (i.e., melting) was noted for samples having low oxidation levels.

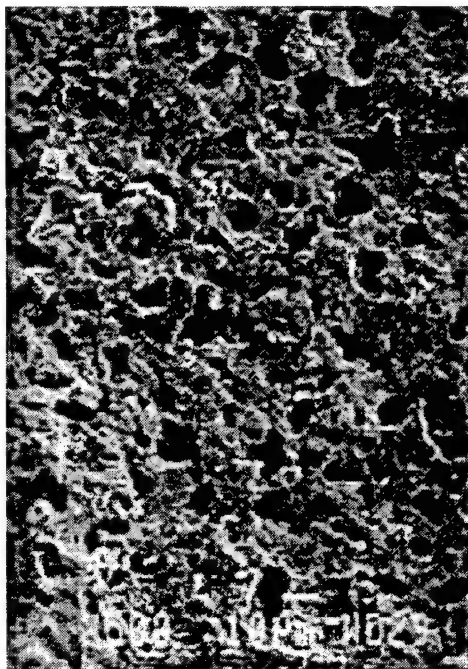
Full consolidation during compaction is the only case determined to be undesirable at this point; open porosity is believed necessary to provide a route for the escape of gaseous pyrolysis products during subsequent reaction sintering. In the observation of the sintered material, consideration was made for the change in particle bonding between the compacted and sintered states. Figure 100 illustrates this as the partial melting and formation of porosity may be observed in the carbonized (sintered) condition. A large fraction of porosity was noted in some of the best specimens, believed to be due to the segregation of pyrolysis products that were trapped in the material due to a lack of sufficient open porosity. The presence of large pores is much less desirable than the uniform small pores observed in the best panels. The formation of large voids was often visible on the surface and even resulted in nonuniform shrinkage, as in the photo of sintered panel C1 (Figure 99d). The porosity in some cases may simply be the result of poor sinterability and therefore could be improved through better understanding of the reaction sintering process. The porosity is currently being documented through image analysis, so that comparisons can be made based on relative amounts of open vs. closed porosity, and correlations can be made between oxidation and pressing conditions and compacted vs. sintered porosity. The lack of strength or porosity data for more than half of the original test matrix conditions, due to panel bloating upon carbonization, has resulted in much difficulty in making any correlations in the statistical analysis of the data. As more data are obtained, additional correlations may be made.



a. Panel E4 as pressed.



b. Panel E4 as pressed.



c. Panel E4 sintered.



d. Panel E4 sintered.

Figure 100. Fracture Surface SEM Images of Panel E4 which was Oxidized to 6% and Pressed at 5000 psi and 225°C for 240 min. No large-scale bloating was observed.

4.7.2.7 Thermoplasticity Testing of Compacted Panels

Thermoplasticity testing of compacted specimens has resulted in bloating and/or cracking of the specimen under the probe that correlated well with what happened to samples during sintering. The higher ramp rate of 10°C per minute significantly increased the chances for gasses to be trapped in the material, resulting in void formation within the sample, causing a dimensional change and a large expansion when the probe is actually penetrating the surface. The data obtained up to the point of bloating will be useful as well as the data obtained from the uniform pressing of oxidized powders as shown in Figure 95. Initial results are not presented here, as the testing is still underway.

4.7.2.8 Mechanical Testing Results

Coupons from the sintered panels for flexure testing were machined with 0.35-in. widths so that up to six coupons could be obtained from whole 2x6-in. panels. Four-point bend testing was performed using appropriate span-to-depth ratios for each panel, because they had slightly varied thicknesses (Table 22). Modulus is reported for specimens which were strain gaged during testing. Very large amounts of scatter for some specimens were due to cracks and/or pores in the specimens which resulted in lower strengths. The large potential error this presents reduces the chances of making correlations between processing conditions and mechanical properties. Demonstration of success in production of panels and the mapping of the processing space is the main objective of this study, so lack of data for optimization of strength is not a major concern at this stage. The matrix properties, although low, will be quite adequate in composites with the addition of fibers.

4.7.3 Summary

This investigation of processing conditions for sintered carbon has confirmed the assertion that preparation by thermal oxidative stabilization is the most important factor in the production of sintered carbon bodies. Oxidation levels of six percent or more are required to prevent bloating for this particular pitch resin. Effects of pressing conditions are being evaluated, but additional data will be required to make specific correlations and/or conclusions. Observation of pressed and sintered microstructures resulted in an understanding of the wide variation of possible conditions. The potential benefits of using elevated temperature pressing in the adaptation of this process to complex and net-shape products, as well as to the addition of reinforcing fibers, have been confirmed by the observation of interparticulate bonding during compaction. The extreme difficulty in handling of weak compacted panels and the low

TABLE 22
PITCH SINTERING PHYSICAL AND MECHANICAL DATA RESULTS

Cond #	% Char Yield	Average Dimensional Changes			Flex Strength (psi)	Standard Deviation (psi)	Flex Modulus (msi)
		Length	Width	Thickness			
A1	82.43	0.88	0.87	0.94	4421	2649	
A2							
A3							
A4	83.18	0.85	0.88	1.09	3428	1848	
A5							
B1	77.04	0.83	0.84	0.86	1435	869	
B2	82.52	0.88	0.84	0.97	4142	622	
B3	77.04	0.83	0.86	0.86	1515	834	0.64
B4							
B5							
C1	83.51	0.85	0.86	0.99	4789	2696	
C2	77.07	0.85	0.85	0.87	8137	30	2.43
C3							
C4							
C5	83.78	0.87	0.87	0.94	6895	2006	1.47
D1							
D2							
D3	82.24	0.59	0.88	0.87			
D4	77.48	0.85	0.85	0.73	2364	663	
D5	78.91	0.86	0.87	0.88			
E1							
E2	76.84	0.00	0.00	0.85			
E3							
E4	82.78	0.86	0.87	0.89	4808	1354	2.18
E5	79.87	0.88	0.87	0.84			

average strength indicate the importance of introducing reinforcement to the process as soon as possible.

4.8 STABILIZATION OF PITCH

A new research topic was the investigation of the concept of using some materials other than air or oxygen to stabilize pitch for a carbon-carbon composite. The current method of air stabilization is a time-intensive procedure, which is a balance between the oxygen penetrating into the pitch and reacting with the pitch. As the pitch reacts with oxygen to gain stability, the ability of oxygen to pass through the pitch becomes significantly limited, making additional stabilization more difficult.

A literature search for internal oxidants of pitch did not reveal any chemical species that were used by previous workers, other than air and oxygen and nitric acid. The literature for pitch oxidation consisted mostly of penetration times and depths for air stabilization or the oxidation of surfaces for adhesive purposes (nitric acid). Most of the literature also dealt with fiber production rather than carbon-carbon composites, no doubt because the latter is either company-confidential or restricted data.

The two primary methods considered feasible for stabilizing pitch are the incorporation of a stabilizing chemical prior to processing and partially stabilizing the pitch before processing.

4.8.1 Solvent Methods to Infiltrate Pitch

The first question addressed in the investigation of adding stabilizers to pitch was the method of introducing the stabilizer. The stabilizing chemicals need to be homogeneously mixed with pitch prior to processing. Any solid additive, high-viscosity liquid, or low-volume liquid cannot be melt processed with the pitch to disperse the additive without the desired stabilization reaction occurring during the mixing phase rather than in the later composite processing stage.

The idea of solution or slurry mixing of components with the pitch was therefore investigated. A successful solvent should ideally be one that dissolves or swells the pitch while also dissolving the additive. It should have a relatively low boiling point, so that the solvent can be easily removed before additional processing.

Several solvents were examined using a Soxhlet extractor with pitch. Both Mitsubishi AR and Ashland A-240 pitches were examined. The solvents tested were: toluene, dimethyl sulfoxide (DMSO), tetrahydrofuran (THF), and N-methylpyrrolidone (NMP). The hot solvent in this equipment drains onto the pitch and is siphoned off to be re-evaporated back to the pitch. Weight loss from the pitch in the extractor is the amount of pitch dissolved by the solvent. Extractions were performed for 24 hours each. By the end of the extraction, the siphoned solvents were mostly clear.

The DMSO solvent was the worst solvent tested; almost no pitch was extracted. The NMP extracted a fair portion of the pitches with the assumption that other nitrogen-containing aromatics such as pyridine would work in a like manner. In these and all solvents, the A-240 was extracted more (almost completely dissolved) than the AR pitch. This result was not unexpected. NMP, pyridine, and similar compounds have severe environmental and health problems which made them undesirable, and they were not examined further. Toluene extracted

90+ percent of the A-240 and would be a usable solvent for that pitch, but it did not extract very much of the AR which was the pitch of real interest. Other aromatic hydrocarbons such as xylene, benzene, etc. are expected to yield similar results. The THF solvent extracted 65 percent of the AR pitch.

The question of whether THF could successfully swell a pitch sample and thereby act as a carrying agent for internal oxidants was tested. A solid AR pitch plaque 1 mm thick was boiled in THF which contained a small amount of sodium chloride. After the outside of the plaque was cleaned with water, it was broken in half and examined by XPS in an SEM. Chloride atoms were found 100 μm from the edge, indicating at least some of the salt was carried by the THF into the pitch plaque.

The high degree of extraction by the THF solvent, its ability to penetrate pitch, its low boiling point of 67°C, and ready availability made this the solvent of choice for later experiments.

4.8.2 Pitch Sample Preparation

Several methods of sample preparation were examined. These preparations were primarily designed to produce neat resin samples to test the ability of a treatment to stabilize the pitch. This work was originally planned as an extension of the press sintering of neat pitch project (see Section 4.7). While this work could be extended to the Ashland A-240 pitch, it was usually carried out on the Mitsubishi AR pitch.

The first method of sample preparation was to melt press a pitch plaque. A variety of methods were attempted to produce a low void, even thickness, solid plaque. In all cases when air was not excluded, the pitch would not melt together. Heated in an oven, even under some pressure, the crushed pitch powder or pellets did not form a low-void plaque. This was true even when the oven temperature was over 100°C above the melt temperature of the pitch. Pressing the AR pitch between platens at 300 to 320°C proved to be the most effective method of producing good quality plaques. This latter method was the one used to fabricate the samples referred to as "plaques" below. To exclude oxygen, the top and bottom plates and the sample were placed in a stainless-steel bag that was flushed with nitrogen from a gas cylinder.

Pellets of pitch were pressed at ambient temperature and 20,000 psig on the small Carver press. Starting with ~2 g of pitch, a 1-in. diameter cylindrical pellet 2-3 mm thick was produced. Two possible methods of stabilization were examined: adding the stabilizing agent to

the pitch before pressing into a pellet (the “powder” method) and the addition of the stabilizing agent to the pellet after it had been pressed (the “pellets” method listed below).

Composite samples of AR pitch and a plain-weave T-300 cloth were also produced. The pitch was placed between two layers of the cloth and melt pressed together like the neat pitch plaques above.

4.8.3 Stabilization Results for Pitch Samples

A standard carbonization cycle was used to test the ability of the stabilizer. The samples were placed in the carbonization furnace and purged with nitrogen overnight. The furnace was then heated from ambient to a furnace temperature of 900°C at 2°C/min. and then allowed to cool naturally. This method generally heated the nitrogen and presumably the samples to 850°C and held that temperature for several hours.

4.8.3.1 Pitch Samples

A variety of additives were incorporated into pitch samples. The types of additives were peroxides (to release oxygen into the pitch during processing), polymer or polymerizable materials (to hold the pitch stable while carbonizing), and oxygen-containing compounds (to react with the pitch during processing). The polymer materials had the added variable of heating in an oven to cure the polymer: each piece was broken into two pieces, one was cured and the other carbonized without curing. In addition nitric acid was used to treat the pitch in an attempt to stabilize it.

The peroxides tested included tert-butyl peroxide, dicumyl peroxide, and cumyl hydrogen peroxide. The polymeric materials included a phenolic (SC1008), furfuryl alcohol (with five percent NaOH catalyst), and furfuryl aldehyde (with five percent para-toluene sulfonic acid catalyst). The other oxygen-containing compounds were para-benzoquinone, hexamethylene disilazane, and maleic anhydride. The nitric acid treatment consisted of boiling the sample in concentrated nitric acid for two hours and then neutralizing the acid in sodium bicarbonate and drying.

The “powder” method consisted of treating jet-milled pitch (1- to 2-mm particle diameter) with the additive mixed in THF. The THF was allowed to evaporate overnight in a hood and then the powder compacted into pellets as described in the preceding section. These pellets were then carbonized. The “pellet” method consisted of compacting the raw jet-milled pitch, as given above, and then infiltrating the pellet with THF containing the desired

additive. After evaporation of the solvent, the pellets were carbonized. The “plaque” method was very similar in that the melt pressed pitch was infiltrated with THF with the additive before carbonization.

The levels of additives tested ranged from 10 to 40 percent. The level of additive could be controlled best by dissolving the material in THF and adding to the pitch powder. Addition of material to pellets and plaques usually resulted in a significant loss of material which was left in the beaker holding the pitch pellet or plaque. The amount of stabilization in nitric acid was also less controllable: the only control being the amount of time the pitch was in the acid.

The results of these treatments, levels of treatment, and infiltration methods were very disappointing, as the only sample which did not bloat was the nitric acid treatment of the pitch powder. All the other treatments and preparation methods produced porous blobs. Most of the experiments used the AR pitch, but some also used the isotropic A-240 pitch with the same disappointing results. This can be seen in Figure 101. Figure 101a is a picture of part of a pellet made from nitric acid treated powder; note the smooth circular bottom edge and well defined broken edge on top. Figure 101b shows a typical bloated pellet. The size of the pellet has expanded (note the different scales at the bottom) and the pellet has lost all of its shape definition during carbonization due to the lack of stabilization. Some pellets retained part of their shape, indicating partial stabilization, but they were still largely expanded.

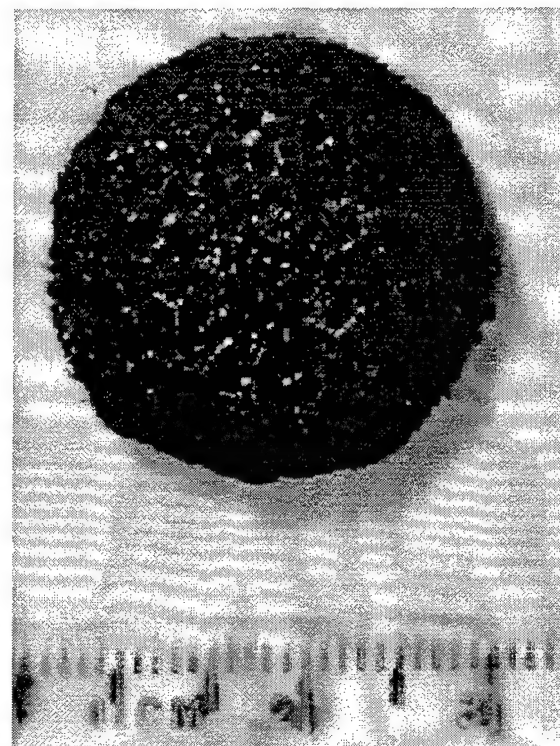
4.8.3.2 Foams with Additives

In addition to the solid pitch samples above, unstabilized pitch foams were treated with the furfuryl aldehyde and furfuryl alcohol polymeric additives. In these cases the low-viscosity liquids were vacuum infiltrated into the foams, and then the excess liquid was allowed to drain out of the foams. It was assumed that a thin layer of the polymer forming liquid would coat the foam surfaces and support the pitch struts until they were sufficiently carbonized to support themselves. The liquid-infiltrated foams were carbonized directly and after curing in an oven for two hours at 150°C. The uncured samples were tested to see if the liquid would polymerize sufficiently during the initial carbonization heating and therefore save a step in the process.

Neither the cured or uncured furfuryl alcohol samples were stabilized; the foams lost shape and collapsed during carbonization. The same was true for the uncured furfuryl aldehyde-treated foam, but the cured furfuryl aldehyde-treated foam retained its shape



(a)



(b)

Figure 101. Pellets after Carbonization: (a) Pellet formed from Powder Treated with Nitric Acid and (b) a Typical Bloated Pellet.

completely. Microscopy on the carbonized foams showed an internal bubble structure virtually identical to the original foam, except that many of the struts were covered by an isotropic layer that is the cured and carbonized furfuryl aldehyde polymer.

This avenue of foam stabilization was not pursued further, since foam production had introduced additional steps during cool down that apparently will sufficiently oxygen-stabilize the foam. So despite this success, alternative stabilization techniques are no longer considered necessary for the foams.

4.8.3.3 Pitch/T-300 Composites

Testing began on composites for several reasons, even though the neat pitch samples failed to be stabilized. Composites made from pitch were one of the major outlets for this work from the beginning. There was a need to see if pitch with additives could be processed into composites. Melt pressing the pitch after addition of the stabilizers would allow some or all reaction to occur prior to carbonization. Finally, the neat pitch samples which were

partially covered by metal plates during carbonization bloated less than open samples, and it was believed that the fabric in the composites would hold the plate mass better than neat pitch.

These composites consisted of two layers of T-300 fabric and pitch with additives. Stabilizers were added to the pitch by dissolving them in THF, making a slurry of the THF solution and pitch, and allowing the THF solvent to evaporate. This was essentially the same procedure as the "powder" method above, except instead of cold pressing a pellet, the pitch was placed between fabric sheets and hot pressed.

The move to composites was justified in the results. Bloating was reduced in all of the samples tested, although not all the samples gave good composites.

The first set of samples (based on the foam success) incorporated furfuryl aldehyde, both by adding the furfuryl aldehyde to the pitch before melt pressing and by soaking the pitch composite in THF containing furfuryl aldehyde after melt pressing. In both cases the manufactured composite was split in two with one piece being given an additional cure of two hours at 150°C. Bloating was reduced for all samples. Because the additive level is more easily controlled by incorporating it into the pitch before melt pressing and there were little differences in the results, this method was used for the next sample set.

The second set of samples consisted of the three polymeric materials used with the neat pitch samples and the other additives of p-benzoquinone and hexamethylene disilazane. The results are summarized in Table 23. The composite overall char yields were all in the 90 percent range, and the level of bloating was significantly reduced, relative to unstabilized pitch or the neat pitch samples. The similarity in the results between cured (two hours at 150°C) versus uncured indicates this step may not be necessary.

The amount of pitch incorporated into the composite was less than desired. This is believed to have caused the poor composites which delaminated. Future work in the stabilization area will incorporate more pitch resin into the composites to eliminate this problem.

4.8.4 Partial Carbonization of Pitch Samples

An alternate means of producing a pitch composite without oxygen stabilization may be the use of partially-carbonized pitch. Work by Fujiura, et al. [23] indicated that pitch, heated to above its melt temperature but below the carbonization level, can be pressed into reasonable carbon articles without further stabilization. This study was initiated primarily as a

TABLE 23
PITCH STABILIZATION IN COMPOSITES RESULTS

additive	% additive	cured		uncured	
		char yield	bloat ^a	char yield	bloat ^a
SC-1008 phenolic	11	92.1	1	90.3	0 ^b
	20	89.3	0	91.2	0
	40	87.7	1	92.3	0
Furfuryl alcohol	10	94.4	1	90.1	0
	20	93.0	1 ^b	93.0	0
	39	92.4	0	92.0	0
Furfuryl aldehyde	9	92.5	0	92.8	2
	21	91.6	1	90.9	0
	40	93.5	1 ^b	91.6	2
p-Benzoquinone	11	93.9	0 ^b	93.8	0 ^b
	22	94.2	0	91.8	0
	40	93.3	0	91.4	0
Hexamethylene disilazane	11	92.9	0	98.1	0
	20	94.3	0	92.5	1
	41	94.0	0 ^b	92.7	0

a - Bloating index from 0 = no bloating to 4 = complete bloating

b - Sample delaminated when cut after carbonization

route to produce pitch for the sintering work in Section 4.7 but also as a possible precursor to melt processed pitch composites.

The initial work in partial carbonization was done using thermogravimetric analysis (TGA). Pitch samples were heated at constant rates and their weight loss measured. The measurements were done in both air and nitrogen atmospheres. The Mitsubishi AR was also examined as both a powder and the as-received pellets. Ashland A-240 was tested after crushing, but its low melt temperature and melt viscosity should have produced the same results as any other form of this pitch. This was confirmed when the A-240 appeared to have melted into a single mass for all the sample runs.

The AR pitch started to lose weight at approximately 400°C with a total weight loss of 20 percent after reaching and holding at 450°C for two hours in a nitrogen atmosphere.

When the TGA was run in air, there was a significant difference between the as-received pellets and the powder samples: the powder samples picked up mass starting about 220°C with a maximum at 320°C before losing all but 38 percent of the original mass. The as-received pellets did not gain weight but did start to lose weight at 400°C to give a final mass of 90 percent of the starting mass. The difference in form is undoubtedly due to the much larger surface-to-volume ratio in the powder. Oxygen can penetrate, allowing weight gain, and then as the reaction continues, the pitch reacts to form CO₂. In pellets the oxygen may penetrate slightly, but the burning and stabilization rates balance until the entire pellet is sufficiently stable to withstand the 450°C temperatures. In nitrogen the reactions are roughly the same: weight loss due to low molecular weight species vaporizing and partial carbonization products leaving the samples.

For the A-240 pitch the weight loss began at 200°C in air and 290°C in nitrogen. The weight loss leveled off in air at about 350°C with a total loss of 45 percent after two hours at 450°C. In nitrogen the weight loss was more gradual, leveling off during the 450°C hold with a total loss of 64 percent. Partial carbonization of the A-240 could therefore be accomplished more easily than for the AR pitch but with more loss of mass.

Several small batches of both AR and A-240 pitch were partially carbonized in the carbonization furnace. These samples were heated to 450°C in nitrogen in individual large stainless-steel cans. The yield was 74 percent for the AR and 64 percent for the A-240. The AR pitch stayed as a powder, albeit slightly melted together, which did not show any additional mass loss by TGA. The A-240 pitch melted into a single mass with another reaction occurring in A-240: the formation of mesophase regions from the initial isotropic pitch. This can be seen in Figure 102.

The A-240 lost an additional 10 percent mass in the TGA starting at 300°C and showed a baseline shift (T_g or softening point) around 242°C.

Larger samples of AR pitch did not lose much mass (only 0.5 percent) and showed similar mass losses in the TGA to the starting material. It was surmised that with the large volume of material, the top layer of material underwent mass loss (top layer bloated in the steel can), but this bloated layer prevented the underlying material from giving up its volatile matter. A modification of the initial experiment consisted of pulling a vacuum on the pitch which did result in a larger mass loss. TGA of this pitch showed very little weight loss up to 450°C and a total weight loss of six percent up to 600°C after the partial carbonization.

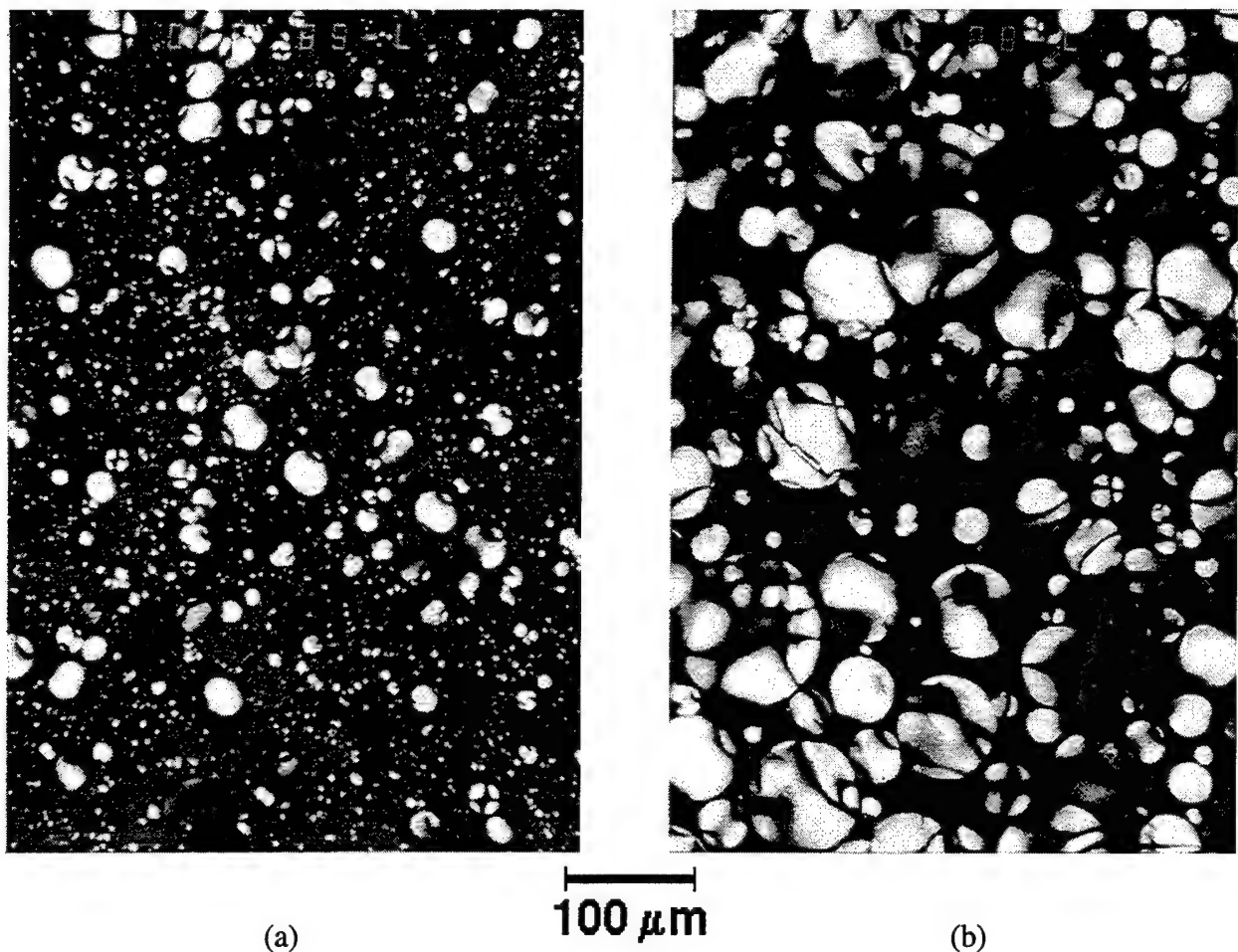


Figure 102. Optical Polarizing Microscopy of Partially-Carbonized A-240 Pitch Showing Different Size Mesophase Regions in the Same Sample.

The length of time required to remove volatiles with a minimum amount of reaction was tested with A-240 and Aerocarb-80 (reportedly A-240 run through an evaporator to remove volatiles). The pitches were heated to a furnace temperature of 450°C and held for varying amounts of time. Table 24 shows the results. Very little weight was lost when the temperature was raised and then lowered. When the samples held at temperature, one hour was sufficient to remove whatever material could be removed at that temperature. A-240 lost 38 to 39 percent of its original mass, and Aerocarb-80 lost 12 to 15 percent of its original mass. Any carbonization reaction which occurs at this temperature is complete and its products removed within one hour.

TABLE 24

PARTIAL CARBONIZATION YIELDS (% REMAINING) FOR A-240 AND AEROCARB-80 PITCHES AS A FUNCTION OF TIME HELD AT 450°C

Dwell Time (hr)	A-240	Aerocarb-80
0	99.3	95.0
1	61.9	85.0
2	61.0	83.9
4	61.7	83.3

4.8.5 FTIR Analysis of Pitch

A study of the Fourier transform infrared (FTIR) absorption of pitch was undertaken in order to evaluate the degree of oxygen stabilization and graphitization in pitch materials. The results of this study are directly related to the press sintering project results and are part of the characterization of pitches stabilized by nonair oxidized means. The *in situ* monitoring of the carbonization process by FTIR [24] also requires a knowledge of the absorption response of the pitch which will be measured in the next phase of this study.

The absorption of light is governed by the Beer-Lampert Law:

$$A = \epsilon lc \quad (4-1)$$

and

$$T = \log_{10}\left(\frac{1}{A}\right) \quad (4-2)$$

where A is the absorption, ϵ is the absorption coefficient for the species being examined, l is the sample pathlength, c is the sample concentration, and T is the transmittance (often expressed in percent). This law holds for light of almost any wavelength from infrared to x-rays.

Since absorption is an exponential measurement and transmittance is a linear measurement, it is usually easier to measure transmittance and then calculate the absorption. It was also found to give significantly better baseline corrections. In all cases reported here, the transmittance was actually measured and the baseline subtracted by the FTIR instrument and then the scans converted to absorption for later analysis.

The pathlength of the sample was fixed at 25 μm primarily because a holder which easily fit into the instrument could be fabricated from a manila folder of that thickness. It was found, through trial-and-error, that a pitch in potassium bromide salt concentration of two

percent gave reasonable and reproducible absorption levels. The KBr salt does not absorb in the measurement region of FTIR and is used to hold the sample, since a solid pitch sample of the thickness of the sample holder would absorb entirely too much of the infrared radiation.

The numbers of interest from these measurements are the relative concentrations of species in the sample. In an unoxidized pitch sample, only hydrocarbon bands should be observed, while in oxidized samples various oxygen-containing groups will be observed. The details of what groups absorb in pitch were established by Drbohlav and Stevenson [25]. The absorption bands and the responsible chemical moieties are give in Table 25. They also reported that the 1600 cm^{-1} band can be used as an internal standard. An internal standard is usually a superior measurement for semiquantitative results, since exact thicknesses and KBr concentrations are difficult to obtain.

Figure 103 shows the FTIR region of most interest for AR powders as received and oxidized six percent. The absorptions in this figure and all the absorption ratios discussed below have been normalized to the 1600 cm^{-1} band. It can be seen immediately that the hydrogen out-of-plane bending bands drop dramatically in the oxidized sample as well as the methylene bridge bending absorption. The rise in the oxygen-containing bands is also clearly visible.

A series of mixtures of these two powders was examined to see if the absorption ratios for each band (relative to the 1600 cm^{-1} band) could accurately predict the amount of oxidation. Figure 104 shows these ratios for the methylene bridge and oxygen moieties. There is an approximately linear decrease in the methylene bridge and similar increase in the carbonyl and ether bands. The phenolic band is almost flat, indicating there was not a lot of change in that group. The free hydroxyl rises and then falls, but this band is the one most susceptible to water contamination. The decrease in the hydrogen species in Figure 105 shows very linear curves.

When pitches oxidized to various levels are examined, a different picture develops. Figures 106 and 107 show the ratios for AR pitch oxidized to weight gains of 0, 1, 5 and 6 percent. What can be seen is the dramatic decrease in hydrogen species and the methylene bridge from 0 to 1 percent which then levels out. The equivalent increase and leveling out in oxygen-containing species can also be seen. The TGA on these same three oxidized powders showed almost identical 7-9 percent mass loss to 500°C .

These absorption ratios are from peak heights rather than from the much more difficult to measure peak areas, but the real reason may be more the assumption of the constancy

TABLE 25

ABSORPTION BANDS REPORTED BY DRBOHLAV AND STEVENSON [25] FOR
OXIDIZED PITCH AND GENERALLY IN SILVERSTEIN AND BASSLER [26]

Chemical Moiety	Approximate Wavenumber (cm ⁻¹)
HO- hydroxyl stretching	3200-3550
H- aromatic stretching	3050
H- aliphatic stretching	2925
H- other stretching	2850
C=O carbonyl stretching	1675-1800
aromatic ring bending	1600
-CH ₂ - methylene bridge bending	1440
Arom-OH phenol stretching	1380
-O- ether stretching	1250
H- single naphthalenic out-of-plane bending	880
H- two and three adjacent naphthalenic out-of-plane bending	810
H- four adjacent naphthalenic out-of-plane bending	750

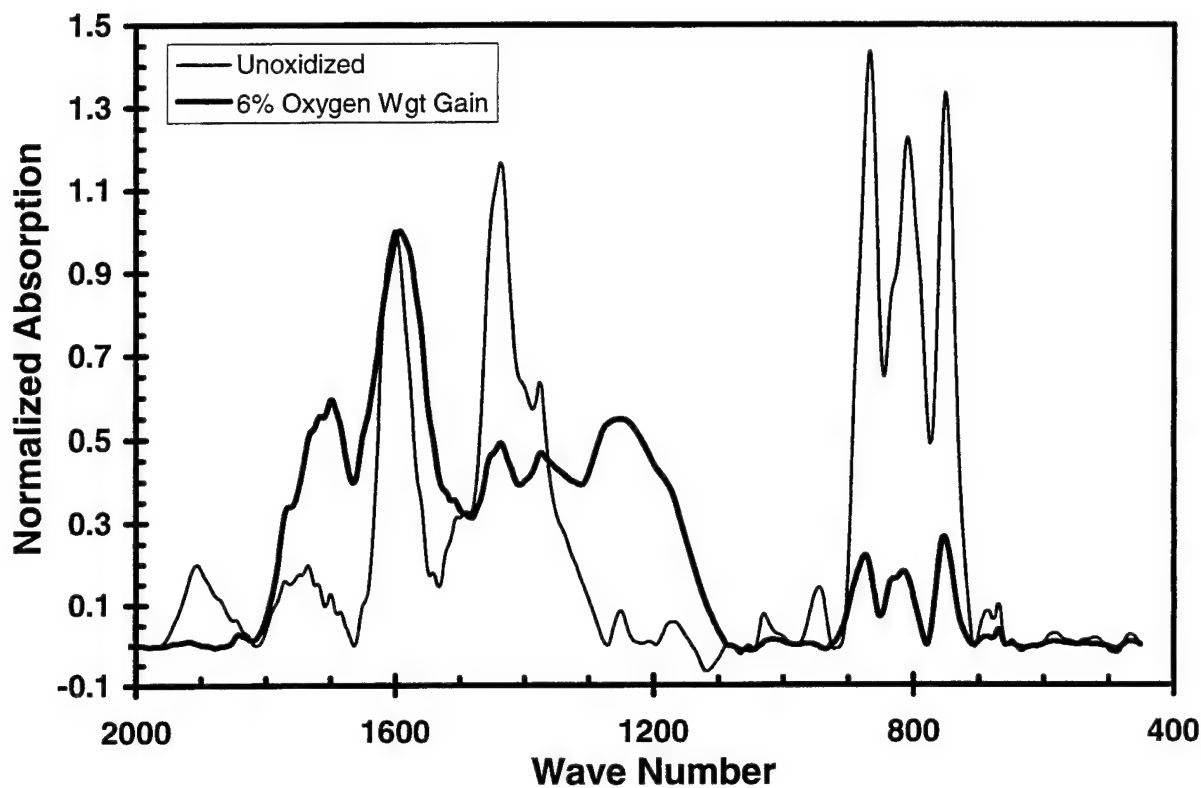


Figure 103. Normalized FTIR Absorption Scan for Unoxidized and 6% Oxidized Mitsubishi AR Pitch Powder.

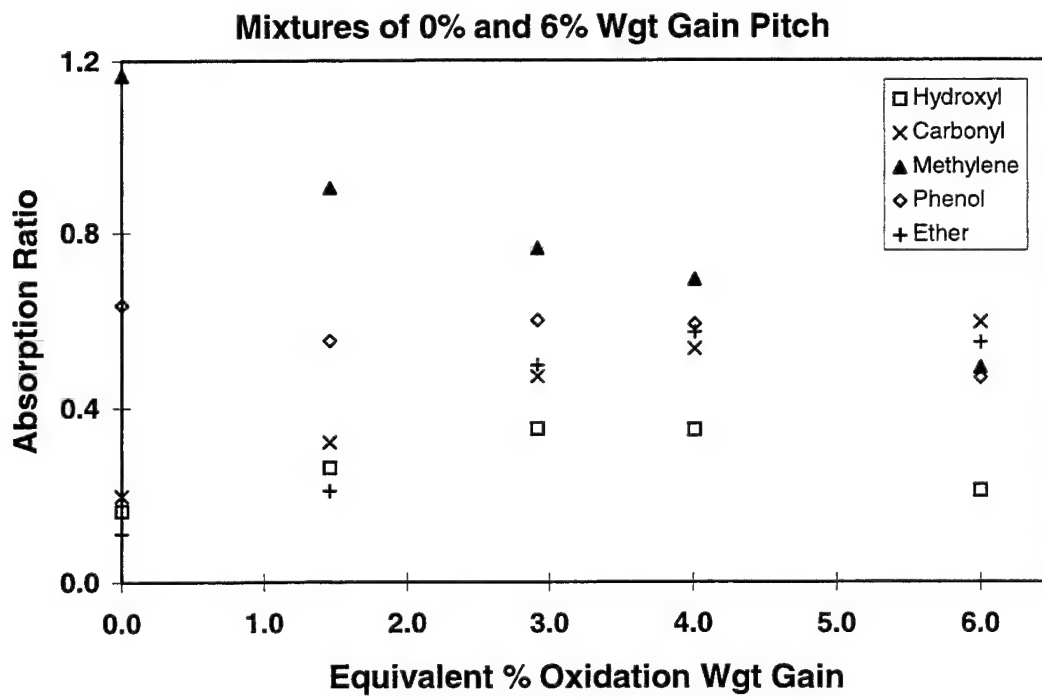


Figure 104. Absorption Ratios for Mixes of 0 and 6% Oxidized AR Pitch Powders.

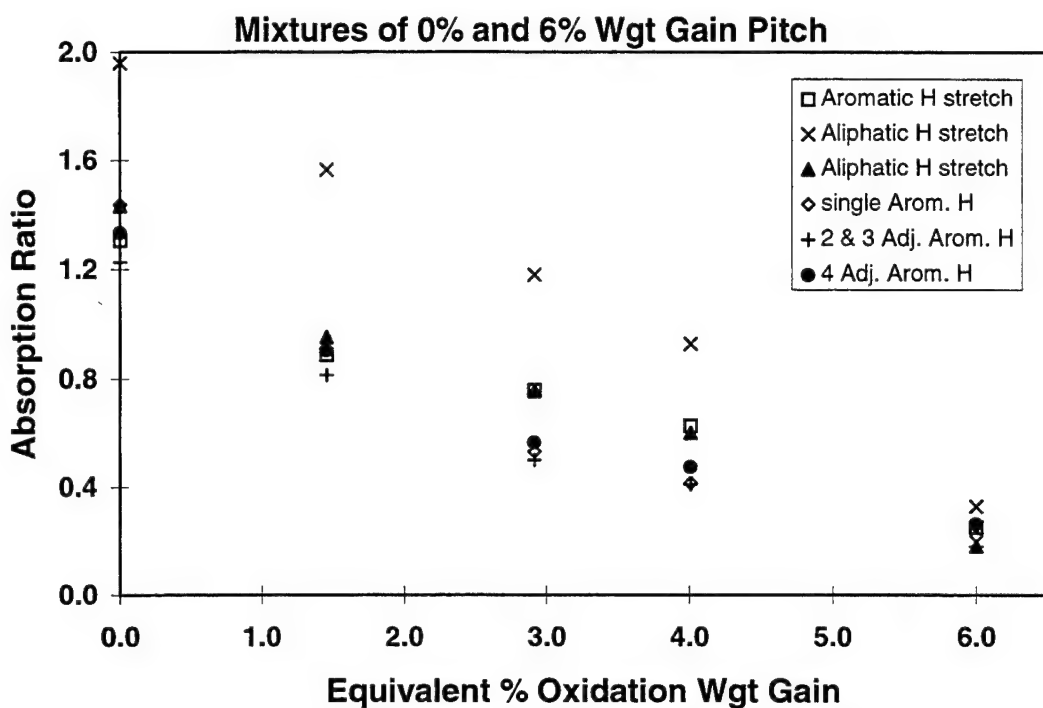


Figure 105. Absorption Ratios of Hydrogen Species for Mixes of 0 and 6% Oxidized AR Pitch Powders.

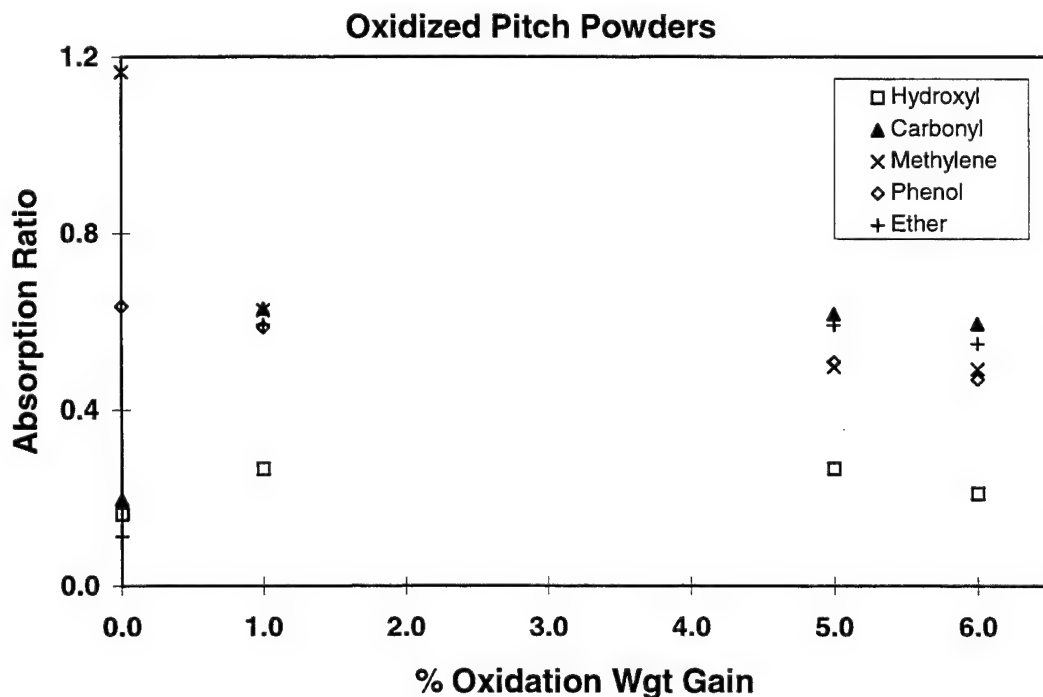


Figure 106. Absorption Ratios for AR Pitch Powders Oxidized to Various Levels.

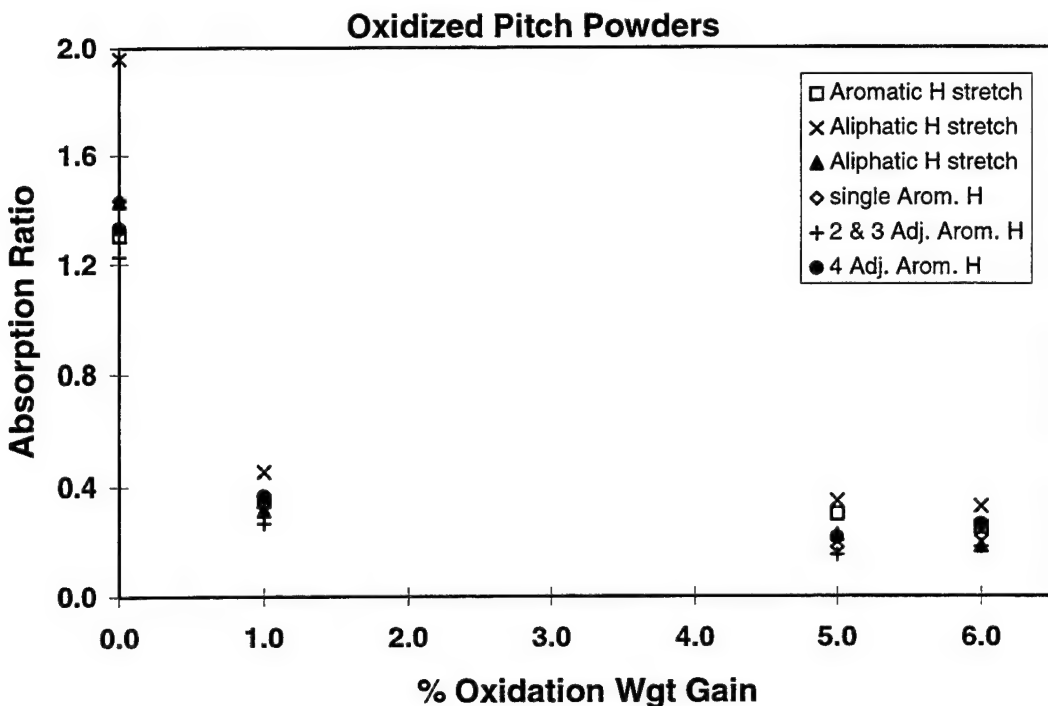


Figure 107. Absorption Ratios of Hydrogen Species for AR Pitch Powders Oxidized to Various Levels.

of the aromatic ring bending at 1600 cm^{-1} . There may be an oxygen-containing species which absorbs at or near 1600 cm^{-1} which causes this band to be artificially large. Certainly the absorption coefficient of this band is much less than the oxygen bands. The aromatic rings constitute more than 90 percent of the pitch, while the individual oxygen moieties amount to a total of 1-6 percent, but the absorption heights of those species are all of the same order of magnitude as the aromatic ring bending. This makes the use of FTIR useful in determining if a powder has been oxidized but not to what level, unless a different internal standard can be found.

4.9 EVALUATION OF A NEW HIGH CHAR YIELD RESIN

Three composite samples from Southern Mississippi University (SMU) with a matrix resin of propargyl cyclopentadiene (PCP) [27] and K-1100 fiber were carbonized to give 95 percent char in the composite. Interlaminar tensile strengths (ILS) of the carbonized composites were $\sim 300\text{ psi}$. This is approximately the strength of uncarbonized phenolic and twice that of carbonized phenolic composites. The three samples had slightly different cure cycles but gave the same char yield and ILS. Microscopy on the uncarbonized PCP samples showed large cracks between what appears to be fiber bundles (see Figure 108). Some cracking of the matrix within fiber bundles was also visible. After carbonization, the matrix within bundles could be seen to

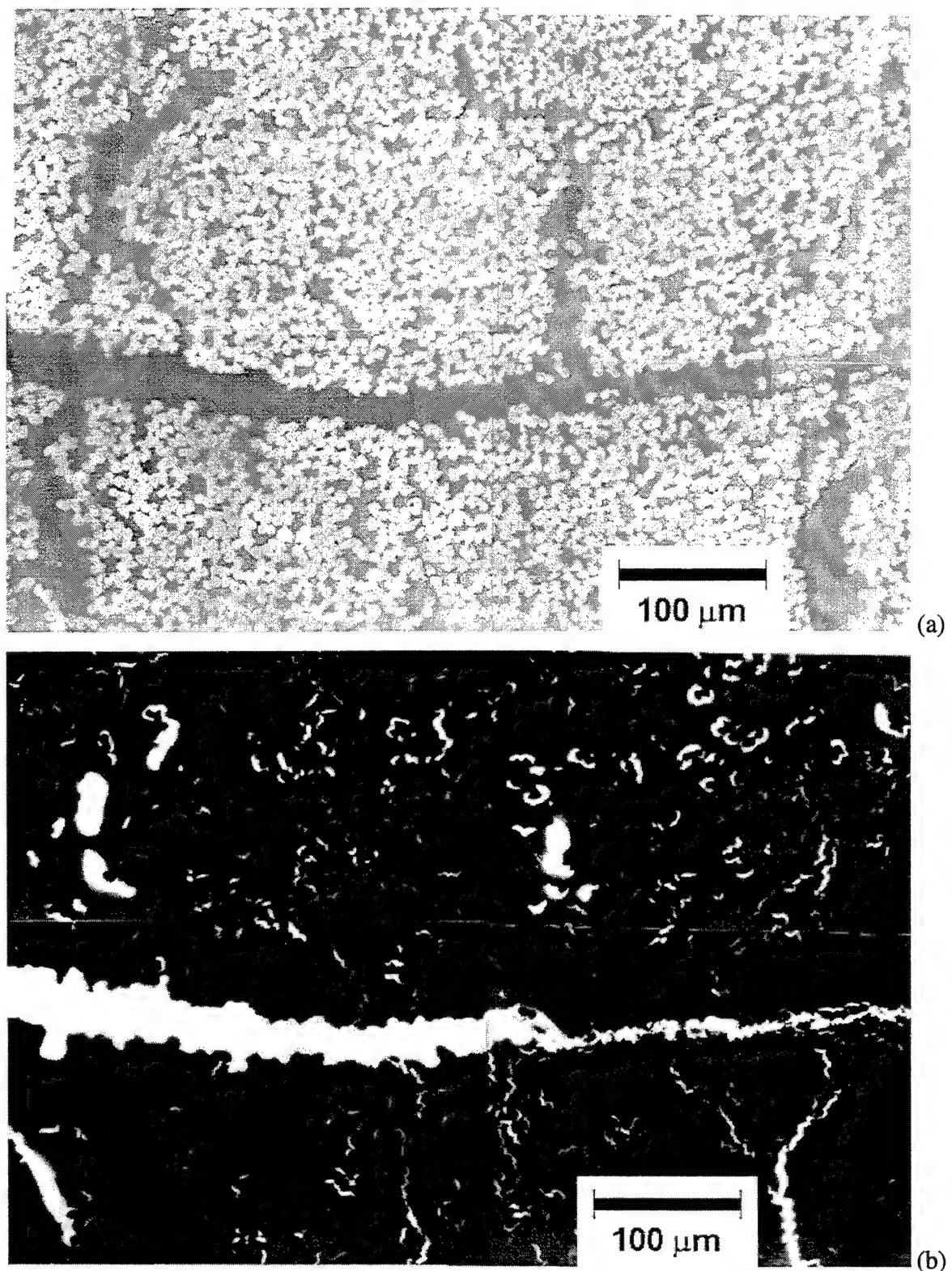


Figure 108. Optical Microscopy of a Cured PCP Composite: (a) Bright Field and (b) Fluorescent Image.

crack near the fiber matrix interface at virtually every fiber (see Figure 109). Despite these cracks the mechanical properties were still quite good.

A second series of composite samples from SMU, made with the PCP resin and AS-4 fibers, was carbonized. The char yield of these composites was ~90 percent. Despite the lower char yield, these composites had fewer cracks than the K-1100 fiber composites. ILS values on the carbonized samples are currently being measured.

The as-cured composite quality of both of these composite series was poor; even better mechanical properties may be possible if better "as-cured" composites can be obtained.

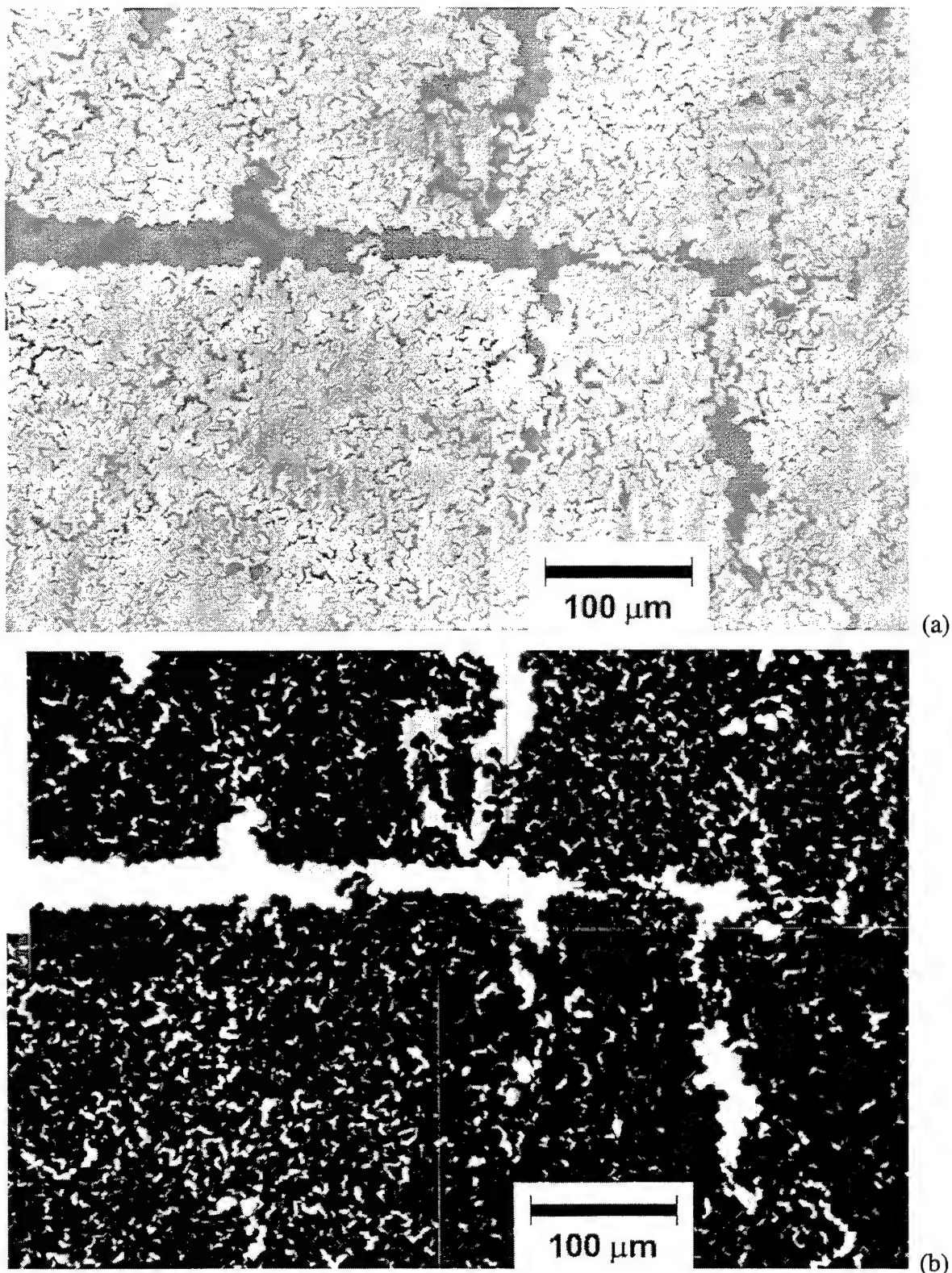


Figure 109. Optical Microscopy of a Carbonized PCP Composite: (a) Bright Field and (b) Fluorescent Image.

SECTION 5

REFERENCES

1. Rice, B. P. (1996). Recent Studies Concerning Hydrolytic Degradation of High-Temperature Polyimides. *Proceedings of High Temple Workshop XVI* (pp. U1-U23).
2. Crasto, A. S., R. Y. Kim, C. Fowler, & J. P. Mistretta. (1996). Rehabilitation of Concrete Bridge Beams with Externally-Bonded Composite Plates, Part I. *Proceedings of First Int. Conference on Composites for Infrastructure* (ICCI-I).
3. Roy, A. K. (1996). *In Situ* Damage Observation and Failure in Model Laminates Containing Planar Yarn Crimping of Woven Composites. *Mechanics of Composite Materials and Structures* 3(2) (101-117).
4. Reissner, E. (1950). On a Variational Theorem in Elasticity. *J. of Mathematical Physics* 29 (90-95).
5. Iarve, E. (1996). Spline Variational Three-Dimensional Stress Analysis of Laminated Composite Plates with Open Holes. *Int. J. of Solids & Structures* 33(14) (2095-2117).
6. Oakes, D., M. Norris, & H. Chen. (1995, October). *Coefficient of Thermal Expansion Measurements of High Modulus Fiber*. Purchase Order No. S8-164687-LNH, Hughes Aircraft Company Space & Communications.
7. Pagano, N. J., & S. R. Soni. (1983). Global-Local Laminate Variation Model. *Int. J. Solids & Structures* 19 (207).
8. Kim, R. Y. (1989). Experimental Observation of Free-Edge Delamination. In N. J. Pagano, Ed., *Interlaminar Response of Composite Materials* (pp. 111-160). Elsevier.
9. Kim, R. Y., F. Abrams, & M. Knight. (1988). Mechanical Characterization of a Thick Composite Laminate. *Proceedings of American Society for Composites* (pp. 711-718). Technomic Publishing Co.
10. Park, W. J., & R. Y. Kim. (1982). Statistical Analysis of Composite Fatigue Life. In T. Hayashi, Ed., et al., *Progress in Science & Engineering of Composites* (pp. 708-716). Tokyo, Japan: ICCM-IV.
11. Lee, C. W., & B. Rice. (1996, November). *Modeling of Epoxy Cure Reaction Rate by Neural Network*. Paper presented at 28th International SAMPE Technical Conference, Seattle, WA.

12. Whitcomb, J. D. (1991). Three-Dimensional Stress Analysis of Plain Weave Composites. In T. K. O'Brien, Ed., *Composite Materials: Fatigue and Fracture 3* (ASTM STP 1110, 417-438). Philadelphia: ASTM.
13. Fukuda, N., & K. Nagasawa. (1985). *Sprechsaal 118*.
14. Nagayama, K., T. Torii, H. Hatano, & N. Fukuda. (1991). A Study of the Sintering Mechanism of KMFC Green Compact Made of Mesocarbon-Microbeads. *Proceedings of the 20th Biennial Conference on Carbon* (p. 206).
15. Nakagawa, Y., K. Fujita, & M. Mori. (1985). An Industrial Process for Mesocarbon Microbeads. *Proceedings of the 17th Biennial Conference on Carbon* (p. 409).
16. Rand, B., & C. Stirling. (1991). Sintered Carbons from Mesophase Powders. *Proceedings of the 20th Biennial Conference on Carbon* (p. 204).
17. El Horr, N., C. Bourgerette, & A. Oberlin. (1994). Mesophase Powders (Carbonization and Graphitization). *Carbon 32* (p. 1035).
18. Hoffman, W. R., & K. J. Hutterer. (1993). Demonstration of Spontaneous Liquid-Phase Sintering of Mesophase Powders. *Carbon 31* (p. 259).
19. Hoffman, W. R., & K. J. Hutterer. (1993). Modeling of the Apparent Viscosity of Pitches and Mesophases at Linear Temperature Increase up to 500°C. *Carbon 31* (p. 263).
20. Hoffman, W. R., & K. J. Hutterer. (1994). Sintering of Powders of Polyaromatic Mesophase to High Strength Isotropic Carbons - I. Influence of the Raw Material and Sintering Conditions on the Properties of the Carbon Materials. *Carbon 32* (p. 1087).
21. Gschwindt, A., & K. J. Hutterer. (1994). Sintering of Powders of Polyaromatic Mesophase to High Strength Isotropic Carbons - II. Influences of the Synthesis Conditions of the Mesophase and the Preparation of the Powders. *Carbon 32* (p. 1105).
22. Mochida, I., et al. (1994). Self-Adhesive Carbon Grains Oxidatively Prepared from Naphthalene-Derived Mesophase Pitch for Mould of High Density. *Carbon 32* (p. 961).
23. Fujiura, R., T. Kojima, M. Komatsu, & I. Mochida. (1995). Mechanical Properties of Binderless Carbon Mould Prepared from Heat-Treated Mesophase Pitch of Controlled Grain Size. *Carbon 33* (1061).
24. Druy, M., & P. Glatkowski. (1996). *In Situ Fiber-Optic FTIR Process Monitor for Advanced Composites* (WL-TR-94-4076). Dayton, OH: U.S. Air Force.

25. Drbohlav, J., & W. T. K. Stevenson. (1995). The Oxidative Stabilization and Carbonization of a Synthetic Mesophase Pitch, Part I: The Oxidative Stabilization Process. *Carbon* 33 (693).
26. Silverstein, R. M., & G. C. Bassler. (1967). *Spectrometric Identification of Organic Compounds* (Chapter 3). New York: John Wiley & Sons, Inc.
27. Mathias, L. J., & J. Muthiah. (1994). Synthesis and Characterization of a New Class of Thermosetting Resins: Allyl and Propargyl Substituted Cyclopentadiene Derivatives. *Polymer Composites* 15 (464).

APPENDIX

Notations used in Equation (2-14)

$$\chi_{ij}^{(k)} = \eta_{ij}^{(k)} - E_{ij}^{(k)} - \hat{S}_{ilmj}^{(k)} S_{lm}^{(k)}$$

where

$$\hat{S}_{ijLM}^{(k)} = \int_{h_{k-1}}^{h_k} S_{ij}^{(k)} f_L^{(j)} f_M^{(i)} dz, \quad E_{ij}^{(k)} = \int_{h_{k-1}}^{h_k} e_i^{(k)} f_j^{(i)} dz,$$

and S_{ij} is the compliance matrix.

$$\begin{aligned} \eta_{11}^{(k)} &= (h_k - h_{k-1}) \frac{\partial \bar{u}}{\partial x} + \frac{\partial(h_k - 2h_{k-1})}{\partial x} \bar{u} - \frac{\partial h_k}{\partial x} u^*, \quad \eta_{12}^{(k)} = (h_k - h_{k-1}) \frac{\partial u^*}{\partial x} + \frac{\partial(2h_k - h_{k-1})}{\partial x} u^* + \frac{\partial h_{k-1}}{\partial x} \bar{u} \\ \eta_{21}^{(k)} &= (h_k - h_{k-1}) \frac{\partial \bar{v}}{\partial y} + \frac{\partial(h_k - 2h_{k-1})}{\partial y} \bar{v} - \frac{\partial h_k}{\partial y} v^*, \quad \eta_{22}^{(k)} = (h_k - h_{k-1}) \frac{\partial v^*}{\partial y} + \frac{\partial(2h_k - h_{k-1})}{\partial y} v^* + \frac{\partial h_{k-1}}{\partial y} \bar{v} \\ \eta_{31} &= \bar{w} + w^*, \quad \eta_{32} = -(\bar{w} + w^*), \quad \eta_{33} = \bar{w} - w^*, \quad \eta_{34}^{(k)} = -3\hat{w} + \frac{h_k + 2h_{k-1}}{h_k - h_{k-1}} \bar{w} - \frac{2h_k + h_{k-1}}{h_k - h_{k-1}} w^* \\ \eta_{41}^{(k)} &= \bar{v} + v^* + (h_k - h_{k-1}) \frac{\partial \bar{w}}{\partial y} + \frac{\partial(h_k - 2h_{k-1})}{\partial y} \bar{w} - \frac{\partial h_k}{\partial y} w^* \\ \eta_{42}^{(k)} &= -\bar{v} - v^* + (h_k - h_{k-1}) \frac{\partial w^*}{\partial y} + \frac{\partial(2h_k - h_{k-1})}{\partial y} w^* + \frac{\partial h_{k-1}}{\partial y} \bar{w} \\ \eta_{43}^{(k)} &= \bar{v} - v^* + (h_k - h_{k-1}) \frac{\partial \hat{w}}{\partial y} + 3 \frac{\partial(h_k - h_{k-1})}{\partial y} \hat{w} + \frac{\partial}{\partial y} (h_k w^* - h_{k-1} \bar{w}) \\ \eta_{51}^{(k)} &= \bar{u} + u^* + (h_k - h_{k-1}) \frac{\partial \bar{w}}{\partial x} + \frac{\partial(h_k - 2h_{k-1})}{\partial x} \bar{w} - \frac{\partial h_k}{\partial x} w^* \\ \eta_{52}^{(k)} &= -\bar{u} - u^* + (h_k - h_{k-1}) \frac{\partial w^*}{\partial x} + \frac{\partial(2h_k - h_{k-1})}{\partial x} w^* + \frac{\partial h_k}{\partial x} \bar{w} \\ \eta_{53}^{(k)} &= \bar{u} - u^* + (h_k - h_{k-1}) \frac{\partial \hat{w}}{\partial x} + 3 \frac{\partial(h_k - h_{k-1})}{\partial x} \hat{w} + \frac{\partial}{\partial y} (h_k w^* - h_{k-1} \bar{w}) \end{aligned}$$

$$\eta_{61}^{(k)} = (h_k - h_{k-1}) \left(\frac{\partial \bar{u}}{\partial y} + \frac{\partial \bar{v}}{\partial x} \right) + \frac{\partial (h_k - 2h_{k-1})}{\partial x} \bar{v} + \frac{\partial (h_k - 2h_{k-1})}{\partial y} \bar{u} - \frac{\partial h_{k-1}}{\partial x} v^* - \frac{\partial h_{k-1}}{\partial y} u^*$$

$$\eta_{62}^{(k)} = (h_k - h_{k-1}) \left(\frac{\partial u^*}{\partial y} + \frac{\partial v^*}{\partial x} \right) + \frac{\partial (2h_k - h_{k-1})}{\partial x} v^* + \frac{\partial (2h_k - h_{k-1})}{\partial y} u^* + \frac{\partial h_{k-1}}{\partial x} \bar{v} + \frac{\partial h_{k-1}}{\partial y} \bar{u}$$

$$\mu_{11}^{(k)} = \frac{\partial h_1}{\partial x} u_1^{(k)}, \quad \mu_{12}^{(k)} = -\frac{\partial h_2}{\partial x} u_2^{(k)}, \quad \mu_{21}^{(k)} = \frac{\partial h_1}{\partial y} v_1^{(k)}, \quad \mu_{22}^{(k)} = -\frac{\partial h_2}{\partial y} v_2^{(k)}$$

$$\mu_{31}^{(k)} = -w_1^{(k)}, \quad \mu_{32}^{(k)} = w_2^{(k)}, \quad \mu_{41}^{(k)} = \frac{\partial h_1}{\partial y} w_1^{(k)} - v_1^{(k)}, \quad \mu_{42}^{(k)} = -\frac{\partial h_2}{\partial y} w_2^{(k)} + v_2^{(k)}$$

$$\mu_{52}^{(k)} = -\frac{\partial h_2}{\partial x} w_2^{(k)} + u_2^{(k)}, \quad \mu_{51}^{(k)} = \frac{\partial h_1}{\partial x} w_1^{(k)} - u_1^{(k)},$$

$$\mu_{61}^{(k)} = \frac{\partial h_1}{\partial y} u_1^{(k)} + \frac{\partial h_1}{\partial x} v_1^{(k)}, \quad \mu_{62}^{(k)} = -\left(\frac{\partial h_2}{\partial y} u_2^{(k)} + \frac{\partial h_2}{\partial x} v_2^{(k)} \right)$$

$$F_1^{(k)} = (h_k - h_{k-1}) \left(\frac{\partial s_{11}^{(k)}}{\partial x} + \frac{\partial s_{61}^{(k)}}{\partial y} \right) + (s_{11}^{(k)} - s_{12}^{(k)}) \frac{\partial h_{k-1}}{\partial x} + (s_{61}^{(k)} - s_{62}^{(k)}) \frac{\partial h_{k-1}}{\partial y} - s_{51}^{(k)} + s_{52}^{(k)} - s_{53}^{(k)}$$

$$F_2^{(k)} = (h_k - h_{k-1}) \left(\frac{\partial s_{12}^{(k)}}{\partial x} + \frac{\partial s_{62}^{(k)}}{\partial y} \right) + (s_{11}^{(k)} - s_{12}^{(k)}) \frac{\partial h_k}{\partial x} + (s_{61}^{(k)} - s_{62}^{(k)}) \frac{\partial h_k}{\partial y} - s_{51}^{(k)} + s_{52}^{(k)} + s_{53}^{(k)}$$

$$F_3^{(k)} = (h_k - h_{k-1}) \left(\frac{\partial s_{61}^{(k)}}{\partial x} + \frac{\partial s_{21}^{(k)}}{\partial y} \right) + (s_{61}^{(k)} - s_{62}^{(k)}) \frac{\partial h_{k-1}}{\partial x} + (s_{21}^{(k)} - s_{22}^{(k)}) \frac{\partial h_{k-1}}{\partial y} - s_{41}^{(k)} + s_{42}^{(k)} + s_{43}^{(k)}$$

$$F_4^{(k)} = (h_k - h_{k-1}) \left(\frac{\partial s_{62}^{(k)}}{\partial x} + \frac{\partial s_{22}^{(k)}}{\partial y} \right) + (s_{61}^{(k)} - s_{62}^{(k)}) \frac{\partial h_k}{\partial x} + (s_{21}^{(k)} - s_{22}^{(k)}) \frac{\partial h_k}{\partial y} - s_{41}^{(k)} + s_{42}^{(k)} + s_{43}^{(k)}$$

$$F_5^{(k)} = (h_k - h_{k-1}) \left(\frac{\partial s_{51}^{(k)}}{\partial x} + \frac{\partial s_{41}^{(k)}}{\partial y} \right) + (s_{51}^{(k)} - s_{52}^{(k)} + s_{53}^{(k)}) \frac{\partial h_{k-1}}{\partial x} + (s_{41}^{(k)} - s_{42}^{(k)} + s_{43}^{(k)}) \frac{\partial h_{k-1}}{\partial y} \\ - s_{31}^{(k)} + s_{32}^{(k)} - s_{33}^{(k)} - \frac{2h_{k-1} + h_k}{h_k - h_{k-1}} s_{34}^{(k)}$$

$$F_6^{(k)} = (h_k - h_{k-1}) \left(\frac{\partial s_{52}^{(k)}}{\partial x} + \frac{\partial s_{42}^{(k)}}{\partial y} \right) + (s_{51}^{(k)} - s_{52}^{(k)} - s_{53}^{(k)}) \frac{\partial h_k}{\partial x} + (s_{41}^{(k)} - s_{42}^{(k)} - s_{43}^{(k)}) \frac{\partial h_k}{\partial y} \\ - s_{31}^{(k)} + s_{32}^{(k)} + s_{33}^{(k)} + \frac{2h_k + h_{k-1}}{h_k - h_{k-1}} s_{34}^{(k)}$$

$$F_7^{(k)} = (h_k - h_{k-1}) \left(\frac{\partial s_{53}^{(k)}}{\partial x} + \frac{\partial s_{43}^{(k)}}{\partial y} \right) - 2s_{53}^{(k)} \left(\frac{\partial h_k}{\partial x} - \frac{\partial h_{k-1}}{\partial x} \right) - 2s_{43}^{(k)} \left(\frac{\partial h_k}{\partial y} - \frac{\partial h_{k-1}}{\partial y} \right) + 3s_{34}^{(k)}$$

PUBLICATIONS, PRESENTATIONS, AND PATENTS

The following is a list of presentations, publications, and patents that were generated during this contractual period.

Anderson, D. P., C. S. Hill, & W. R. Ragland. (1996). "Sintering" of Compacted Pitch Powder as Applied to Carbon-Carbon Processing. *Composites Technology Symposium Proceedings* (p. IV-B-1).

Anderson, D. P., & A. S. Crasto. (1996). A Microstructural Study of Carbon Fibers for Thermal Management and Space Applications. *Proceedings of Space Technology and Applications International Forum (STAIF-96)* (p. 869).

Anderson, D. P., & A. K. Roy. (1995). *Carbon-Carbon Rotor Blade Disk Characterization* (UDR-TR-95-0092). Dayton, OH: University of Dayton Research Institute.

Crasto, A. S., et al. (1996, March). *Prefabricated Vacuum Bag and Vacuum Bag Process to Externally Reinforce Structural Members with Advanced Composites*. U.S. Patent Application.

Crasto, A. S., R. Y. Kim, C. Fowler, & J. P. Mistretta. (1996). Rehabilitation of Concrete Bridge Beams with Externally-Bonded Composite Plates (Part I). *Int. Conf. on Composites in Infrastructure 1* (p. 857).

Crasto, A. S., R. Y. Kim, & J. P. Mistretta. (1996). Rehabilitation of Concrete Bridge Beams with Externally-Bonded Composite Plates (Part II). *Int. SAMPE Symposium 41* (p. 1269).

Crasto, A. S., & R. Y. Kim. (1995, October). *Creep Behavior of High-Temperature Composites*. Paper presented at a TTCP Workshop on High-Temperature Resins and Composites, Williamsburg, VA.

Dutton, R. E., N. J. Pagano, & R. Y. Kim. (1996). Influence of Residual Stress and Interface Bonding on Matrix Cracking Stress and Ultimate Strength of Borosilicate Glass-SiC Fiber Composites. *J. Amer. Cer. Soc.*

Hill, C. S., D. P. Anderson, & W. R. Ragland. (1996). *Application of Sintered Carbon Processing to Carbon-Carbon Composites*. Cocoa Beach Conference on Carbon-Carbon, Cocoa Beach, FL.

Kim, R. Y., & A. S. Crasto. (1996). Measurement of Thermal Expansion Coefficient for Space Structures. *Proceedings of ASTM E-28 Meeting*.

Kim, R. Y. (1995, October). *Creep and Fatigue*. Paper presented at a TTCP Workshop on High-Temperature Resins and Composites, Williamsburg, VA.

Kim, R. Y., & N. J. Pagano. (1995). Progressive Microcracking in Unidirectional SiC/CAS Composites at Elevated Temperatures. *Proceedings of ASME Winter Meeting*.

Lee, C. W., B. Rice, & M. Buczek. (1996). Direct Current Resistance-Based Resin State Sensor. *Proceedings of the 41st International SAMPE Symposium*.

Matikas, T. E., P. Karpur, R. Dutton, & R. Kim. (1995). Influence of the Interface and Fiber Spacing on the Fracture Behavior of Glass Matrix Composites. *Materials Evaluation* 53(5).

Rice, B. P., & C. W. Lee. (1996). Novel, Low-Cost Sensors for Intelligent Process Control. *Proceedings of the 41st International SAMPE Symposium*.

Rice, B. P. (1996). Recent Studies Concerning Hydrolytic Degradation of High-Temperature Polyimides. *Proceedings of High Temple Workshop XVI* (pp. U1-U23).

Roy, A. K. (1996). In Situ Damage Observation and Failure in Model Laminates Containing Planar Yarn Crimping of Woven Composites. *Mechanics of Composite Materials & Structures* 3(2) (pp. 101-117).

Roy, A. K. (1996). Tensile Fatigue Behavior of a Coated Two-Dimensional Carbon-Carbon Composite. *J. of Composites Technology & Research* 18(3) (pp. 202-208).

Roy, A. K., & D. P. Anderson. (1995). Effect of Carbonization Heating Rate, Microstructure, and Lay-Up on the Interlaminar Tensile Properties of a Two-Dimensional Carbon-Carbon Composite. *J. Eng. Mat. & Tech.* 118 (241).

Schaff, J. R., & R. Y. Kim. (1996). Damage Initiation Criteria for Composite Laminates with Open Hole. *Proceedings of 1996 ASME Mechanics & Materials Conference*.

Schmidt, D. L. (In Press). *Carbon-Carbon Composites (CCC) - A Historical Perspective* (WL-TR-96-4107). Dayton, OH: U.S. Air Force.

Tandon, G. P., R. Y. Kim, & R. E. Dutton. (1995, October). *Failure Modes in Unidirectional Composites Under Transverse Loading*. Paper presented at ASC Technical Conference, Santa Monica, CA.

Whitney, J. M., A. S. Crasto, & R. Y. Kim. (1995). Compression Loading of Laminates: *In Situ* Failure of 0° Unidirectional Plies. *J. Compos. Mater.* 29(6) (p. 820).